AN ABSTRACT OF THE THESIS OF

Marshall D. Crew for the degree of Doctor of Philosophy in Chemistry presented on February 24, 1997. Title: **High Resolution Ionization-Detected Stimulated Raman Spectroscopy.**

Abstract approved: _____
Joseph W. Nibler

A new experimental apparatus was built at Oregon State University to perform high resolution stimulated Raman spectroscopy in a pulsed molecular jet at state densities of the order of 10^{11} cm^{-3}. The technique uses a stimulated Raman step to first populate a vibrational/rotational level and then a resonantly enhanced multiphoton ionization (REMPI) step to subsequently probe the Raman pumped upper state. The resulting ions are accelerated down a Wiley-McLaren time of flight mass spectrometer (with mass resolution of 182 amu) and are detected with a home built microchannel plate detector, making mass selective Raman spectroscopy possible.

Instrumental linewidths of 0.001 cm^{-1} were demonstrated for benzene transitions, possibly being the highest resolution yet obtained for stimulated Raman spectroscopy. One reason for this narrow linewidth is that all the spectroscopy is performed in a cold molecular beam. This is advantageous because the rotationally resolved spectra are simplified to a great extent due to the low rotational temperatures (on the order of 10 K) and the collisional and Doppler contributions to the linewidths are reduced to less than the instrumental resolution.

This form of ionization-detected stimulated Raman spectroscopy (IDSRS) was performed on N_2 for the first time. This is important because nitrogen was ionized using a difficult 2 + 2 REMPI step for detection of the Raman signal. Even so, the detection limit was improved by a factor of 10^4 over optical stimulated Raman spectroscopy. These results demonstrate that IDSRS is not limited to the aromatic molecular systems (which are easily ionized with 1 + 1 REMPI) that have been studied almost exclusively to date.

Finally, the unusually high resolution of this experiment has enabled a qualitative study of the AC Stark splittings that come about through the *induced* dipole moment of the benzene molecule. To model the experimental spectra it was determined that good fits can only be achieved by including saturation and temporal/spatial broadening with the Stark splittings. Due to the unique power dependent lineshapes of the Stark split rotational transitions, the Stark effect can be a useful spectroscopic tool for Raman rotational assignments within a particular vibrational band.

High Resolution Ionization-Detected Stimulated Raman Spectroscopy

by

Marshall D. Crew

A THESIS

submitted to

Oregon State University

in partial fulfillment of
the requirements for the
degree of

Doctor of Philosophy

Presented February 24, 1997
Commencement June 1997

Doctor of Philosophy thesis of Marshall D. Crew presented on February 24, 1997

APPROVED:

Redacted for Privacy

Major Professor, representing Chemistry

Redacted for Privacy

Chair of Department of Chemistry

Redacted for Privacy

Dean of Graduate School

I understand that my thesis will become part of the permanent collection of Oregon State University libraries. My signature below authorizes release of my thesis to any reader upon request.

Redacted for Privacy

Marshall D. Crew, Author

ACKNOWLEDGMENTS

Like most people in science, many people have been involved in shaping my career. The first was no doubt my father who raised me to the best of his ability to have creativity, mechanical aptitude, common sense, and a mind of my own – a success that he, not I, should be proud of.

There is always one teacher that stands out in a person's education and for me that person is Dr. Jim Kelly. It is safe to say that if it wasn't for him, I would never have been a scientist. He introduced me to a world of physics that I never dreamed could exist. He allowed me to work in his lab as an undergraduate where I learned that I had skills that were invaluable to a scientist. His constant encouragement is what brought me to graduate school and Oregon State University.

By far, Professor Joe Nibler has been the most influential person in my scientific career. There are so many admirable things about Dr. Nibler that it would be impossible to list them all, but there are a few that I hope to emulate. First is his enthusiasm and scientific creativity. More than anyone else Dr. Nibler has shown me that the good in science is a matter of attitude and how you choose to interpret your results. Another is analytical thought; I have never seen someone with better problem solving abilities and I have done my best to learn this skill. There is no question that Dr. Nibler is, in every sense of the word, my mentor.

TABLE OF CONTENTS

TABLE OF CONTENTS (continued)

LIST OF FIGURES

LIST OF FIGURES (Continued)

Page

LIST OF TABLES

LIST OF APPENDICES

Page

Dedication

This thesis is dedicated to the two most important people in my life; my wife, Lan, and our daughter, McKenzie Marie. Lan has been a constant support in my pursuit of a career in science – even temporarily giving up her own career dreams so that we could be together while I attended graduate school. I will be forever indebted to her for her patience and understanding. McKenzie is special. It is hard to say how much she means to me and how much she has put my life into perspective. Her life has, in no small way, influenced my decisions and the direction of my career.

High Resolution Ionization-Detected Stimulated Raman Spectroscopy

1. INTRODUCTION

1.1 Motivation for Experiment

Over the years the research interests of Dr. Joseph Nibler's spectroscopy lab at Oregon State University have centered around the study of molecular cluster properties using coherent Raman spectroscopy. Clusters are interesting because they fit in a size range that is in between bulk materials and isolated molecular systems. They therefore behave in a unique way. To a large extent, thermodynamic properties such as phase changes in large aggregations ($N > 100$) have been the focus of the experimental studies. For the vibrational transitions seen in such cases it is not necessary to use lasers with resolution greater than approximately 0.05 cm^{-1}. However, in order to further understand the transition from a single molecular unit to clusters on the order of a few dozen molecules, it is desirable to have much higher resolution so that rotational structure can be resolved. With rotationally resolved spectra, molecular structure can often be determined without ambiguity.

Cluster studies in the range of 2 - 100 molecules are important because information about the molecular interactions as well as the buildup geometry can be determined. This kind of information can be used, for example, in modeling atmospheric processes such as droplet formation or ozone production (e.g. from studies of the $(O_2)_2$ complex). From a molecular dynamics point of view these small clusters are also

interesting because with high resolution, barriers to internal rotation and tunneling effects can be studied. The spectral splittings and patterns resulting from such effects are important for gaining a more detailed understanding of the intermolecular potential surfaces.

A basic problem in studying these clusters is detection sensitivity. The only practical way to make these particles is in a molecular jet. Under ideal conditions only a small percentage of the gas condenses to form a cluster of any specific size. Even if high enough densities can be obtained so that a Raman signal can be seen, it is very difficult to assign a complex rotationally resolved spectrum due to the many constituents in the sample region.

The work contained in this thesis addresses both of these problems. The following chapters describe a new ionization detected stimulated Raman spectroscopy (IDSRS) experiment that was designed and constructed to take rotationally resolved Raman spectra at densities that are expected for small molecular clusters. The next Chapter is devoted to the design and construction of the experiment. Chapter 3 shows some initial data that were taken during the testing and calibration stages. Chapter 4 is a reformatted version of an article that was published in the Journal of Chemical Physics and Chapter 5 is a study of AC Stark effects which will be submitted to the same journal.

1.2 Historical Development

The development of ionization detected stimulated Raman spectroscopy (IDSRS) was a natural extension in the search of higher sensitivity for Raman spectroscopy in low

density gas samples. In the late 1970's and early 1980's an increased interest in the spectroscopy of low density supersonic molecular jets meant that the conventional Raman methods such as stimulated Raman spectroscopy (SRS) and coherent anti-Stokes Raman spectroscopy (CARS) became increasingly inadequate due to insufficient sensitivity.

CARS is a useful spectroscopic method for molecular jets since it has the advantage that the lasers can point probe the sample at the focal overlap region. This is helpful since specific regions can be probed in the jet as it expands. The disadvantage of CARS is that the signal is proportional to the square of the number density, so as the density decreases the signal diminishes very rapidly. For example, a static gas sample typically may have a pressure of approximately 10 torr, which gives a density of $3.5 \cdot 10^{17}$ cm^{-3}, whereas the density in a pulsed molecular jet may be on the order of 10^{12} cm^{-3}, about 10^5 times lower density. This sample density would give a CARS signal in the jet that is 10^{10} times lower than the static cell. CARS would be even more problematic for one who wanted to study small molecular clusters (on the order of 2 - 20 molecules) whose densities are in the best case 10 times lower than that of the monomer. Clearly, a more sensitive method of detection is needed if Raman spectroscopy is to be a useful tool for elucidating chemical properties in molecular jets.

Improved sensitivity came in 1981 when Cooper et al. performed an experiment[1] (Figure 1-1 a) that is basically resonant Raman spectroscopy competing with resonantly enhanced multiphoton ionization (REMPI). In this so-called "ion dip" experiment[2] one laser was tuned to a resonant multiphoton ionization (MPI) transition of I_2 at its room temperature vapor pressure of <1 torr ($3.2 \cdot 10^{16}$ cm^{-3}). A second laser was tuned such that its frequency matched the frequency difference between the resonant electronic state and a

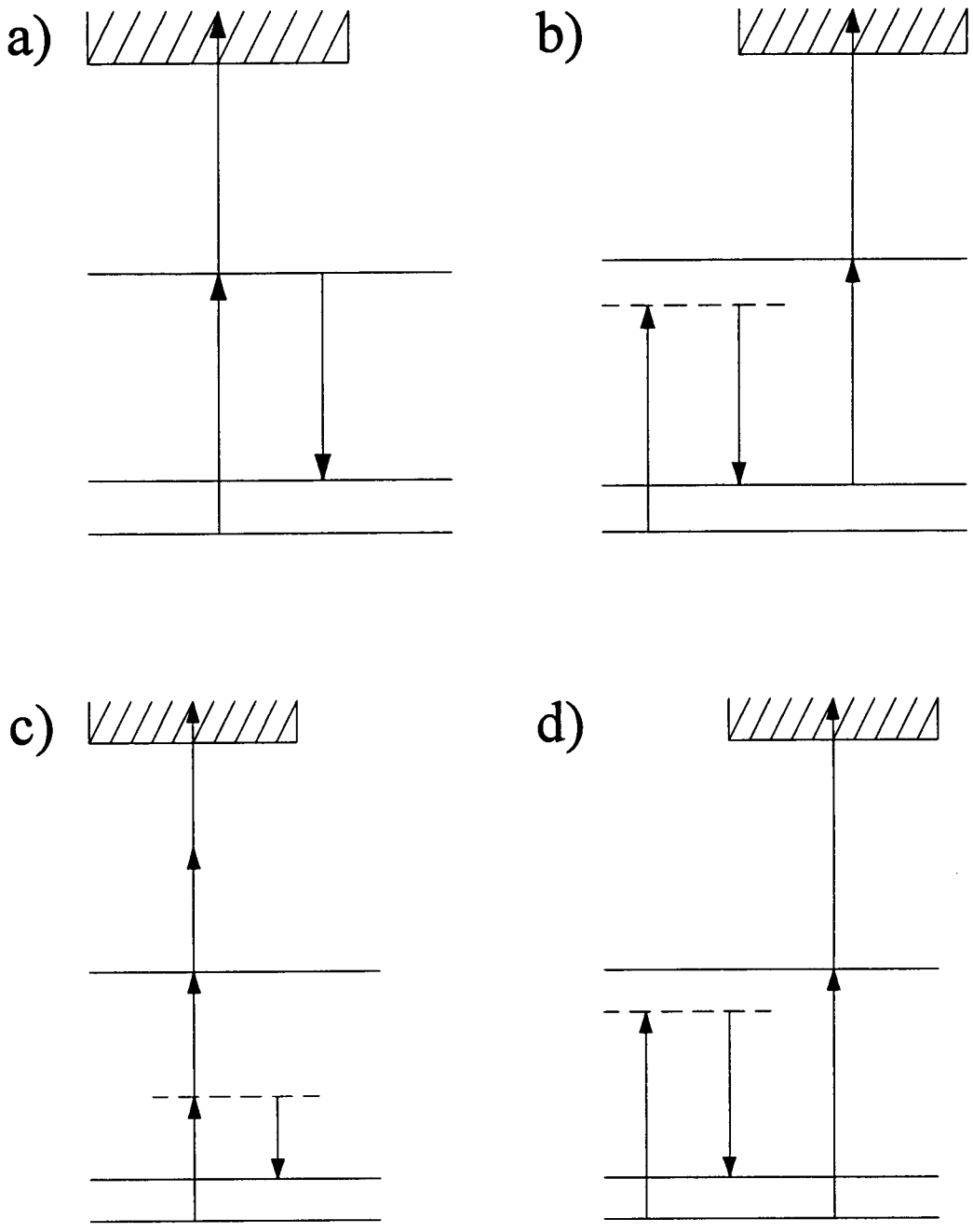

Figure 1-1 Energy level diagrams for experiments performed by: a) Cooper et al., b) Esherick and Owyoung, c) Bronner et al., d) Felker et al. Note that b) is different than d) since the UV step originates from the Raman pumped level (detecting an increase in population for the upper state) whereas in d) the UV starts from the ground state and therefore probes the depletion of the ground state.

lower lying vibrational level. As the second, or Stokes laser, was scanned across a resonant transition the MPI signal showed a dip in the otherwise constant level. Current from the generated ions was collected with two biased electrodes and monitored as a function of frequency. For the strongest ion dips, a depletion of up to two-thirds the parent ion signal was seen. Interestingly, they mention that larger ion dips may be possible by using "coherent excitation conditions whereby π pulses would transfer all population in the (upper electronic state) into (the lower vibrational state)."[2]

In 1983, Esherick and Owyoung used the REMPI process in a static cell to detect population increases in the $X\ ^2\Pi_{1/2}(v = 1)$ state of NO produced by stimulated Raman scattering.[3] "Ionization-detected stimulated Raman spectroscopy" (IDSRS), as they called it, is novel for several reasons. First, since the ionization signal originated from an upper vibrational state (Figure 1-1 b), the signal had inherently less background noise due to the fact that the relative thermal population at room temperature is approximately 10^{-4} in comparison to the ground state. This results in an extremely low ionization signal unless the Raman pumping lasers are tuned exactly on resonance. Second, they increased the sensitivity 1000 fold over conventional stimulated Raman scattering experiments. Third, they used very high resolution (0.003 cm^{-1}) lasers for the Raman pumping step. At the time this kind of resolution was novel in its own right. Detection of the signal was relatively insensitive since they used two biased electrodes that measured the current generated by the ions. This method also has the disadvantage that it does not allow for mass analysis of the ions generated. Nevertheless, this proved to be a landmark experiment for highly sensitive Raman spectroscopy.

Esherick and Owyoung continued this experiment to examine the very weak ν_8, $\nu_1 + \nu_6$ Fermi dyad in benzene at high resolution in a molecular jet.[4,5] Due to the low detection limit ($3 \cdot 10^{15}$ cm^{-3}) and high resolution, they were able to completely analyze all the rotational structure in both modes for the first time. The combination of the cold jet and selection rules for the Raman and UV steps simplified the spectrum and allowed assignments to be made for all rotational branches.

Later, in 1984 Bronner et al. showed that the detection limit of the ion dip method can be as low as 10^{11} cm^{-3} for non-resonant Raman spectroscopy.[6] Their method was similar to that of Cooper et al. except that the ionization laser was tuned to a resonant 2 + 2 photo-ionization of benzene (Figure 1-1 c). This laser also served as the pump source for the Raman transition. A second laser was used for the Stokes beam, pumping molecules to the ν_1 vibrational state and depleting the resonant ionization signal by more than 10% with high intensities. Resulting ions were accelerated through a 850 V potential and allowed to drift one meter where they were detected with an amplified open multiplier with an unspecified gain.

Felker and coworkers have refined the ion dip technique for non-resonant Raman spectroscopy.[7] Their experiment differs from Bronner et al. in that they use two lasers for the stimulated Raman step and a third laser is tuned to ionize the molecules in the ground state approximately 10 ns after the Raman pump (Figure 1-1 d). Ion dip experiments are preferred in Felker's lab over the IDSRS experiments of Esherick and Owyoung since the frequency constraints are relaxed. This means that larger Raman scan ranges can be performed without constantly re-tuning the UV to match a resonance. Felker's work has concentrated on the vibrational Raman spectroscopy of small aromatic clusters in the

range of 2-30 units.[8,9,10] Recently they have done a great deal of work on intermolecular vibrations[11,12,13,14] and have mapped the rotational band contours[15] of these van der Waals clusters.

Felker's experimental apparatus differed from the above early experiments as well. A Wiley-McLaren[25] time of flight mass spectrometer (TOFMS) added a mass specific Raman spectroscopic capability. Also, higher detection sensitivity was obtained from the use of microchannel plate detectors. These detectors typically have a gain of 10^6-10^7 in the linear region of amplification[16] so this was a significant improvement over the biased electrode arrangement.

The experiment described in this thesis combines the high resolution of Esherick and Owyoung with the high sensitivity and mass specific capability of Felker's experiments. The purpose of this work was to construct the experimental apparatus and demonstrate the capabilities of the experiment. With the custom laser system used for the stimulated Raman pumping, we have been able to show that at sufficiently low laser energies, instrumental linewidths of 30 MHz (0.001 cm^{-1}) are possible. This alone is a significant achievement for Raman spectroscopy. With the use of sensitive microchannel plate detectors, it has been possible to take spectra at state densities of 10^{10} cm^{-3}. The results presented in this thesis show promise for further experiments involving small molecular clusters, photoproducts, and Raman spectroscopy of excited state molecules.

2. THE IDSRS EXPERIMENTAL APPARATUS

2.1 Overview

Figure 2-1 displays the ionization detected SRS experimental layout. The high resolution Raman lasers are provided by the Continuum neodymium: yttrium-aluminum-garnet (Nd:YAG) laser and the pulse amplified, tunable, Coherent 699-29 ring dye laser. For the UV ionization, a separate YAG is timed to the experiment and supplies the pump for a broad band tunable dye laser. The output of the dye laser is sent into an active frequency doubler and is doubled with a beta-barium-borate (BBO) or potassium diphosphate (KDP) R6G crystal, depending on the desired UV wavelength. After the doubler, a harmonic separator dumps the fundamental and passes the doubled light which is then brought into the vacuum chamber counter-propagating to the Raman pumping beams. All laser beams are brought to a common focus between the acceleration plates in the vacuum chamber, approximately five centimeters from the jet nozzle. Upon photo-ionization, the ions are accelerated through a 3000 volt potential and then drift in a field free region approximately one meter down the time of flight tube before being detected by a microchannel plate detector. The resulting amplified signal is sent to a Tektronix 2440 oscilloscope for monitoring and a Stanford Research SR250 boxcar integrator for processing. For UV scans a computer program collects and stores the spectra via a Stanford Research SR245 computer interface, while for Raman scans the data is collected by the ring laser computer, directly from the last sample out on the boxcar. All the data are then transferred by disk to a separate computer for analysis.

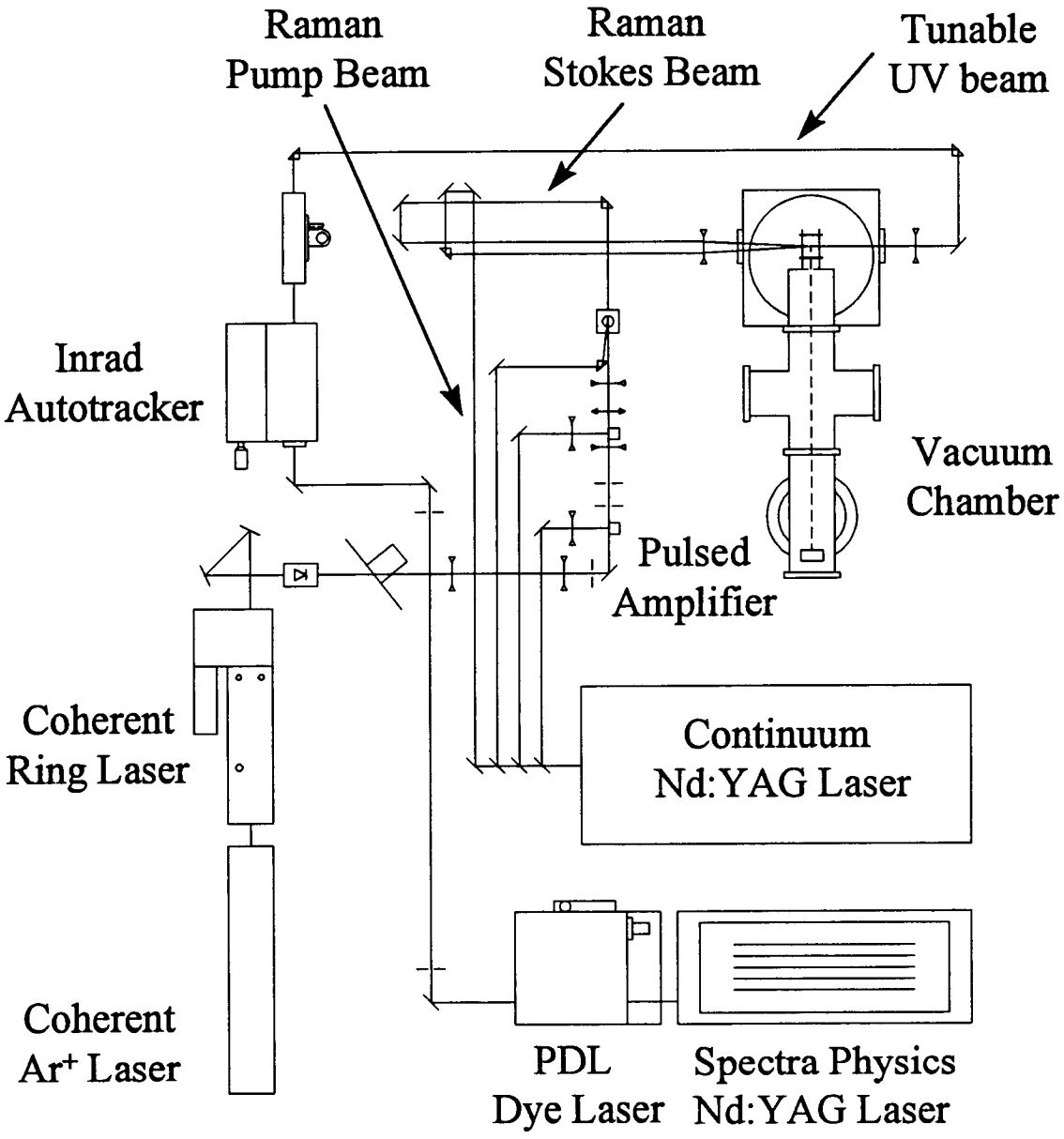

Figure 2-1 Layout for the IDSRS experiment.

2.2 Laser Systems

2.2.1 Raman Pumping Source

2.2.1.1 **Continuum Nd:YAG laser**

The heart of the high resolution IDSRS laser system is the Continuum Nd:YAG laser and is described in detail in reference 17. Continuum custom built a two meter cavity with a preamplifier and amplifier to deliver a 200 mJ, 50 ns pulse of 532 nm light which corresponds to a spectral linewidth of 8.8 MHz (see Appendix A.). To ensure that the YAG runs in a single longitudinal mode, a Lightwave Series 122, 50 mW narrow band, diode pumped, Monolithic, Isolated, Single-frequency, End-pumped Ring (MISER)[18] laser is injection seeded into the cavity. The MISER cavity is made of a single Nd:YAG crystal and is frequency stabilized with precise temperature control which in effect controls the index of refraction and cavity length of the laser cavity.

2.2.1.2 **Continuum Frequency Stabilization**

Since the seeder has the capability of being tuned externally by changing the temperature of the monolithic crystal, we can lock the laser to the side of an absorption line in iodine.[19] When Harrison et al.[19] developed the locking procedure it was believed that the voltage resolution sent to the seeder was 0.5 mV which corresponds to a frequency shift of approximately 1 MHz. Unfortunately, the voltage resolution of the AD board in the SRS 245 computer interface has 2.5 mV resolution.[20] This corresponds to a

frequency change of 5 MHz or 0.00017 cm^{-1} in the IR and 0.00033 cm^{-1} at 532 nm, which is on the order of the linewidth of the laser. A new locking procedure was written that allows the laser to drift within a specified range of ± 0.001 cm^{-1} without correction. Only if the frequency gets out of this range is there a minimal correction voltage applied to the seeder.

When the locking procedure is used, it is necessary to use three boxcar integrators. One boxcar is needed for data acquisition and the other two are used for monitoring the transmission through an iodine cell and monitoring the YAG laser intensity for normalization of the absorption signal. The integrated signals from the two boxcars are sent to a Stanford Research SR225 signal processor for analog normalization. This could be done just as well with a computer but in this experiment the signal processor was used to simplify the program. This normalized signal is then sent to the computer interface, digitized and then sent to the computer. All the cable connections for the boxcars, laser control and locking are shown in Figure 2-2 for Raman and UV scans.

An alternative approach to the locking procedure used above would be to use a voltage divider at the input of the seeder. The advantage of this would be that there would be tighter control on the frequency drift. This method is feasible in principle, but with voltage changes on the order 0.1 mV at the seeder controller, noise starts to become a concern.

One possible source of noise that could contribute to frequency instability is Johnson noise due to the resistors in the voltage divider. The rms voltage generated by a resistor is calculated from the expression[21]

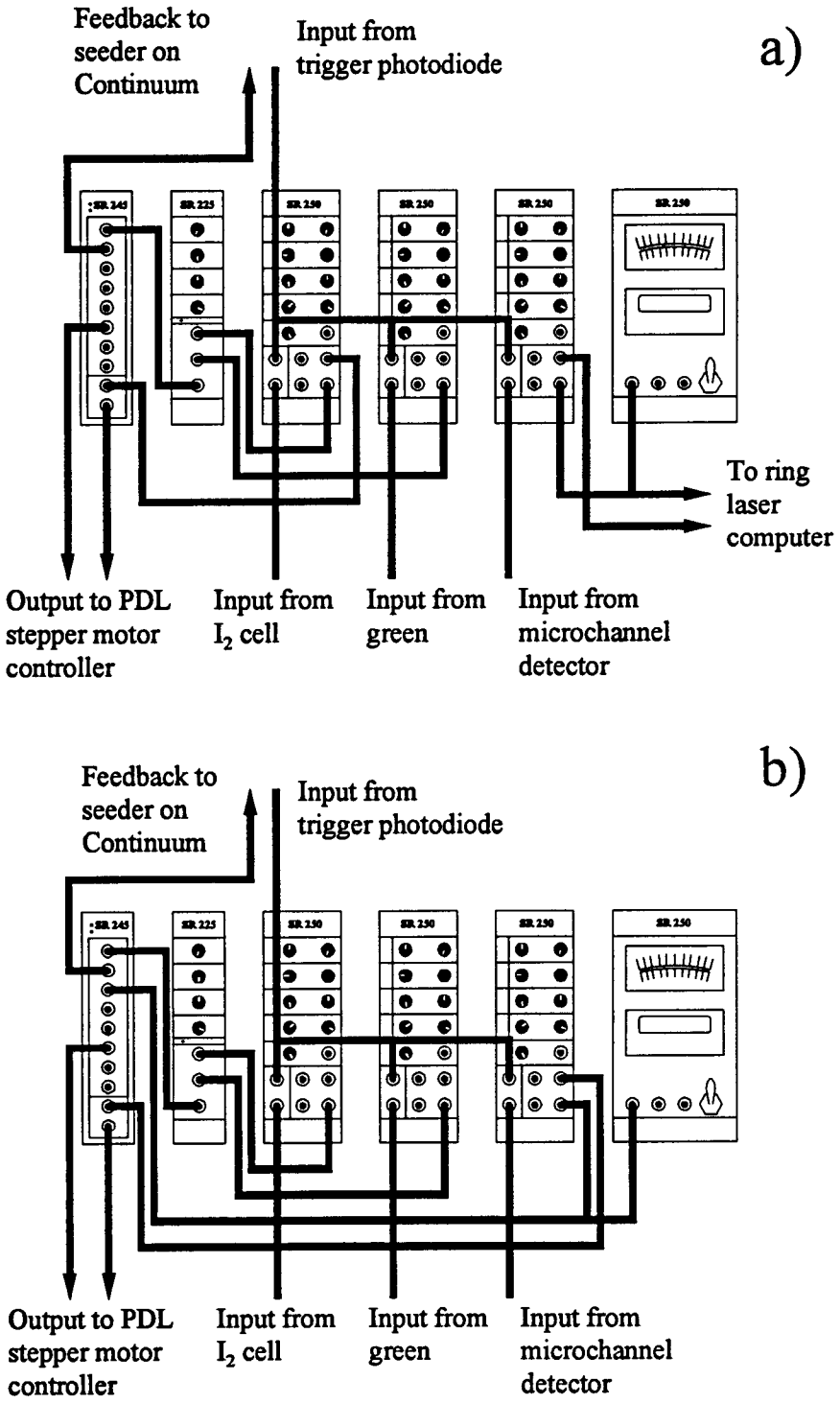

Figure 2-2 Wiring diagrams for data acquisition and locking of the Continuum with a) ring laser scans. b) UV scans.

$$V_{rms} = \sqrt{4kTR\Delta f} \qquad (2.1)$$

where $k = 1.381 \cdot 10^{-23}$ J/K is Boltzmann's constant, T is the temperature in Kelvin, R is the resistance in Ohms and Δf is the bandwidth of the noise in hertz. In our case the resistance is approximately 1 kΩ and the temperature is roughly 300 K. The bandwidth of the noise takes more thought. Only noise that occurs on a time scale longer than the response time of the seeder laser (1-10 seconds[18]) will cause frequency instability. This means that high frequency noise will average out to zero. It is hard to imagine that frequencies above 100 Hz will effect the frequency stability of the laser so this can be used a upper bound for calculating Δf. A rms voltage of $4 \cdot 10^{-8}$ V is calculated with the above values which shows that Johnson noise is completely negligible in comparison to the voltages sent by the source. A noise source of more concern is RF noise picked up by the BNC cables. Some of this can be eliminated by using a low bandpass filter for frequencies above 20 Hz.

With the computer controlled locking procedure adding a minimal frequency jitter, the bandwidth of the laser will be 9 MHz plus another 6 MHz from the dither on the end mirror of the cavity which is used for locking the cavity to the seeder laser.

2.2.1.3 **Coherent Ar^+ and Ring Laser**

The tunable Stokes beam is furnished by the Coherent 699-29 ring dye laser. This laser is pumped by the 7 watt output of a Coherent I-90-6 Argon ion laser. Typically 50-500 milliwatts of tunable CW output are obtained, depending on the dye used. Output from the laser is sent through a Faraday isolator and a chopper wheel before going to the first stage of the amplifier.

Pulse amplification is needed since the energy of the ring laser is approximately $5 \cdot 10^{-5}$ mJ for the 50 ns pulse duration of the Continuum YAG. Typically we need 1 to 5 mJ/pulse so we must amplify the Stokes beam by a factor of approximately one million to have adequate energy for this experiment. Amplification is accomplished with three consecutive dye amplifier cells. The first two are transversely pumped and the last is longitudinally pumped to help clean up the beam spatially and make it more cylindrically symmetric. A telescope is placed between the second and third amplifiers and serves two purposes. One is to expand the beam to the same size as the pump beam for the last amplifier stage and the other is to provide an adjustment to collimate the beam. Collimation of the dye laser beam will be discussed in more detail in section 2.2.3.1.

2.2.2 UV Ionization Source

2.2.2.1 **Spectra Physics Nd:YAG and PDL**

The QuantaRay GCR-170 is an unseeded high power Nd:YAG laser. Its function is to provide a 532 nm or 355 nm pump for the PDL dye laser depending on which dye is needed. For coumarin dyes such as C-500, the output of the YAG is 355 nm while for rhodamine dyes the 532 nm output is used. Typical powers for the 532 and 355 output are given in Table 2-3 for several lamp energy settings when the laser was new.

A computer provides wavelength control of PDL laser via the Stanford Research computer interface and Unidex, Aerotech Inc. stepper motor controller. The computer program takes the direction and scan distance, computes the number of steps and then

issues clock and direction commands to the SRS computer interface. The computer interface then sends TTL pulses to the clock and direction inputs on the stepper motor controller. A significant improvement in the accuracy of scanning the PDL dye laser would be the

Lamp Energy	355 nm power (mJ/pulse)	532 nm power (mJ/pulse)
7		17.5
7.5	25	60
8	60	110
8.5	115	190
9	175	275
9.5	210	350
10		350

Table 2-1 Output Powers of the Spectra Physics GCR-170 YAG laser.[22]

addition of a digital encoder on the grating drive. Currently the program just issues the stepping commands without actually checking to see where the laser frequency really is. An encoder would eliminate this problem and give better positioning reproducibility as well as calibrated scans.

2.2.2.2 **Inrad Autotracker**

The Inrad Autotracker is a active frequency doubler. This means that as the frequency of the fundamental beam from the PDL dye laser is changed, an error signal is generated internally that optimizes the crystal angle for maximum doubling efficiency. To

generate the error signal, a part of the doubled beam is picked off with a beam splitter, filtered from the fundamental, and focused onto a split photodiode. As the frequency changes the intensity distribution on the detector changes so that one of the diodes sees more light than the other. These error signals are sent to the control box which then compensates by adjusting the crystal angle so that the intensity remains equal on both photodiodes.

Alignment is accomplished by sending the laser through the center of the input and output apertures. In practice, it is a bit more complicated to obtain reliable tracking and the following procedure seems to be a reliable method.

Autotracker Alignment Procedure

1. Optimize the doubled output visually
2. Place the proper attenuation filters in the beam so the detector is not saturated
3. Using the micrometer on the detector, balance the signals on the display
4. While monitoring the display signals, slowly tune the angle of the crystal in both directions to see if the signals are balanced on both detectors. If the detector is properly adjusted the display should look like Figure 2-3
5. Change from manual to auto

The magnitude of the error signal can vary depending on the wavelength. For example, around 520 nm (coumarin 500) the Autotracker works quite well but as the laser is tuned to the red, to approximately 540 nm, the error signal gets much smaller and stable locking is more difficult. This is because the BBO crystal is only a few millimeters long so the

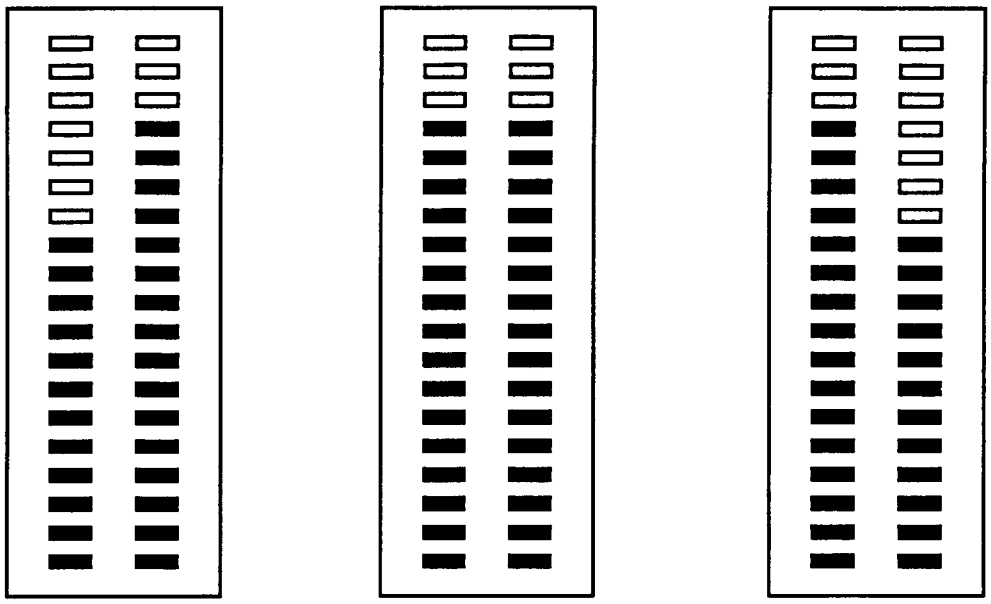

Figure 2-3 Properly adjusted Autotracker LED signals. The left and right views show what the LED's look like when the crystal is tuned to one side of the maximum or the other. The middle shows the locked position.

beam deviation is small. It should also be noted that the position of the lens that focuses the UV on the split photodiode is a critical factor in the alignment and can sometimes be misleading. When the dye is changed to a new wavelength more than 30 nm from the old dye, the focus should be checked. It is possible that the focus has changed due to the dependence of the index of refraction on the wavelength and the Autotracker will not lock properly—if at all. This can be especially confusing if the wavelength change is to the blue, since the focus can move to in front of the detector and the Autotracker will anti-lock because the error signal is reversed and drives the crystal from the locked position.

2.2.3 Spatial Overlap Alignment of Laser Beams

A great deal of time and effort was spent on developing a reliable alignment procedure that ensured a double resonance signal would be obtained. The result of this work showed that the two most critical factors in the alignment of the double resonance experiment are:

- Good transverse spatial overlap at the focus.
- All laser beams must have a common focus.

The following section describes the methods developed to obtain these two criterion.

2.2.3.1 **Alignment Procedure for IDSRS Experiment**

The alignment procedure begins with getting all the beams roughly aligned parallel without any focusing optics in place. The pump and Stokes beam are brought into the vacuum chamber parallel and offset by approximately one centimeter and the UV beam counter propagates in the middle of the two Raman beams. Typically the lens for the Raman beams is placed in the path first and then the lens for the UV. Care must be taken at each step to insure that the lenses do not steer the beams when they are inserted since this would introduce coma in the focus and also misalign the system if the lens position is moved. In order to assure that the beams are overlapped transversely at the focus, a piece of brass shim stock is placed at the center of the acceleration plates and a hole is burned with the green beam from the Continuum. The Stokes and UV beams are then aligned so that they pass through the hole. This should require very small adjustments if care was taken in the rough alignment.

Once all the beams are through the pinhole it is necessary to check if they have a common focal point. A series of burns through the shim are made at different lens positions and the corresponding burn time is measured. The minimum burn time indicates that the lens is positioned at the optimal focal distance. Bringing both of the Raman pumping beams to a common focus is in theory straightforward since their wavelengths only differ by about 2000 cm^{-1}.

To calculate the difference in focal length for the two Raman beams we use the relation

$$f_\lambda = f_{589}\left(\frac{n_{589}-1}{n_\lambda - 1}\right) \qquad (2.2)$$

where f_{589} is the focal length designated by the manufacturer (at the wavelength of the yellow sodium line) and n_{589}, n_λ are the indices of refraction at 589 nm and the wavelength of interest. For most common materials the index of refraction is inversely related to the wavelength as shown in Figure 2-4 for quartz. If we use (2.2) and Figure 2-4 to calculate the ratio of the focal lengths for the pump and Stokes beams with a 2000 cm^{-1} Raman shift we find that

$$\frac{f_{595}}{f_{532}} = \frac{n_{532}-1}{n_{595}-1} = \frac{0.4607}{0.4582} = 1.006. \qquad (2.3)$$

This means that the Stokes beam has a 1.5 mm longer focal length than the pump beam for a 250 mm focal length lens. This is a small difference and should not need adjustment. In practice the focal length is typically 0.5 cm longer than the green beam. It is difficult to say why this is, but there are several possibilities. One is that the spatial beam quality is

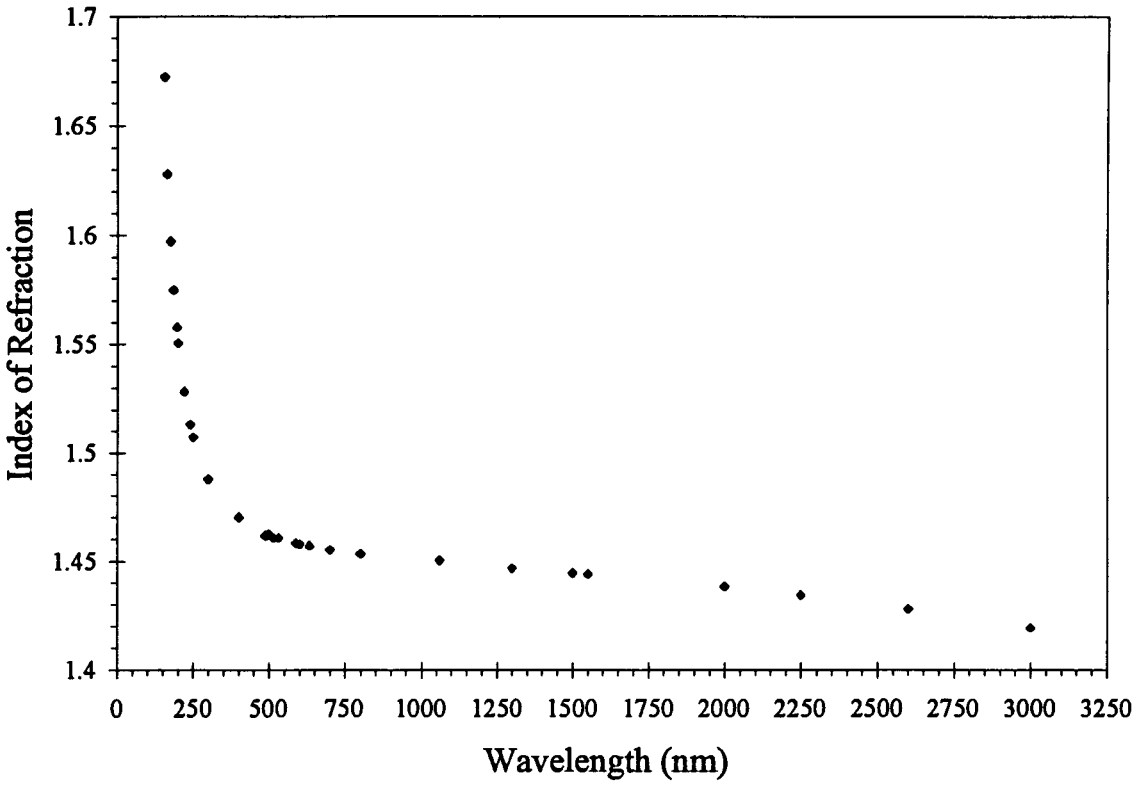

Figure 2-4 Index of refraction for fused silica (non-crystalline quartz).[23]

not very good. There are several hot spots in the beam and this could change the effective focal length. Most likely, the beam is not collimated uniformly over the entire beam. This could be caused by the amplifier stages; for instance the light emitted from the dye cell is not a point source for the telescope in the amplifier. The effect of this is to cause spherical aberration in the beam so that it can not be collimated. Another cause could be small density fluctuations in the dye cell or concentration effects that would cause astigmatism and effect the beam divergence from the dye cell. Regardless, the Stokes beam can be brought to the focus of the green by adjusting the telescope in the amplifier chain. Figure 2-5 shows several burn plots that demonstrate the process of bringing the Stokes beam to

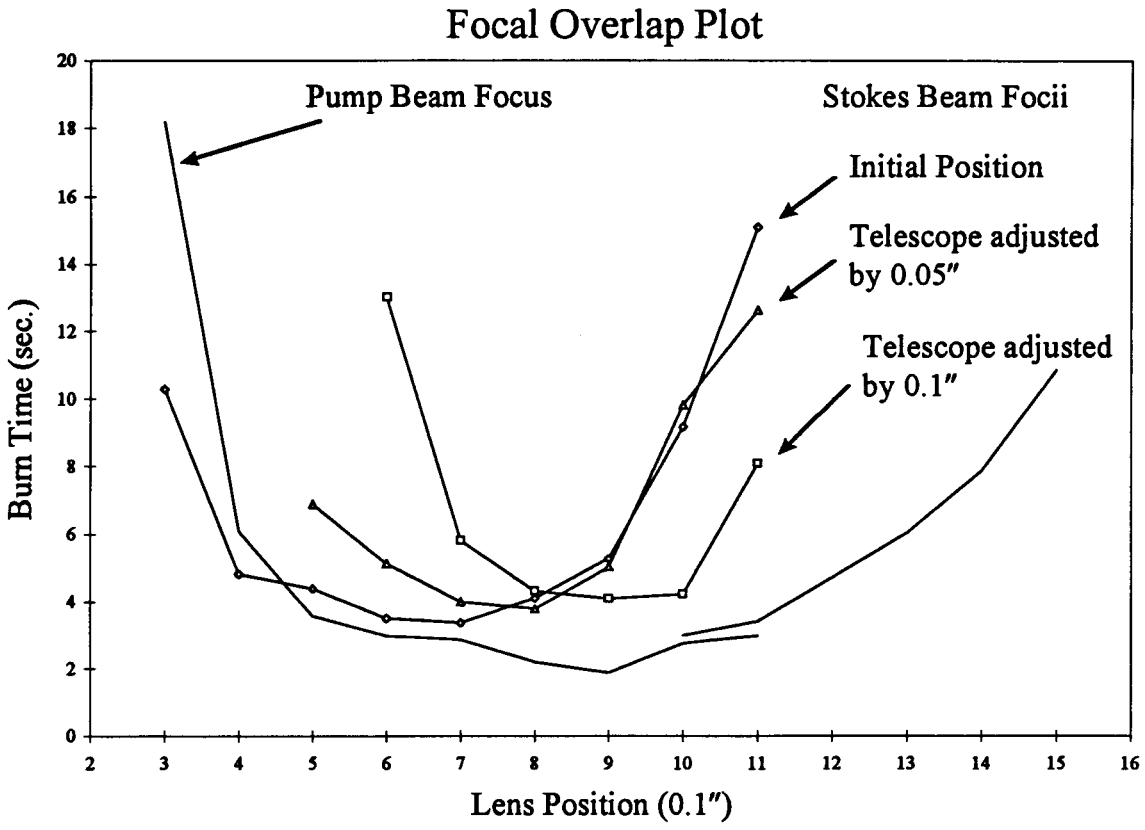

Figure 2-5 Focal overlap adjustment for the Stokes beam and the green pump

a common focus with the green. After any adjustment of the telescope, the alignment must be rechecked from the beginning since the beam can be steered if it is not centered on the optics.

Since the UV is typically at 260 nm to 280 nm and the Raman beams are roughly twice that wavelength, it is difficult to bring all three laser beams to a common focus using one lens. The ratio of the UV and green focal lengths in this case is

$$\frac{f_{250}}{f_{532}} = \frac{0.4607}{0.5075} = 0.91. \qquad (2.4)$$

This means that for a 250 mm focal length lens, the UV would be approximately one inch shorter. Small differences in the focal lengths can be compensated by changing the divergence of the incident beams as in the case of the Stokes beam, but differences as great as this are difficult to compensate for. In order to avoid this complication, the UV is brought to the sample region through a separate lens counter-propagating to the Raman pumping beams. This also allows us to more carefully overlap the focal volumes of the three beams. Not only that, but it also permits us to use a much shorter focal length lens for the UV to ionize molecules such as nitrogen, oxygen, or carbon dioxide.

2.2.3.2 **Characterization of the Laser Beam Focus**

To describe the propagation of the laser beams we assume that the electric field is a plane wave that has a transverse Gaussian amplitude distribution given by

$$E(x,y) = E_0 e^{-\frac{x^2+y^2}{w^2}}, \qquad (2.5)$$

where E_0 is the maximum amplitude at the origin and w is the beam waist defined as the half width at an intensity of E_0/e. When the beam is sent through a lens, the wave front can be approximated as spherical and the intensity profile is modified to include the fact that the beam waist changes in the z-direction,[24]

$$E(x,y,z) = E_0\left[\frac{w_0}{w(z)}\right]e^{-\frac{x^2+y^2}{w(z)^2}}. \qquad (2.6)$$

Here, w_0 is the minimum beam waist at the focus and

$$w(z) = w_0\left[1+\left(\frac{\lambda z}{\pi w_0^{\,2}}\right)^2\right]^{\frac{1}{2}} \qquad (2.7)$$

is the waist as a function of the distance z from the focus. It is possible to determine $w(z)$, and thereby w_0, both experimentally and theoretically. The purpose of this section is to compare the theoretical results with the measured values.

To determine the minimum beam waist experimentally, a razor blade is moved across the beam at several distances z from the focus and the intensity is measured as a function of the razor position, x, perpendicular to the beam axis as shown in Figure 2-6. These data are then fit to the integrated intensity

$$I_{tot}(x,z) = I_0\left[\frac{w_0}{w(z)}\right]^2 \int_{-\infty}^{x}\int_{-\infty}^{\infty} e^{-2\left(\frac{x'^2+y^2}{w(z)^2}\right)}\,dy\,dx'. \qquad (2.8)$$

For a constant z, the integral over y and the factors in front are all constants so they can be normalized to one which just leaves the integral over x'. This integral evaluates to

$$I_{tot}(x,z) = 1 + erf\left(a(z)\,x\right), \qquad (2.9)$$

where

$$a(z) = \frac{\sqrt{2}}{w(z)}. \qquad (2.10)$$

To determine $w(z)$, we fit our data to (2.9) to find (2.10) for several values of z. Figure 2-7 shows a fit of equation (2.9) to the experimental intensity profile for the green laser beam at a distance z = 8 cm. Using equation (2.7), we can find the minimum beam waist by doing a non-linear least squares fit to the beam waist values at each z. Figure 2-8 shows the result of such a fit to the experimentally measured beam waists taken at one

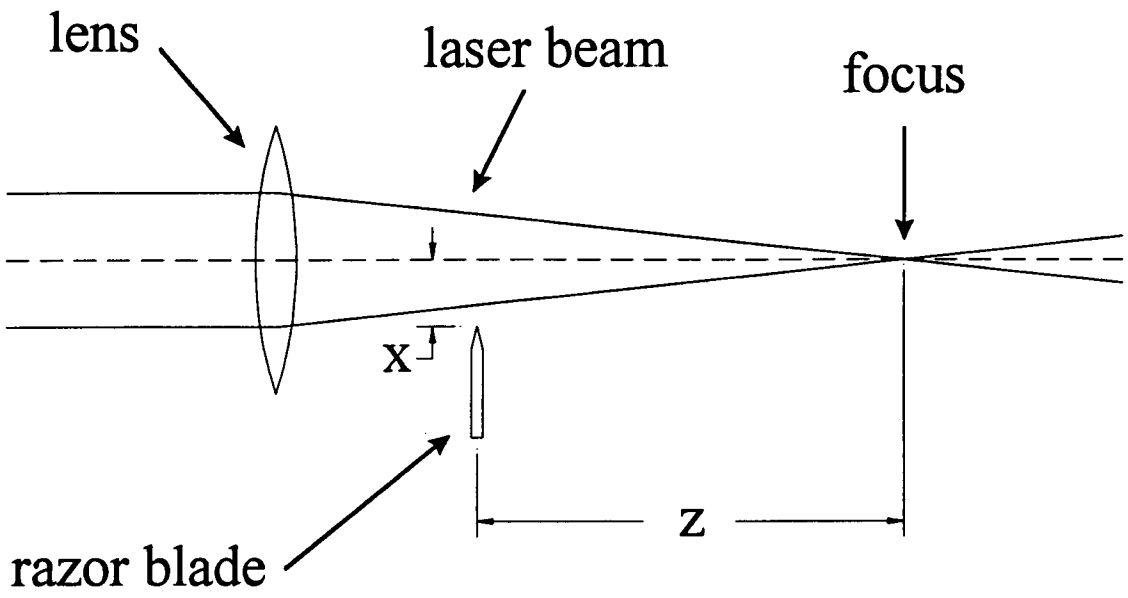

Figure 2-6 Geometry for measuring the beam waist experimentally. The minimum beam waist, w_0, is determined from measuring the transmitted laser intensity as a function of the x-position at different z-positions.

centimeter increments. Implicit in this calculation is that the laser beam has a Gaussian intensity profile, which has the optimum focusing characteristics in terms of diffraction. Essentially this is due to the fact that a Gaussian function Fourier transforms into another Gaussian function. Due to the multistage amplification and apertures in the YAG laser we expect that there is some deviation from a Gaussian beam. Therefore, any measured beam waist must be taken as the lower limit.

The theoretical minimum beam waist can be found from[24]

$$w_0 \cong \frac{2\lambda f}{\pi D} \qquad (2.11)$$

where f is the focal length of the lens at the wavelength λ and D is the diameter of the laser beam at the lens. For our experiment the 0.72 cm diameter, 532 nm beam goes

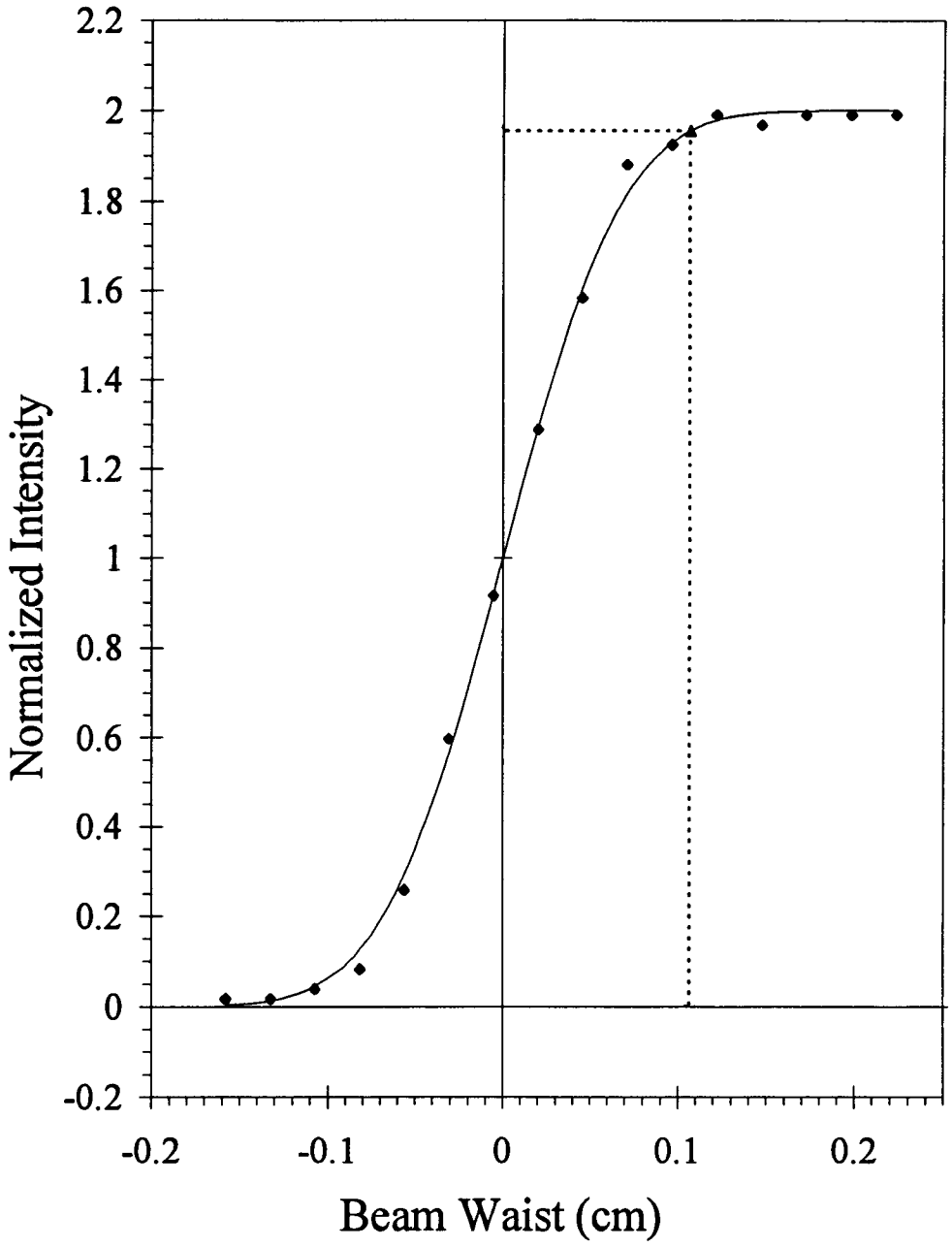

Figure 2-7 Integrated intensity profile of 532 nm laser beam from the Continuum Nd:YAG at a distance of $z = 8$ cm from the focus of a 26 cm (measured) focal length lens. The points show the normalized data measured with a power meter as a razor blade is stepped across the beam waist. The solid curve shows the fit of equation (2.9) with the fitting parameter $a(z) = 13.25$, which gives a minimum beam waist of $w_0 = 12.4 \cdot 10^{-4}$ cm. The two dotted lines indicate the beam waist $w(z)$ and the normalized intensity at that width (1.955).

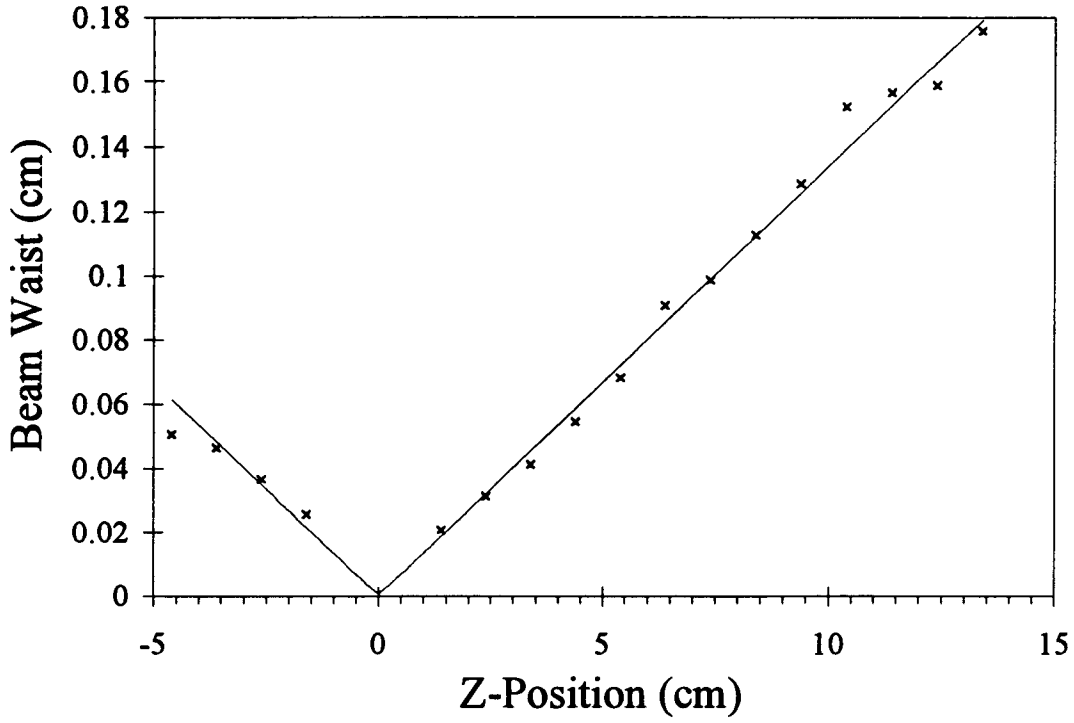

Figure 2-8 A fit to experimentally measured beam waists at different z-positions along the beam axis. The minimum beam waist calculated from this data is $12.7 \cdot 10^{-4}$ cm.

a 26.2 cm focal length lens which gives diffraction limited beam waist of $12.3 \cdot 10^{-4}$ cm compared to the experimentally determined beam waist of $12.7 \cdot 10^{-4}$ cm.

2.3 Vacuum Chamber

2.3.1 General Description

The time of flight vacuum chamber (Figure 2-9) consists of differentially pumped high and low pressure regions. The 12" cube is the high pressure region of the vacuum chamber and is pumped out by a 8 inch Varian diffusion pump model VHS - 6, type No.

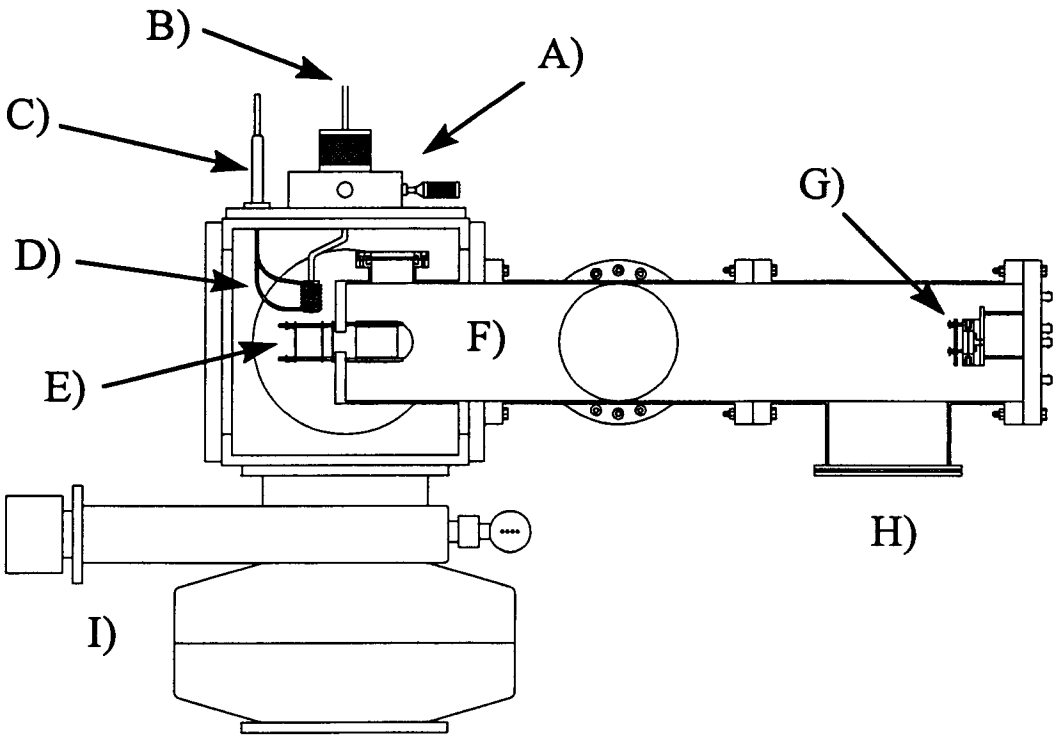

Figure 2-9 Mechanical drawing of the vacuum chamber for the time of flight mass spectrometer. A) X - Y - Z translation stage for nozzle. B) Gas inlet for nozzle. C) Inlet for nozzle cooling tubes. D) Pulsed valve, nozzle and cooling tubes. E) Acceleration and steering plates. F) Time of flight drift region. G) Micro-channel plate detector. H) Vacuum port to Edwards diffusion pump. I) Gate valve, and oil trap for the Varian diffusion pump.

0184. This chamber typically maintains a pressure of 10^{-5} torr while the nozzle is pulsing gas into the system. The pressure is held to a minimum by having the nozzle point straight into the inlet of the Varian diffusion pump. This helps because the gas coming out of the jet makes a straight shot into the pump without hitting the walls of the chamber and subsequently bouncing around several times before going into the pump. Also, the first thing the gas hits in the pump is the cold trap on the pump which is cold enough (- 60 °C) that most of the condensing gasses are not likely to rebound back into the chamber.

A small opening in the cylindrical can inside the cube connects the high and low pressure regions. The ionization takes place just outside this opening and the resulting ions are accelerated perpendicular to the flow of the jet through the hole into the low pressure region. The low pressure region consists of an 8 inch diameter cross and tee and is pumped out by a 160 mm (6.4 in.) Edwards Diffstak Mk2 160/700M diffusion pump that maintains a pressure of 10^{-6} torr while the system is under load. This low pressure region serves two purposes. First, it gives the ions a collision free flight path to the detector and second, it keeps the detector from arcing since the electric field across each of the microchannel plates is approximately 2×10^{6} V/m.

2.3.2 Time of Flight Mass Spectrometer

The design the time of flight mass spectrometer (TOFMS) is that of Wiley-Mclaren[25] except that we use only one acceleration region and a laser for ionization instead of an electron gun. The time of flight process begins with the pulsed valve opening to let the gas into the chamber. When the density in the jet is a maximum, the UV laser fires and ionizes molecules in the middle of the acceleration plates (Figure 2-10). The ions are accelerated half an inch toward the grounded plate and then pass through a hole that is covered by a high transmission wire screen. Approximately three inches from the ground plate two orthogonal sets of parallel plates are used for deflection of the ions. Normally these plates are grounded because if the ions are created right on axis they need no correction to their trajectory. The total drift region is approximately one meter which

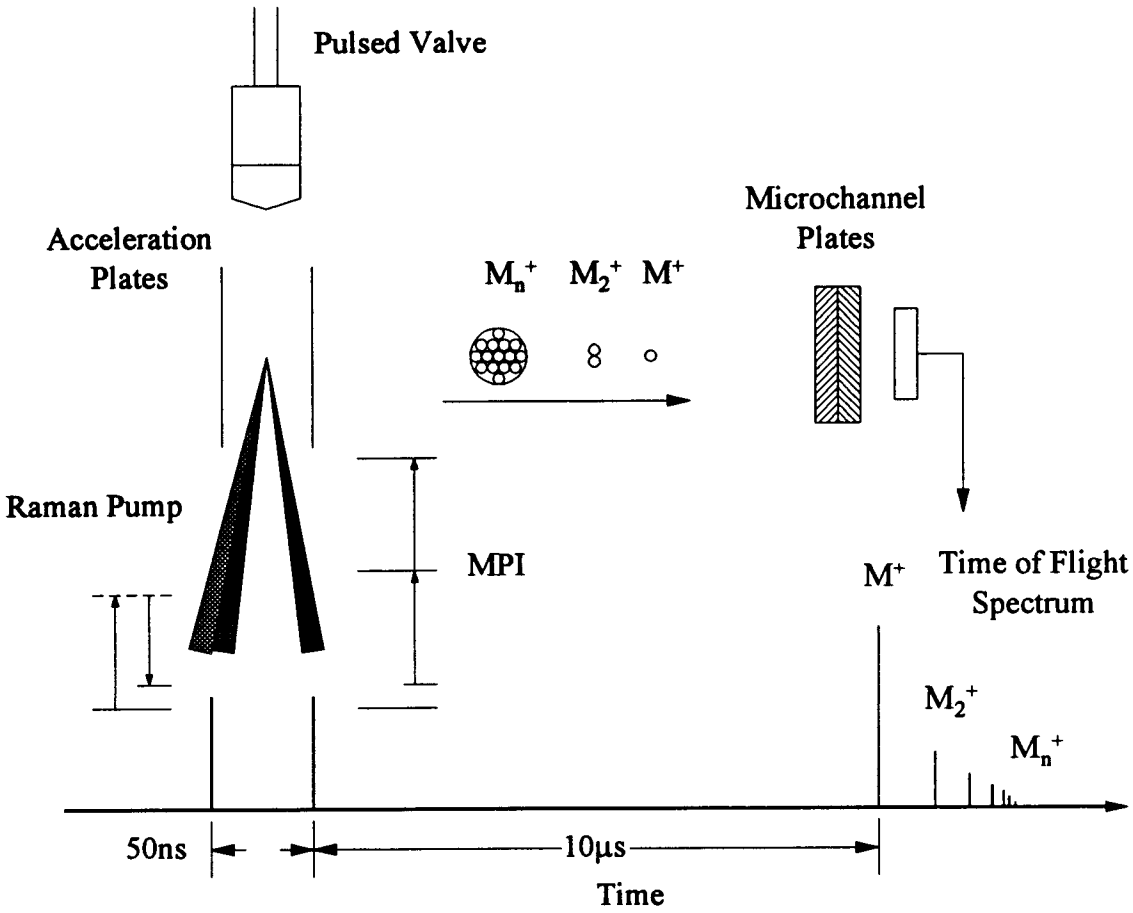

Figure 2-10 Diagram of the IDSRS experimental process. The opening of the pulsed valve starts the experiment. Approximately 1 ms later the Raman lasers fire and probe the sample between the acceleration plates. 50 ns after that, the UV ionizes the molecules and they are accelerated towards the microchannel plate detector. The signal from the channel plates is sent to a oscilloscope where the intensity is recorded as a function of wavelength.

corresponds to a time of flight of about ten microseconds for masses of 100 amu with an acceleration potential of 3000 V.

This experiment is based on the ability to perform mass selective Raman spectroscopy, so it is very important that we be certain that the mass be known for any given time of flight. In practice, the monomer can usually be determined from its spectra

so that all other masses can be calibrated to it using a simple equation relating the time of flight for both particles.

2.3.2.1 Calculation of the Time of Flight

The time of flight for the ionized molecules can be found by adding the time the anion spends in the acceleration region to the time spent in the drift region. To find the time in the acceleration region we first consider the force a charged particle, q, feels in an electric field,[26]

$$\vec{F} = m\vec{a} = q\vec{E}. \qquad (2.12)$$

The scalar electric field in the acceleration region can be written in terms of the scalar potential, Φ, as

$$E = \frac{\Phi}{d_1}, \qquad (2.13)$$

which is just the voltage difference between the two acceleration plates applied with the high voltage power supply. Here d_1 is the distance between the two acceleration plates as shown Figure 2-11. Using (2.13) in (2.12) and solving for the acceleration we get,

$$a = \frac{q\Phi}{md_1}. \qquad (2.14)$$

The time of flight in the acceleration region is found from the kinematic equation[27]

$$d_2 = \frac{1}{2}at_1^2 \qquad (2.15)$$

where d_2 (Figure 2-11) is the distance from the ionization point to the grounded plate. Note that we do not consider the initial velocity of the particles in the direction of

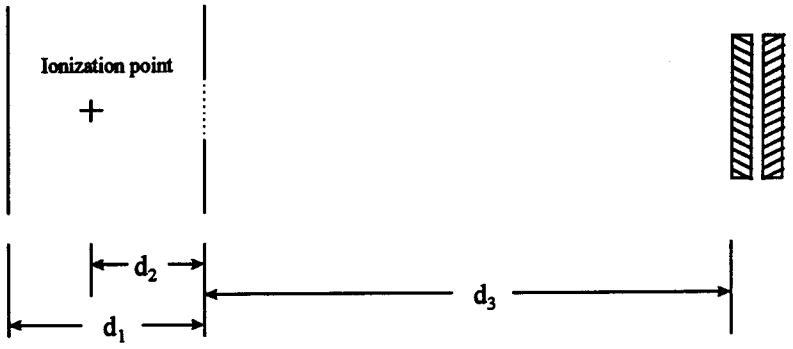

Figure 2-11 Definition of the distances used in the time of flight calculation.

acceleration. This is because the jet is perpendicular to the TOF tube so the velocity component in that direction is essentially zero in comparison to the final velocity of the ion. Solving for t_1 in (2.15) and using (2.14) for the acceleration gives

$$t_1 = \left(\frac{2md_1d_2}{q\Phi}\right)^{\frac{1}{2}}. \qquad (2.16)$$

The time of flight t_2 for the field free region is just the distance the ions drift divided by the final velocity the ions reach at the acceleration plates. To find the final velocity we use the equation

$$v^2 = 2a(x - x_0) = 2ad_2. \qquad (2.17)$$

So the drift time is

$$t_2 = \frac{d_3}{\sqrt{2ad_2}} = d_3\left(\frac{md_1}{2q\Phi d_2}\right)^{\frac{1}{2}}. \qquad (2.18)$$

The total time of flight is just the sum of the two times t_1 and t_2,

$$t = \left(\frac{2md_1d_2}{q\Phi}\right)^{\frac{1}{2}} + d_3\left(\frac{md_1}{2q\Phi d_2}\right)^{\frac{1}{2}}$$

$$= \left(\frac{2md_1d_2}{q\Phi}\right)^{\frac{1}{2}}\left[1 + \frac{d_3}{2d_2}\right]. \qquad (2.19)$$

This is an important equation since we can now calculate the time of flight for a our spectrometer. With $d_1 = 1''$, $d_2 = 0.5''$, $d_3 = 30''$ and $\Phi = 3500$ V, Figure 2-12 a) plots the time of flight as a function of mass. The diamonds along the curve indicate the time of flight for benzene clusters. Note that time separation for the benzene clusters is very large in comparison to the 50 ns width of the pulses. (2.19) also provides an important relation for the identification of unknown mass peaks since if one peak can be positively identified all other masses can be identified by using

$$\frac{t_i^2}{m_i} = \frac{t_j^2}{m_j}. \qquad (2.20)$$

2.3.2.2 **Mass Resolution**

The resolution of the spectrometer is important in this experiment for the spectroscopy of large clusters. We are interested in the largest *n-mer* that can be separated from its *n±1-mer* by at least the width of the pulse. For the same conditions as above, Figure 2-12 b) shows the resolution of our apparatus as a function of mass in amu. For peaks that are separated by the pulse width of 50 ns, we see from this plot that the resolved mass is 183 amu. This means that a molecule of 183 amu could be resolved from an adjacent mass of 182, or one could resolve the cluster M_{183} from M_{182}.

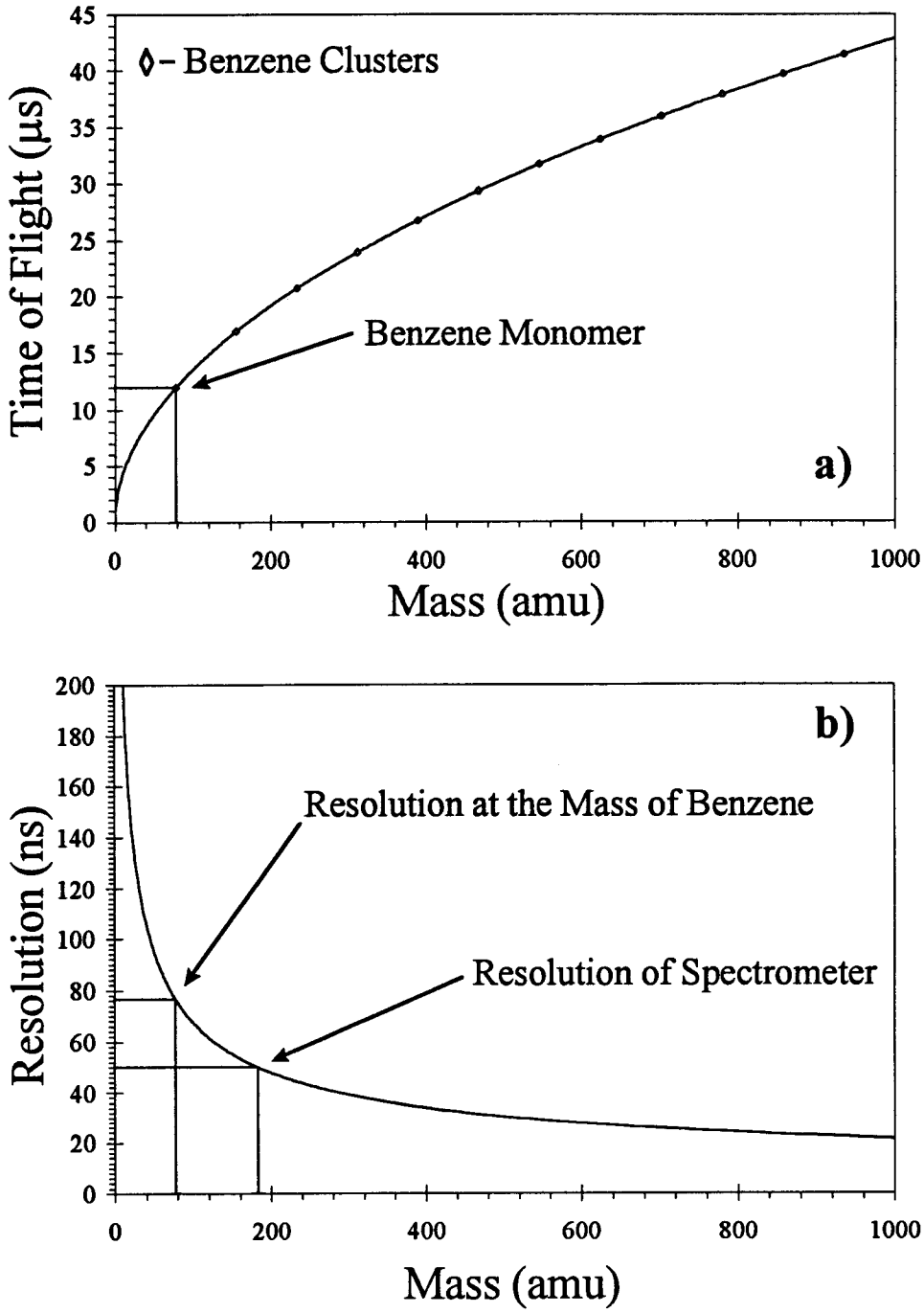

Figure 2-12 a) Predicted time of flight for the mass spectrometer with a 3500 V accelerating potential. The diamonds mark the time of flight for benzene. b) Mass resolution of the TOF spectrometer under the same conditions as above. With 50 ns pulse widths, the resolution is 183 amu. This plot also shows that at the benzene mass we can easily resolve $C^{13}C_5H_6$ from C_6H_6.

2.3.3 Microchannel Plate Detector

Detection of ions produced in our experiment is also very important. High detectability is required in order to see as many of the ions accelerated down the time of flight tube as possible. Microchannel plates were chosen as the amplification devices for several reasons. First, they have a large open area for collecting incident ions. This is an important feature for this experiment since the ions tend to spread out transversely as they drift down the flight tube, so a large collecting surface insures that a minimum of ions are lost. Also, microchannel plates have very fast rise times on the order of 500 ps, which is far better than is needed for our experiment since the pulses we typically see are on the order of 20 - 50 ns in width. Another very important feature of microchannel plates is the sensitivity. When two plates are placed in series (Chevron style) gains of 10^7 are attainable. If ion densities of only a few hundred ions or less per pulse per mass channel are produced, as is the case in this experiment, it is very desirable to have this kind of detection sensitivity.

2.3.3.1 **Mechanical Design**

A mechanical drawing of the detector mount is shown in Figure 2-13. The channel plates are sandwiched by three stainless steel rings that provide electrical contact to the plates. The base ring is bolted to a delrin backing plate that is sits on three threaded rods screwed into the vacuum flange as shown in Figure 2-9. Above the channel plates a grounding screen is used to keep the drift region as field free as possible until the ions are in close proximity to the cathode of the detector. The stainless rings are aligned by three

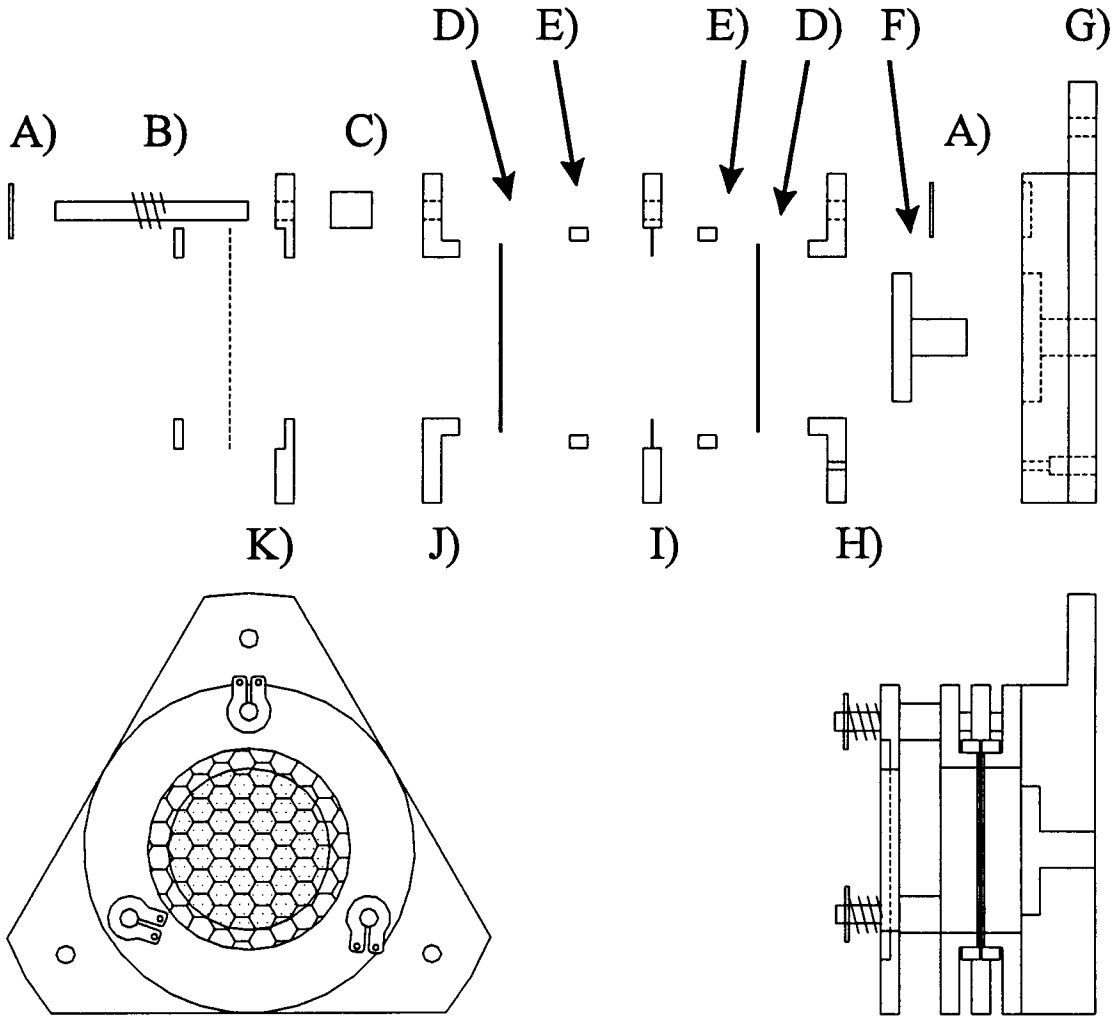

Figure 2-13 Exploded and assembled views of the micro-channel plate detector. A) Snap ring fastener. B) Al_2O_3 rod and tension spring. C) Al_2O_3 spacer. D) Microchannel plate. E) Delrin spacer. F) Stainless anode. G) White delrin backing plate. H) Stainless base ring. I) Stainless shim ring between microchannel plates. I) Stainless top ring. K) Stainless grounding ring and wire grid.

Al_2O_3 rods and compressed with springs held with snap rings. The detector is designed to be as rigid as possible so that the plates are not stressed in any way.

2.3.3.2 Circuit Design

Figure 2-14 shows the electrical circuit for the microchannel plate detector. A Stanford Research current limited, high voltage power supply biases the first plate to a voltage of approximately -2000 V and a 2 MΩ resistor is used to drop the potential to -1000 V between the two plates. The output side of the second plate is held at -100 V so that the ejected electrons can be efficiently collected by the anode which is held 50 Ω above ground. The 50 Ω resistor to ground on the anode serves to couple the current pulse into the coax cable without causing ringing.

With rise times on the order of nanoseconds, any impedance mismatch will cause significant oscillation of the pulse in time. Correct choice of the output coupling resistor on the anode is necessary since wound type resistors have a significant inductance and will make the ringing even worse. Instead, a carbon type resistor works best and some trial and error is needed to find the proper resistor that minimizes the impedance mismatch.

2.3.3.3 Microchannel Plate Design

Microchannel plate amplification devices consist of a lead glass wafer approximately half a millimeter thick that has half a million channels or holes per square centimeter.[28] It is interesting how the microchannel plates are fabricated.[16] First a lead glass tube with a outside diameter of 40 mm has a etchable glass rod inserted in it. A stack of these tubes is then drawn in the same way that fiber optic cables are pulled. This bundle is then cut into lengths, stacked and pulled several more times until a final inside tube diameter of 9.4 μm and a spacing of 11.5 μm is obtained. At this point the bundle is

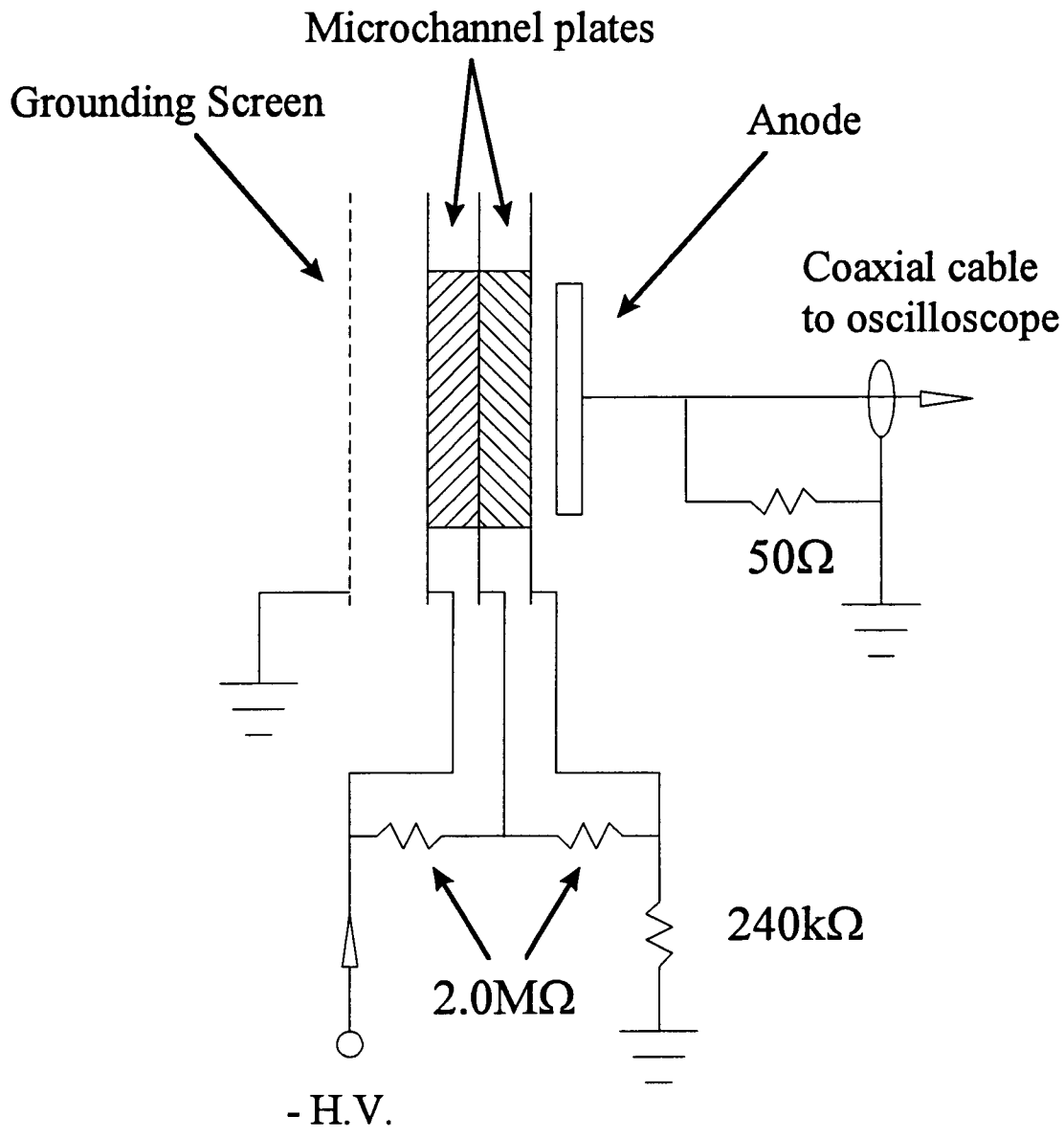

Figure 2-14 Circuit diagram for the microchannel plate detector.

sliced into wafers that are polished to the correct thickness. The etchable glass is removed and then the plates are reduced in a hydrogen atmosphere to create a low work function, high resistance semiconducting surface with high secondary electron emission

characteristics. The surface of the wafer is coated with a thin film of either nickel or nickel-chromium to provide a conducting layer so that a uniform electrical field can be applied to the channels. This conducting layer also allows charge to be restored to the semiconducting channels after a pulse. At this point the channel plates are ready for use.

The channels in the plates are designed very carefully to optimize the gain. The most important parameter for the channel gain is the length to diameter ratio (46 for Intevac plates[29]). The channels should be as small as possible to increase the geometrical open area of the plate (about 60% for most plates[29]). This ratio limits the fundamental diameter of the channels because as the holes get smaller, the plates must become thinner and at some point they will not have enough mechanical strength. Another critical factor in the design of the channels is the angle that the channels make with the normal to the surface. A bias angle between 11-12 degrees is typical. The reason for this is that as the secondary electrons are accelerated in the channel, they collide with residual gases with enough kinetic energy to create positive ions. These ions are accelerated in the opposite direction and produce secondary electrons when they hit the walls of the channels. This causes the detector to saturate and broaden the pulse out. This problem can be reduced in two ways; the vacuum pressure can be reduced and the holes can be tilted at a small bias angle. Having the holes at a small angle limits the distance the electrons can be accelerated so that the probability of creating positive ions is reduced. Typically two plates are stacked together so that higher gain can be achieved. In this arrangement the plates are oriented in such a way that the bias angles are in opposite directions. This so called "Chevron style" is the design employed in this experiment.

2.3.3.4 Operation

Routine operation of the microchannel plates is fairly straight forward. After it is determined that the plates operate properly, e.g. no electrical shorts, there is little more to do than turn the voltage on and off. There are however a few precautions that must be taken.

It is very important that the vacuum pressure be kept below 10^{-6} torr while the high voltage is on. This is to prevent arcing between the plates due to electrical break down of the background gas. It is also important keep the plates free from vacuum pump oil. Our chamber uses two oil diffusion pumps so it is difficult to completely prevent contamination from occurring. The best prevention is to make sure that the backing pressure for the diffusion pumps never exceeds 50 millitorr. If this happens, the diffusion pump cannot pump efficiently and oil will backstream into the chamber. This should not be a problem under normal operating conditions.

The gain of the detector is dependent on the potential across the plates. A gain of 10^7 is typical if the plates are arranged in the Chevron configuration. Before the plates are shipped from Intevac they are performance tested and the results are sent with the plates. Figure 2-15 shows the gain for the individual plates as furnished by Intevac. In the Chevron configuration the gain is the product of the individual gains assuming that there is no saturation of the plates. Typically we use the detector with a bias of approximately 900 V across each plate. According to the plot this corresponds to a gain of almost 10^8.

This is probably a little too generous, a gain of 10^7 is more realistic and can be justified by taking the following factor into account. The detection efficiency depends on

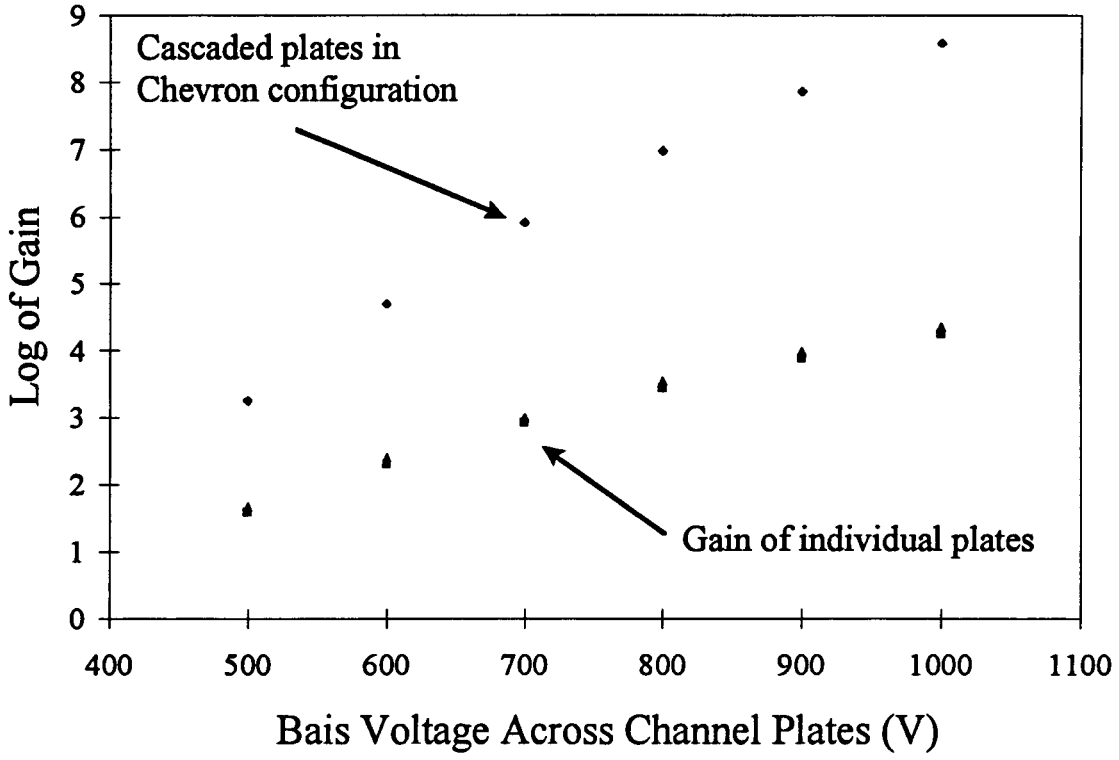

Figure 2-15 Microchannel plate gain as a function of voltage as tested by Intevac Incorporated.[29] The bottom set of points shows the gain of the individual plates while the upper set of points shows the gain possible from the chevron configuration, assuming that no saturation takes place. In both cases the voltage on the ordinate is the potential across each individual plate.

the particle as well as the kinetic energy with which it impinges the detector. In our experiment we are detecting positive ions in the 3 keV energy range which corresponds to a detection efficiency of approximately 40%.[30] Taking this into account gives the expected gain of 10^7.

2.3.3.5 **Handling Precautions**

Microchannel plates are very thin and fragile. They should be handled only when absolutely necessary and extreme care must be taken to keep from damaging the active surface. Gloves should be worn since finger oils will reduce the electrical contact with the electrodes and decrease the gain as well as increase the chance for electrical shorts. Once the package is opened, the plates should be stored under **vacuum only**. Desiccant alone **will not** keep the plates dry enough and over a period of several weeks they will absorb water, swell and break. Cleaning the plates is possible in theory with reagent grade solvents, but this has never been done in this lab to date.

2.3.4 Vacuum System Operating Procedures

2.3.4.1 **Pump Down Procedures**

Pump-down of the vacuum system begins with closing the gate valve on the Varian pump, the butterfly valve on the Edwards pump and all roughing valves in Figure 2-16 before starting the roughing pump. The pressure in the foreline should reach approximately $5x10^{-3}$ torr (the roughing pump is capable of reaching pressures of 10^{-4} torr) before opening the backing valves to the diffusion pumps. Only one of the pumps should be backed out at a time so oil and contaminants from the roughing lines don't get into the pumps when the vacuum line momentarily comes under higher pressure. Once the diffusion pumps are backed out, all the valves should be closed once more so the main chamber can be roughed out with the three-way valve on the Edwards diffusion pump.

This valve is opened slowly so as not to overload the roughing pump. After the roughing pump has stopped gurgling the pneumatic valve on the main chamber can then be opened to speedup the pump down time. Check that the cooling water is flowing (0.25 gpm at 60 ^{0}F to 80 ^{0}F inlet temperature), then the diffusion pumps can be turned on after the vacuum chamber is pumped out and the roughing pumps are switched to backing.

The diffusion pumps take approximately one hour to reach operating temperature. During this time the gate valves should not be opened since the oil trajectories in the pump are not well defined and it is possible for oil to stream back into the chamber. This can be a problem for the Edwards pump in particular since the microchannel plate detector sits directly above the pump inlet and any oil that gets on the detector can potentially cause problems such as electrical shorts and decreased sensitivity. Both pumps have oil traps that keep the small amount (0.0005 mg / cm^2 / min for the Varian pump without the trap) of residual oil from back-streaming during normal operation.

Two different kinds of traps keep oil from the diffusion pumps from back-streaming into the vacuum chamber. On the Varian pump the trap is cooled with methanol cooled to -60 °C with a recirculating chiller. The cold surface of the trap condenses the oil vapor back to liquid so that it can drip down the walls of the pump back into the reservoir. The Edwards pump is similar except that instead of using a methanol cold trap, the cooling water first goes into the trap and then comes back out to cool the walls of the pump. The chiller on the Varian pump should be turned on when the pump is turned on, but not before. If it is left on while the pump is under pressure any moisture that is in the air will condense and build up a layer of ice that will decrease its trapping efficiency. Of course, if the pump is purged with a dry gas this problem can also be

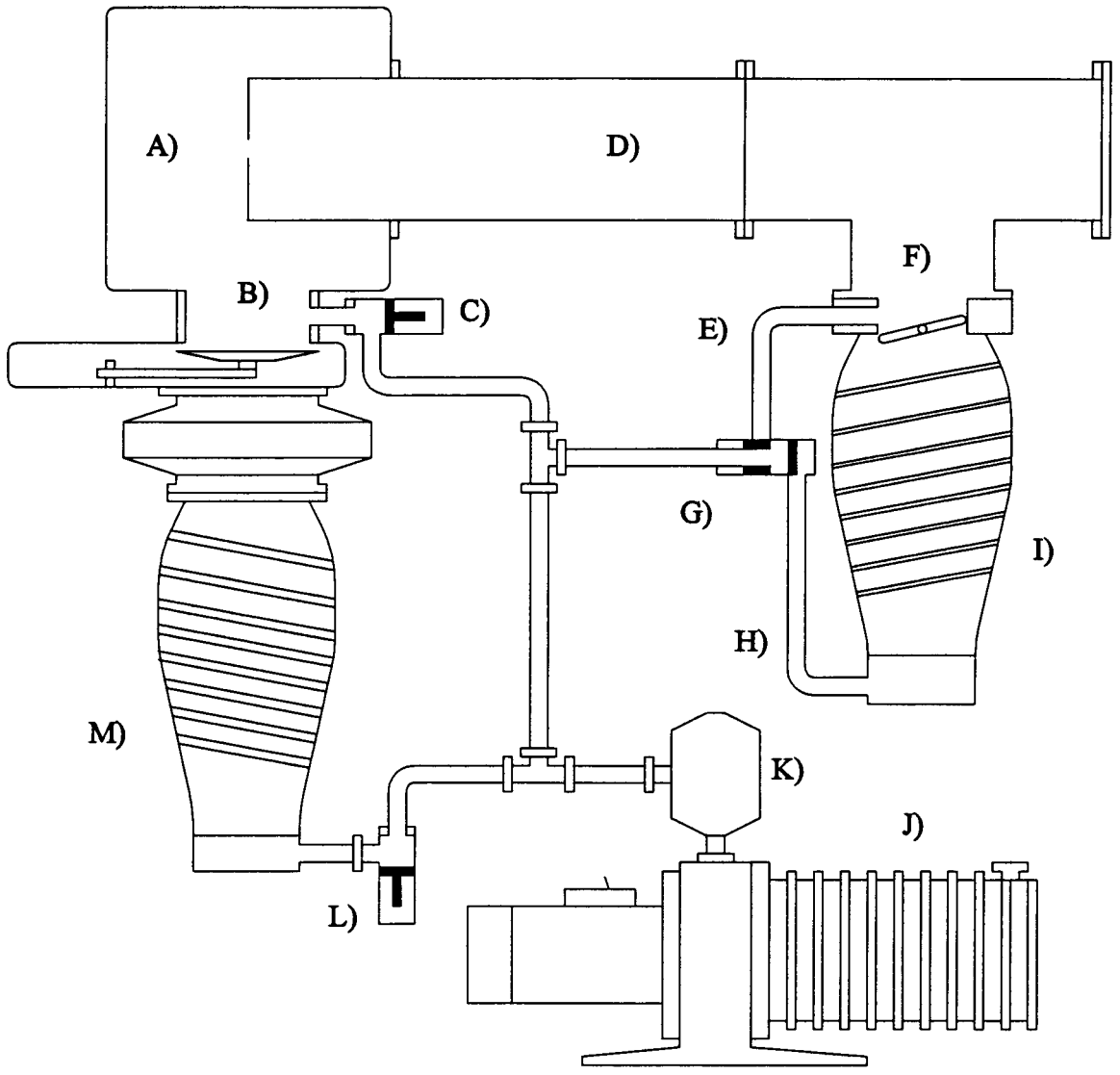

Figure 2-16 Vacuum system layout. A) High pressure region, typically 10^{-5} torr under load. B) Gate valve for the Varian diffusion pump. C) Pneumatic valve for roughing the high pressure region. D) Low pressure region, typically 10^{-6} torr under load. E) Roughing port for the low pressure region. F) Butterfly valve for the Edwards diffusion pump. G) Three-way valve for roughing the low pressure region, backing the Edwards diffusion pump, or isolating the vacuum system. H) Backing port for the Edwards diffusion pump. I) Edwards diffusion pump. J) Alcatel roughing pump. K) Molecular sieve oil trap. L) Pneumatic Backing valve for the Varian diffusion pump. M) Varian diffusion pump.

avoided. In practice, it is rare that the pump itself should need to come up to pressure so the chiller is usually left on.

When the pumps have reached operating temperature, the chamber pressure needs to be pumped down to less than 10^{-3} torr before the gate valves are opened. The reason is to keep from stalling the diffusion pump. For the same reason, the butterfly valve on the Edwards pump is opened very slowly while watching the pressures in the vacuum chamber and foreline. The valve is opened slow enough that the backing pressure never exceeds 5 x 10^{-2} torr. When the pressure on the thermocouple gauge reaches zero, the ion gauge can be turned on to monitor the pressure in the chamber. The butterfly valve can be opened fully when the pressure reaches approximately 5 x 10^{-5} torr without causing the backing pressure to exceed 5 x 10^{-2} torr. Once the pressure in the chamber reaches 10^{-5} torr the gate valve on the Varian pump can be opened for normal operation.

2.3.4.2 **Pumping Speed and Ultimate Pressures**

After the vacuum chamber has been open to the atmosphere it takes about a day before the ultimate pressure of 1 x 10^{-7} torr is reached. During this first day the outgassing creates an extra load on the diffusion pumps and therefore decreases the useful load on the vacuum. We can calculate the ultimate vacuum pressure P obtainable by dividing the pump load Q by the pumping speed S, which is given in Table 2-2 for the pumps on our vacuum system. To get an approximate value for the pump load Q (torr liters per second) from all leaks and outgassing we can use the relation[30]

$$Q = \frac{V\,\Delta P}{\Delta t}, \qquad (2.21)$$

where V is the volume of the isolated chamber (in liters), ΔP is the change in pressure (torr) that the chamber increases by when isolated from the pumps for the amount of time Δt (seconds). To measure this quantity we first pump down the vacuum system to its ultimate pressure and then close the valves to both diffusion pumps for a fixed amount of time. The pressure is measured after this time has elapsed and ΔP is computed. The volume is found from the dimensions of the vacuum system and is approximately 41.5 liters. A typical value for the gas load and the computed ultimate pressure is given in Table 2-3.

Pump	Pump Speed S (liters/sec.)
Diffusion:	
Varian[30]	2400
Edwards[31]	700
Mechanical:	
Alcatel[32]	7.5
Stokes	26

Table 2-2 Pumping speeds for the vacuum pumps employed in this experiment.

Δt (s)	ΔP (torr)	Q (l torr / s)	P (torr) calculated	P (torr) measured
330	0.042	$5.3 \cdot 10^{-3}$	$7 \cdot 10^{-4}$	$8 \cdot 10^{-3}$

Table 2-3 Characterization of the vacuum chamber pressure performance. Q is the pumping speed of the pump and P is the ultimate pressure obtainable for a given load on the system.

2.4 Timing of Experiment

The timing between the lasers and pulsed valve is critical for the ion signal intensity. Every pulse of the experiment is initiated with a TTL trigger (t_1 in Figure 2-17 part a)) from the chopper wheel for the ring laser beam. This pulse is sent to the three channel pulse delay unit where the delays are set and the TTL pulses are sent to the Continuum, Quanta Ray and pulse valve as shown in Figure 2-17 c). It takes approximately 0.5 ms for the valve to open fully after the voltage is applied, so this pulse is sent out before the TTL pulses to the laser lamps. The build-up times for the Continuum/Spectra-Physics YAG's are 332/187 μs respectively and these delays are fixed, that is they must have these values in order for the lasers to fire at the appropriate time relative to the chopped seeder beam. The pulse out to the valve is the only delay that should be adjusted to optimize the ion signal. All the other delays must be close to the values shown in the figure. In order to have a precise delay (about 60 ns) between the Continuum and the Quanta Ray, the Q-switch for the Quanta Ray is trigged off the Q-switch sync out from the Continuum. This sync out has a pot that allows the delay to be varied but it is more convenient to use a separate delay generator for this purpose.

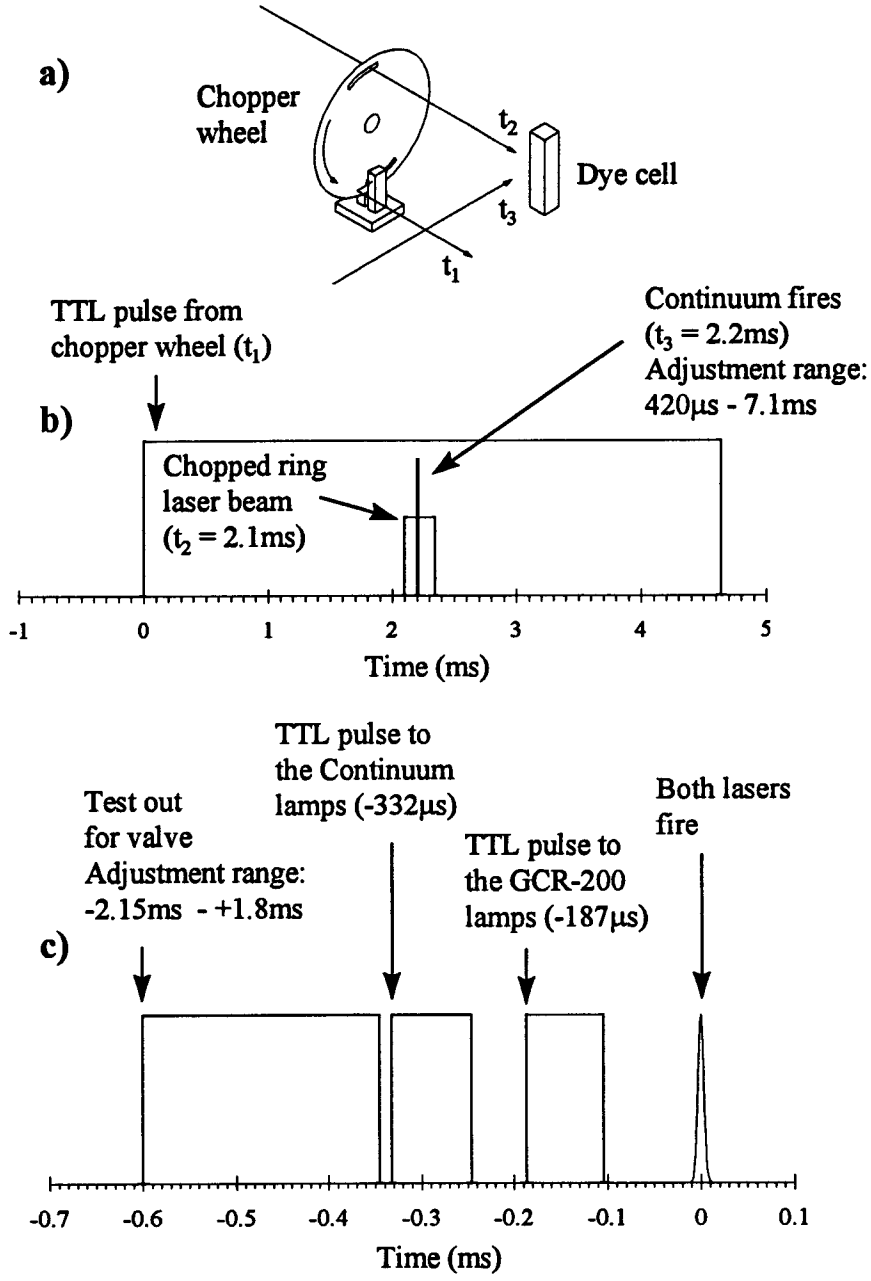

Figure 2-17 Timing diagram for the experiment. Part a) shows the chopper wheel for the ring laser beam, the Continuum laser and the TTL output for the chopper wheel. Part b) is a diagram that shows the relationship between the pulses in part a). Part c) is an expanded view of the b) around 2.2 ms. This shows how the TTL pulses to the laser lamps and valve are delayed relative to the laser output pulse. Note that the delays that are adjustable have the range specified although they must be set to the values shown in order for the experiment to work properly.

3. PRELIMINARY EXPERIMENTAL RESULTS ON BENZENE

For testing and calibration of the IDSRS experiment it is logical to begin with a molecule that is readily ionized with resonantly enhanced multiphoton ionization (REMPI). A great deal of work has been published on the 1 + 1 REMPI spectra of benzene[33,34,35,36,37,38,39] and it is well known for its ease of ionization. Benzene also fits in with the long term goal of studying molecular clusters. Since benzene readily clusters with itself as well as almost any other molecule and the clusters typically have high symmetry, it provides a ideal system for rotationally resolved Raman spectroscopy of molecular clusters.

The initial studies presented in this chapter are important because the experience gained gives a sense of detection capability and the sensitivity of signal levels to experimental variables. Preliminary work focused on the characterization of the time of flight apparatus and photoionization processes, both of which are important for future mass selective spectroscopic experiments. The experiment then shifted to understanding the mass selective photo-ionization spectra of the benzene monomer from the ground state. In order to be certain of the UV frequencies used in the double resonance experiments, several spectra of the hot band transitions were taken. Using the data from these experiments, all the lasers were combined to take IDSRS spectra of the benzene. As an example of the mass selective capabilities, example ionization spectra of benzene clusters are presented at the end of the chapter.

3.1 Time of Flight Spectra of Benzene Clusters and Fragments

A significant amount clustering of benzene occurs even at mild driving pressures of 0 - 1 atmospheres. At pressures exceeding one atmosphere the aggregation of larger clusters occurs and the overall signal of the monomer and small clusters (2 - 20) decreases. The ionization frequency for all benzene clusters is nearly the same so with driving conditions that produce small clusters we can sit at a fixed frequency and monitor the mass distribution of clusters. Figure 3-1 a) shows a time of flight spectrum for benzene with the ionization laser tuned approximately 40 cm^{-1} to the red of the 6_0^1 transition for the monomer shown in Figure 3-2. To obtain this spectrum, the signal from the detector was sent into the Tektronics 2445 digital oscilloscope and averaged for 256 shots. The trace was then sent to the computer for storage as intensity vs. time. To convert the time of flight to mass units we take the square root of the time and calibrate to the monomer peak using (2.20).

It is interesting to consider the fragments that are produced. Fragmentation occurs from the electronic ground state of the monomer ion when it absorbs one or more photons before it leaves the focal region, as shown by Schlag et al.[40] At high UV intensities this can lead to significant fragmentation. There are two kinds of dissociation processes that occur when this happens. The first is known as ladder switching and is very fast with rate constants on the order of 10^9 s^{-1}, approximately the duration of the laser pulse. It is known as ladder switching because the neutral molecule first climbs up its energy ladder, quickly ionizes, and then climbs the energy ladder of the ion until it fragments. The second method is a slow dissociation of metastable ions after they have left the ionization

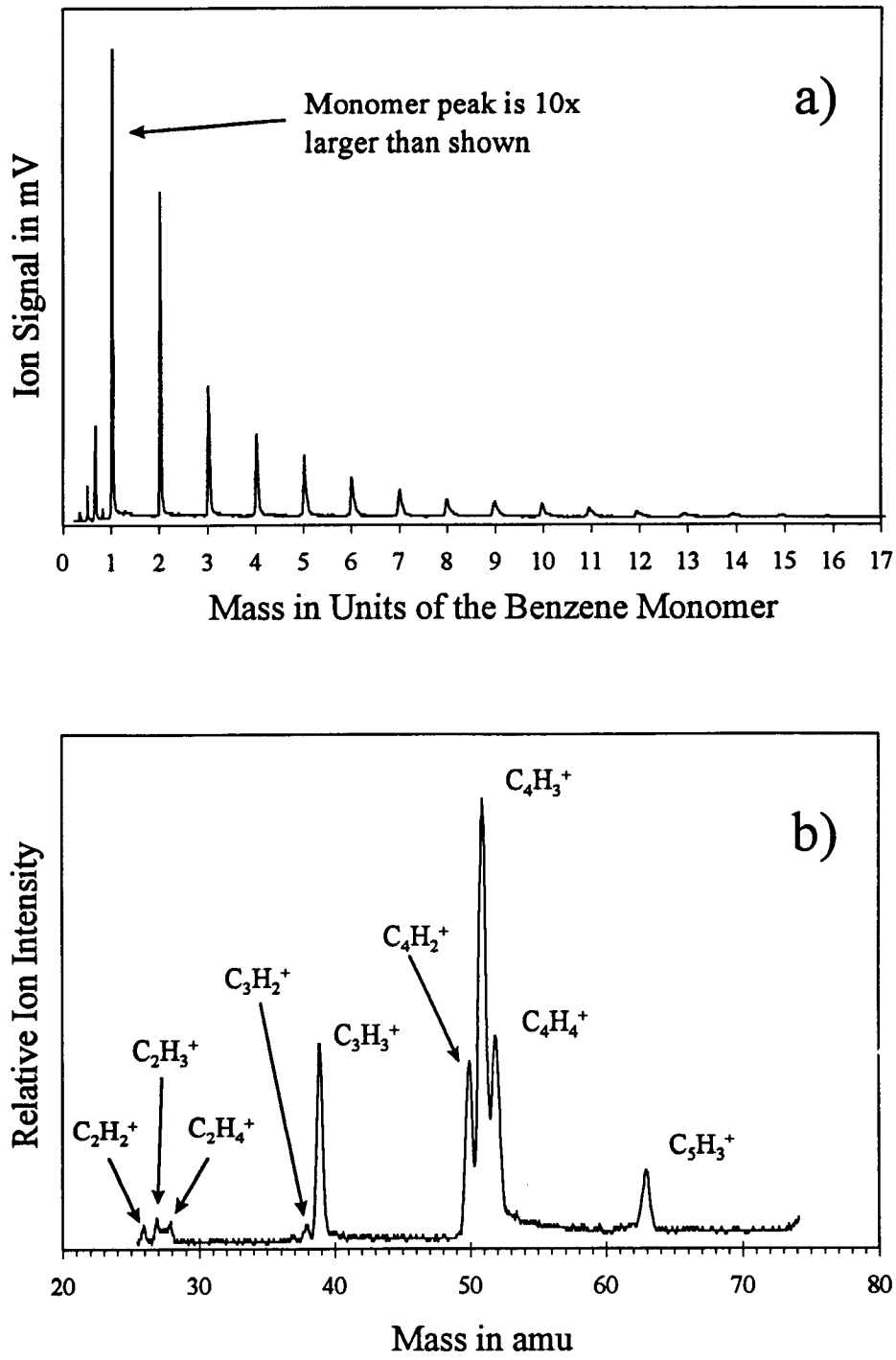

Figure 3-1 a) Mass spectrum of heterogeneous benzene clusters. File: 081894.xls b) Expanded region of the benzene fragments. File: 082094.xls

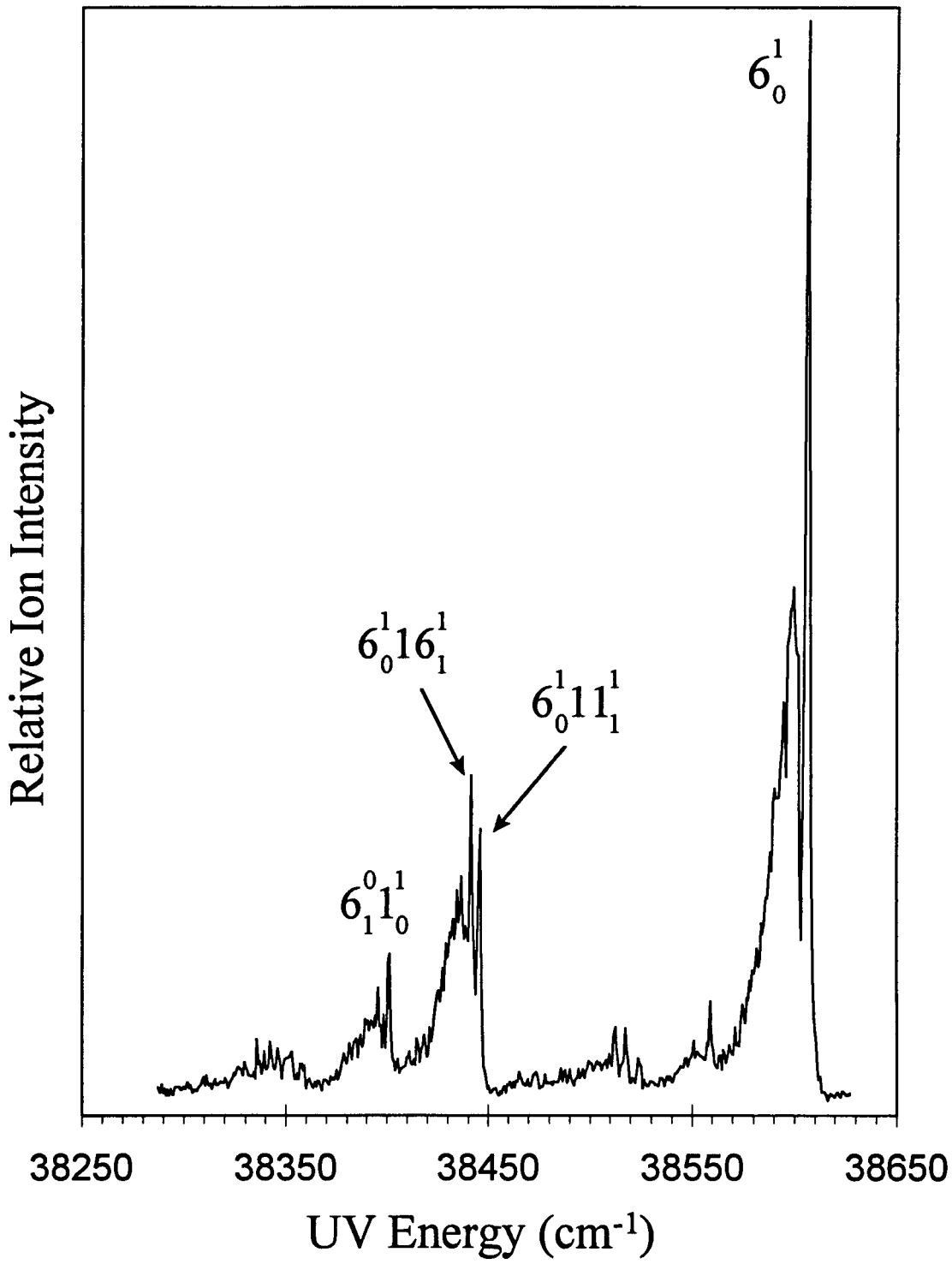

Figure 3-2 Ionization spectrum of the benzene monomer from the electronic ground state.

region. The rate constants in this case are on the order of 10^6 s^{-1}. This process was studied in detail by Schlag et al[34,41,42] and Neusser et al[43] with a reflectron time of flight mass spectrometer. The advantage of the reflectron is that it is capable of measuring the *energy* of the charged particle instead of the velocity. This means that even if the ion falls apart after it reaches its final velocity in the acceleration region, it can still be separated from other masses.

The mass spectrum in Figure 3-1 b) shows the benzene fragments in an expanded view of part a) when the UV is tuned to the 6_0^1 transition of the monomer. The fact that the mass peaks are well resolved indicates that the fragments are instantaneously produced at the focus. If the molecules were to fragment later in the acceleration region the mass peaks would have an asymmetric tail to longer flight times. On the other hand, if the ions fall apart after they are accelerated, there would be no change in the TOF spectrum since they would have already achieved their final velocity. With the assumption that all the mass peaks have one unit of charge, we can determine the composition of each mass peak by comparison of the time of flight to the monomer as shown in Figure 3-1 b).

3.2 Ionization Detected Spectra

Normal UV fluorescence or absorption cannot discriminate spectral features that come from various constituents in the sample region. This is not desirable for studies of clusters—even, or perhaps especially, at high resolution. If high enough resolution is used the rotational structure can be resolved, but when there are several different sized clusters present it will be difficult to assign the spectrum since the many peaks could come from

any of the different components of the sample. The mass spectrometer provides a convenient way to deconvolve complex UV spectra of clusters since a specific mass can be monitored as a function of frequency without interference from other masses. In this section mass selected UV ionization spectra of benzene are presented to demonstrate the capabilities of our apparatus.

3.2.1 Benzene Monomer

3.2.1.1 **Ground State Spectra**

For dipole transitions, the possible electronic states that can be accessed from the A_{1g} ground vibrational/electronic state are of symmetry:

$$A_{1g} \otimes \begin{Bmatrix} A_{2u} \\ E_{1u} \end{Bmatrix} = \begin{Bmatrix} A_{2u} \\ E_{1u} \end{Bmatrix} \qquad (3.1)$$

The 0_0^0 transition at 38086.1 cm^{-1} is electric dipole forbidden for the monomer since the vibrationless electronic state is of B_{2u} symmetry. Therefore, transitions that originate in the electronic and vibrational ground state must end up in a vibrational state that has a symmetry of e_{2g} since

$$B_{2u} \otimes e_{2g} = E_{1u} \qquad (3.2)$$

is the only product that gives a dipole symmetry. There are four fundamental vibrational states that have e_{2g} symmetry, but by far the 6_0^1 transition is the strongest transition to the B_{2u} state.

The strong 6_0^1 transition state shown in Figure 3-2 provides a convenient measure for the ion signal levels. Typical signal levels are around 500 mV to 1 V for UV intensities of a few hundred microjoules. As can be seen from the rotational bands in the figure the benzene sample is quite warm even though this spectrum was taken in a jet. The cooling was minimal because the spectrum was taken in a neat jet with a driving pressure of the vapor at room temperature (100 torr at 26.1 °C)[44]. Even with a driving gas and low rotational temperatures there is a significant rotational band[33] that can be seen because many low energy rotational states are populated due to the small rotational constants of benzene. In fact, with a rotational temperature of 8 K, Riedle et al[33] measured a total of 353 lines for the 6_0^1 transition.

3.2.1.2 **Hot Band Spectra**

In order to perform any ionization gain double resonance experiment, both frequency for the Raman and UV transitions must be known very precisely, since no signal can be seen unless both are on resonance. Therefore, several hot band spectra were taken from vibrational modes that were of interest. UV transitions from Raman pumped states with a_{1g} symmetry go to the same states as the ground state ionization spectra. But, UV transitions from e_{2g} states can go directly to the vibrationless B_{2u} state. Unfortunately, the four Raman transitions of this symmetry are very weak[45] and have Raman crossections approximately ten times smaller than those for the totally symmetric a_{1g} modes.[46]

Initially, the mode of primary interest was ν_8 (e_{2g}) at 1609 cm^{-1} since it had been studied by Esherick and Owyoung at high resolution.[4-5] This state is in Fermi resonance

with a combination band $\nu_1 + \nu_6$ of the same symmetry at 1591 cm^{-1}. At a vibrational temperature of 278 K the population at this energy is about 10^{-4} relative to the ground state. Even so, there is a strong ion signal for both the 8_1^0 and $1_1^0 6_1^0$ transitions with good signal to noise, as shown in Figure 3-3. Due to the fact that the Raman transitions to these states are so weak it makes sense to try a set of transitions that are strong both in the Raman step and in the resonant UV ionization step.

The strongest Raman transitions are to the two a_{1g} modes ν_1 (993 cm^{-1}) and ν_2 (3073 cm^{-1}). For the ν_1 state we can go to the 6^1 state with the UV transition. This transition is strong as shown by UV fluorescence studies from the 6^1 state done by Parmenter.[47] A hot band ionization spectrum in this region is shown in Figure 3-4. The $6_0^1 1_1^0$ transition is approximately ten times smaller than the 6_1^0 transition and is mostly due to the difference in population between the two states. In fact, if we assume that both transitions have the same transition line strength, we can calculate the vibrational temperature for the sample as $T \approx 240$ K. This spectrum also shows that it would be possible to perform a IDSRS experiment on the ν_6 band as well, but in this case we would be fighting a strong background ionization signal due to thermal population in the vibrational state ($n/n_0 = 0.025$). IDSRS from the ν_2 state is complicated by the fact that the UV photon for the $6_0^1 2_1^0$ transition is not energetic enough to ionize the molecule from the 6^1 state. Another mode could be chosen in the B_{2u} state such as ν_7 (3077 cm^{-1} above the 0^0 state) but the ionization efficiency would not be as great as that for ν_6 and no ionization data was taken for this region. A better solution would be to add another UV

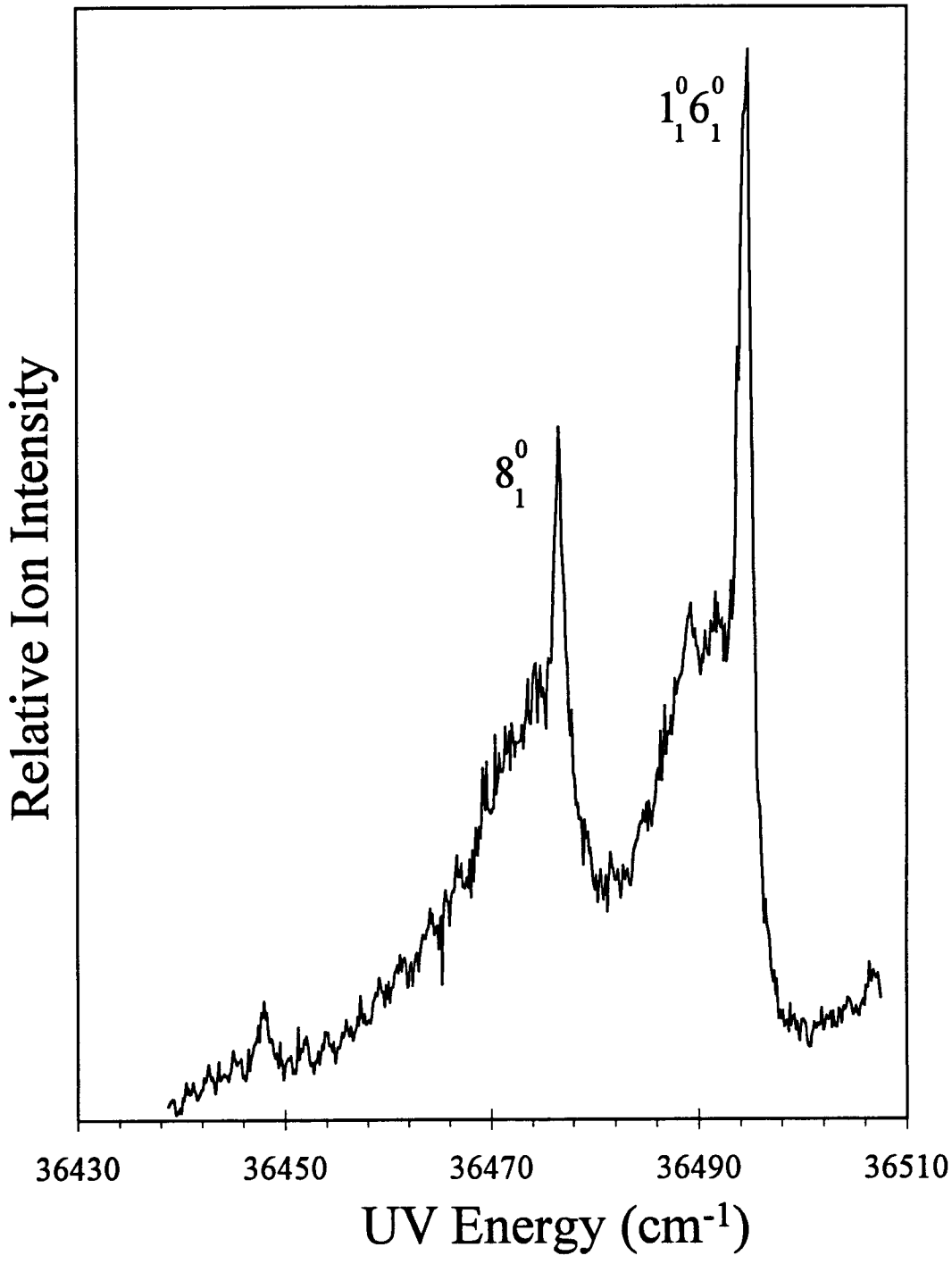

Figure 3-3 Hot band ionization spectrum of the benzene monomer. This scan was used for calibration of the PDL dye laser in the IDSRS experiment on the ν_8 mode.

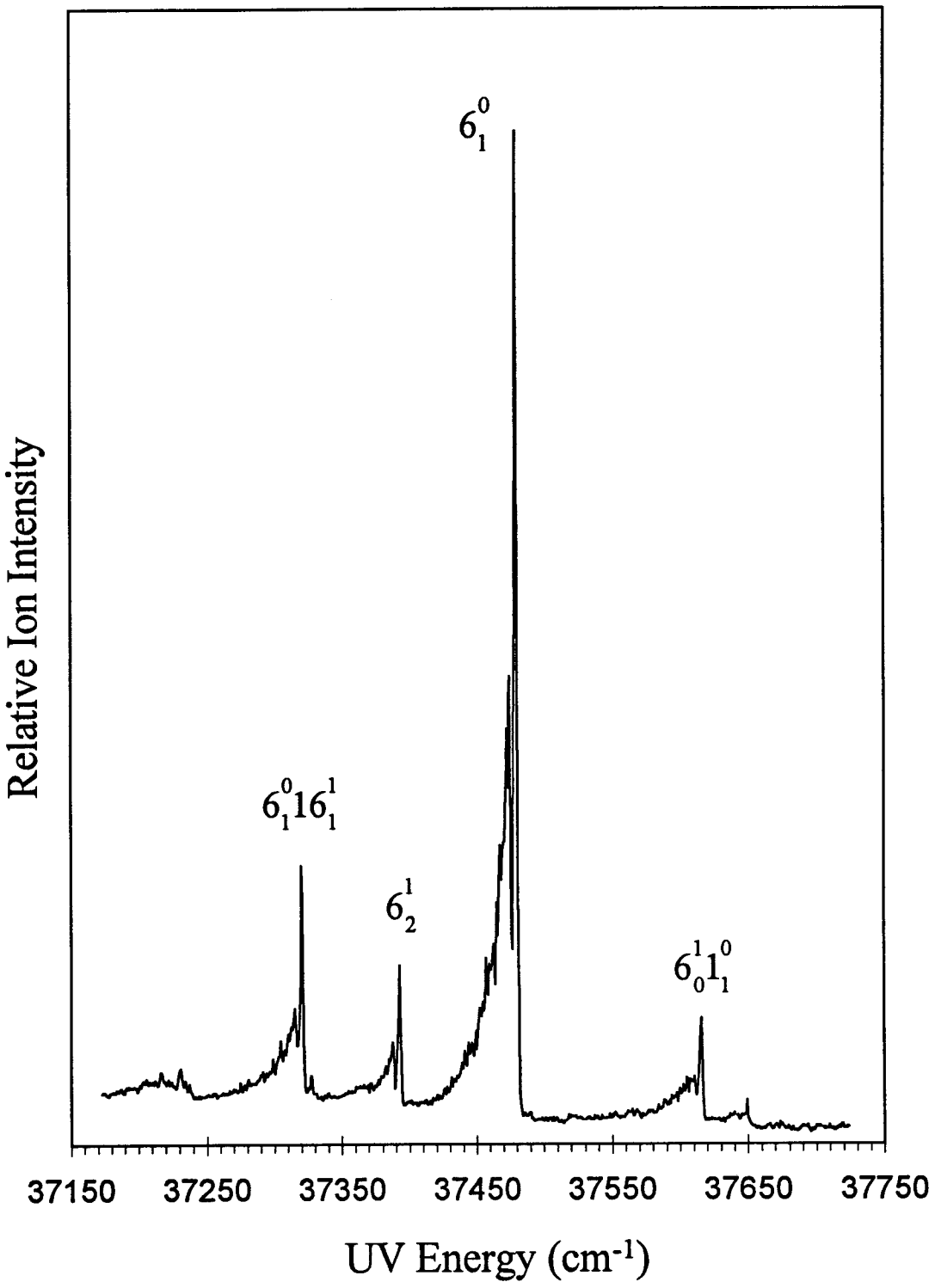

Figure 3-4 Hot band ionization spectrum of the benzene monomer from ν_1 and ν_6 in the electronic ground state.

laser that was tuned to match the energy difference between the ionization threshold and the 6^1 state.

3.2.1.3 IDSRS Spectra of the Benzene Monomer

As a demonstration of the IDSRS experiment, a spectrum of the totally symmetric ν_1 vibrational mode at 992 cm^{-1} is shown in Figure 3-5. This mode is a logical choice for the IDSRS experiment since both the Raman and the UV, $6_0^1 1_1^0$, transition probabilities are very large (see section 3.2.1.2 above). To take the spectrum shown in Figure 3-5 the UV laser was tuned to the $6_0^1 1_1^0$ hot band peak shown in Figure 3-4 and then the Stokes laser was scanned across the ν_1 transition while the monomer ion mass was monitored. The energy level diagram in Figure 3-6 shows all the levels involved as well as the symmetries and energies.

No resolvable rotational structure can be seen in the Q-branch spectrum of Figure 3-5 and the width of the peak is only about 0.01 cm^{-1} wide. The reason that no structure can be seen is because this is the symmetric C-C stretch mode of benzene and the rotational constants do not change significantly going from the lower to the upper state. For a Q-branch of this type all that is seen in the transition is the difference between the upper and lower rotational constants, therefore this transition has no resolvable structure.

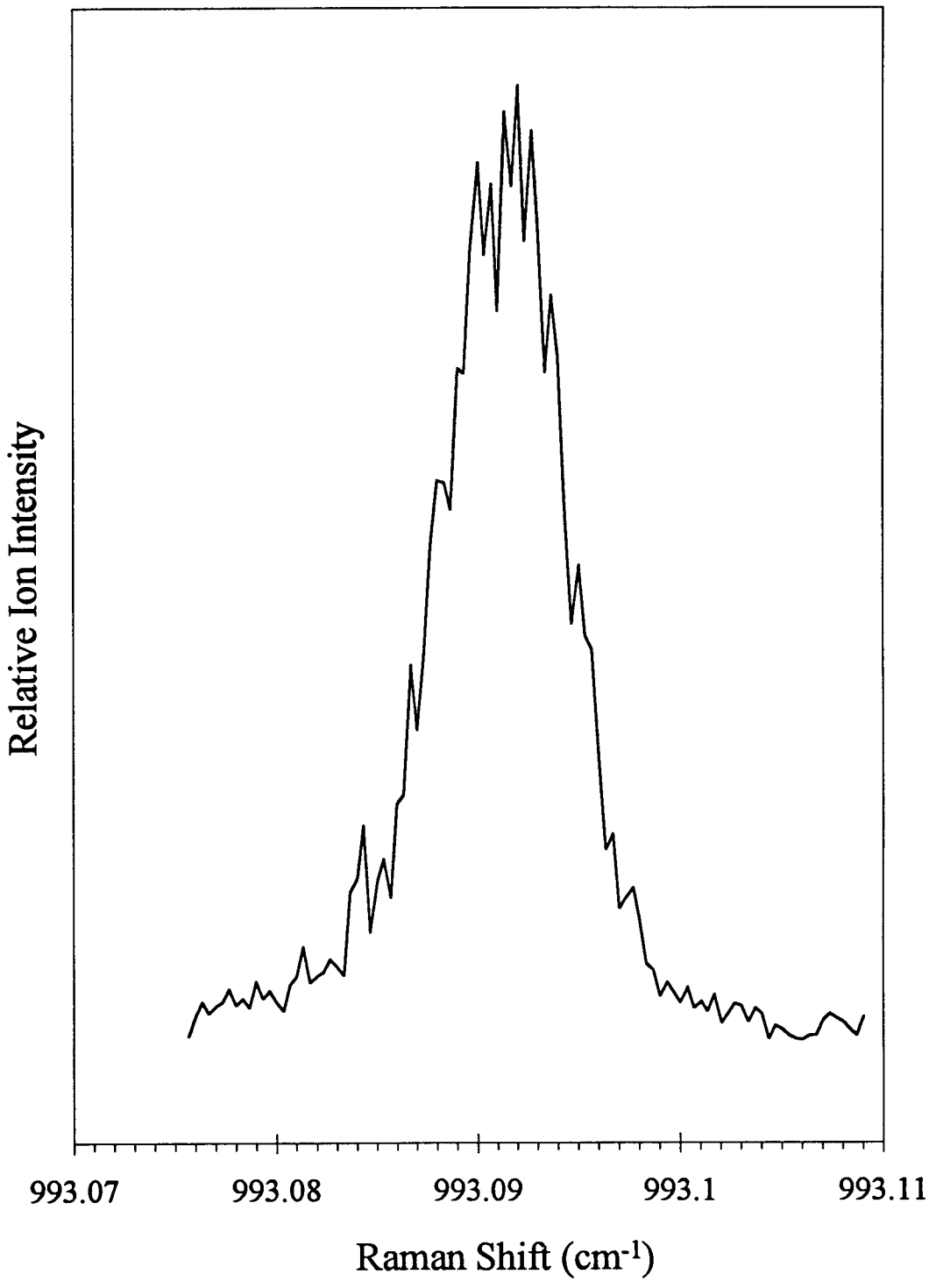

Figure 3-5 IDSRS spectrum of the benzene ν_1 Q-branch.

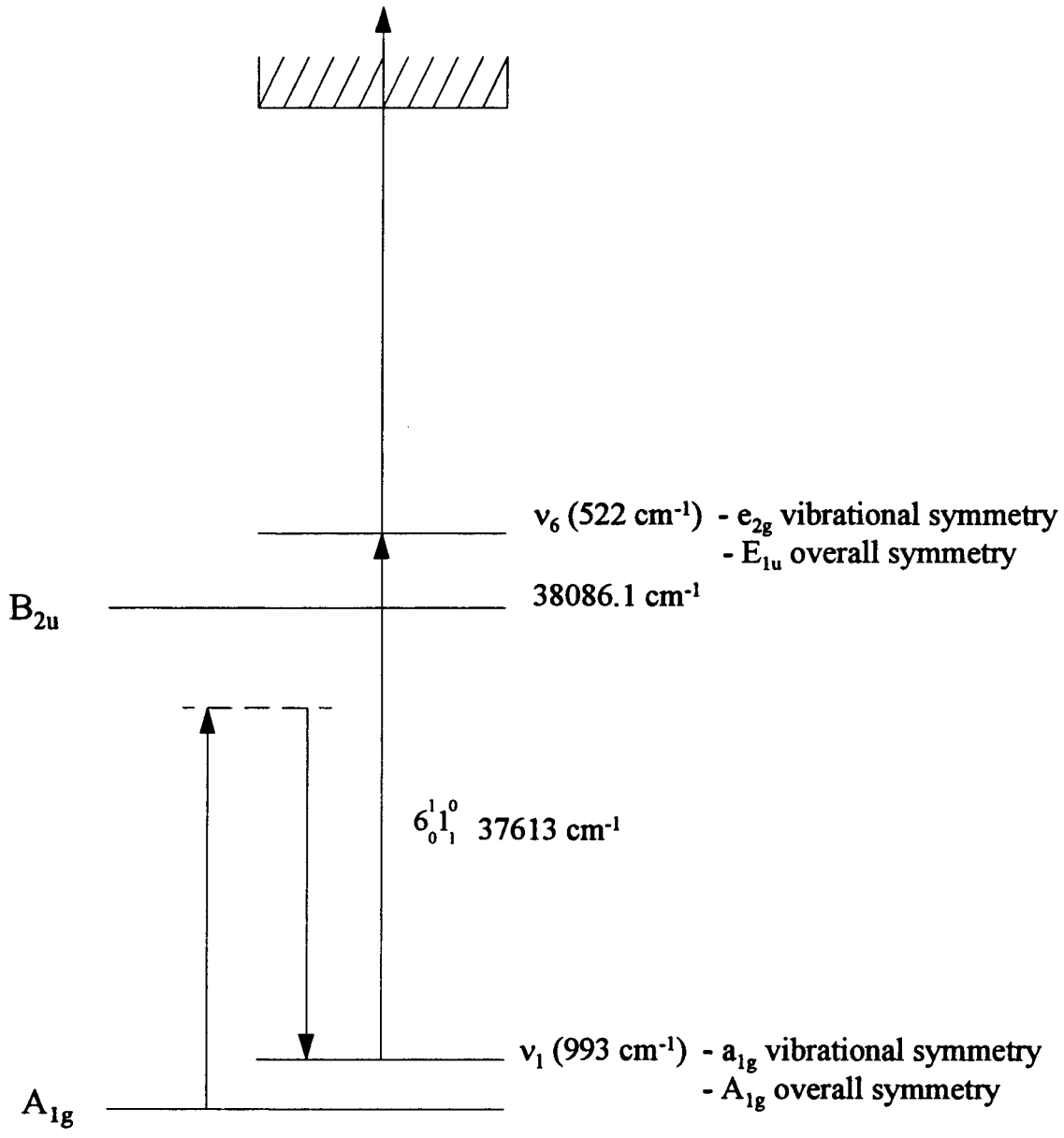

Figure 3-6 Energy level diagram for the IDSRS experiment on the ν_1 mode of benzene. Note that the UV transition is a perpendicular transition of E_{1u} symmetry.

3.2.2 $(C_6H_6)_2$ and C_6H_6·Ar in the 6_0^1 Region

3.2.2.1 **Benzene Dimer**

Until recently, there have been no rotationally resolved spectra of the benzene dimer. A controversy over the structure had been based on the interpretation of the vibrational analysis. Microwave spectra taken recently by Arunan and Gutowsky[48] has proved that the ground state geometry is a T-shape. Still, no rotationally resolved Raman spectra of the dimer exists, although Felker and coworkers have taken medium resolution IDSRS vibrational spectra[8,11,49] of the dimer. In all their experiments they tuned the UV laser to the ground state ionization peak and scanned the Raman lasers over the Raman transition to look for a loss in the ion signal. In an effort to reproduce this work we took ionization spectra of the dimer in this 6_0^1 Region as shown in Figure 3-7.

One of the most striking features of this spectrum is the fact that there is almost no structure at all due to dissociation of clusters[50] made of more than two molecules. Clustering tends to lower the ionization potential so that the ionization threshold is exceeded by several hundred wavenumbers. The depth of the potential well for van der Waals complexes is only on the order of 200-600 cm^{-1} so high lying vibrational states can be excited by the excess energy. When these larger clusters rapidly dissociate before they leave the acceleration region, the fragments will show up at a lower mass channel. This means that the frequency spectrum of the particular mass is a convolution of several unknown masses—a problem very similar to that for UV fluorescence or absorption.

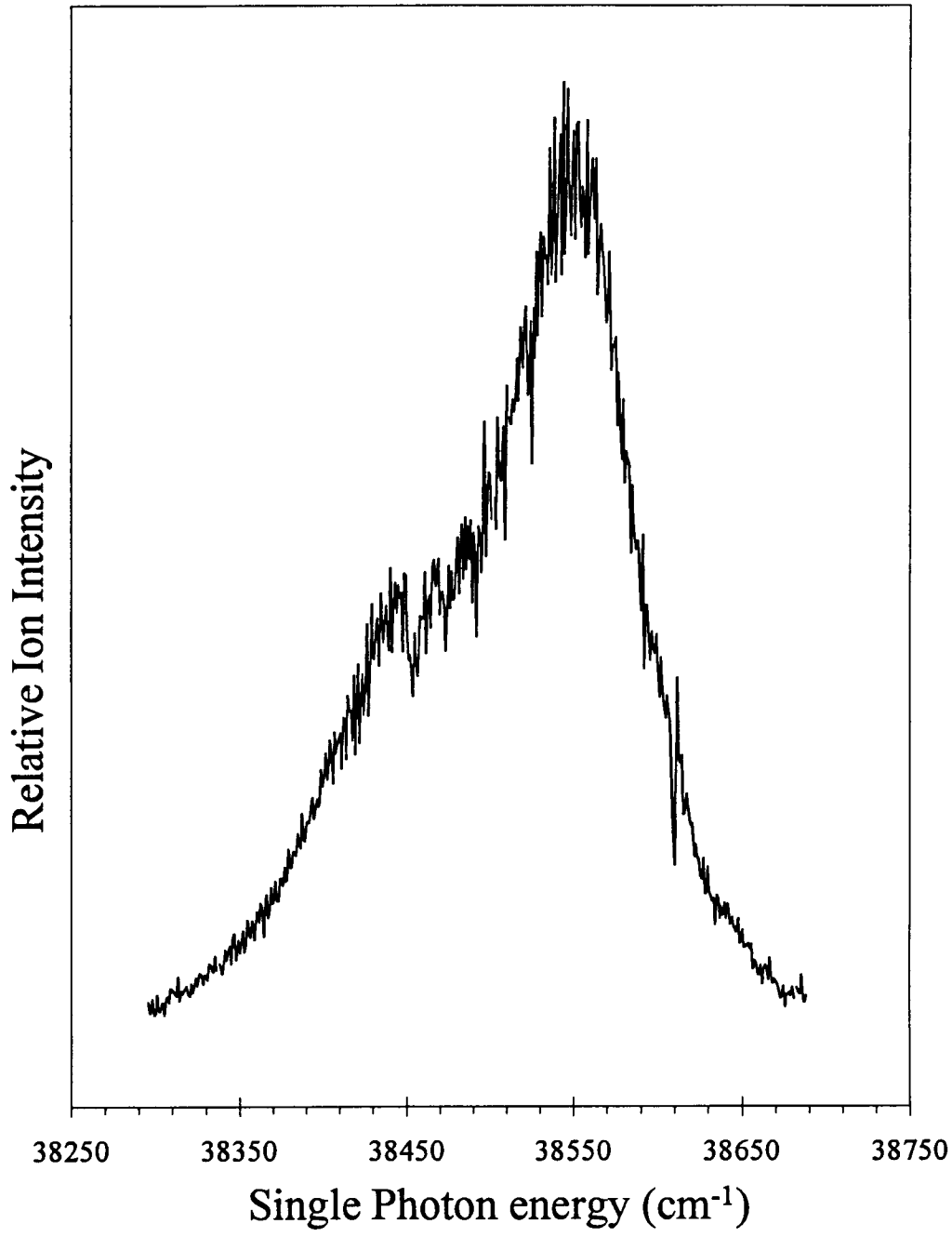

Figure 3-7 One color ionization spectrum of the benzene dimer in the 6_0^1 region.

This broad spectral feature for the dimer makes it difficult to perform an ionization-loss double resonance experiment with our apparatus. The background ionization signal completely overwhelms any depletion that would be induced by Raman pumping–even with a very strong transition. One solution to this problem would be to use a two color ionization process. This technique uses one laser that is tuned to resonance with the electronic state and a second laser to just reach the ionization potential from the electronic state. Smalley et al.[50] has used this method to show that the broad peak in Figure 3-7 is a result of the dissociation of primarily the trimer and tetramer. This is a complicated solution since it adds the complexity of another laser which must be frequency doubled and timed to the experiment. The UV beam must be brought to a common focus with the other lasers, so now there are *four* lasers that need alignment for the IDSRS experiment. The tuning of the frequency is not so critical since this laser is set at particular wavelength and needs only to exceed the threshold by some small, arbitrary amount. Complications aside, an additional laser would add more possibilities for future experiments.

3.2.2.2 C_6H_6·Ar

In the case of the benzene-argon cluster, the peaks (Figure 3-8) are relatively sharp in comparison to the $(C_6H_6)_2$ dimer spectrum (Figure 3-7). Still, this spectrum shows contamination from the dissociation of larger clusters. The two peaks marked with asterisks have been shown by Schlag and coworkers[51] to be the result of mainly C_6H_6·Ar_2 clusters.

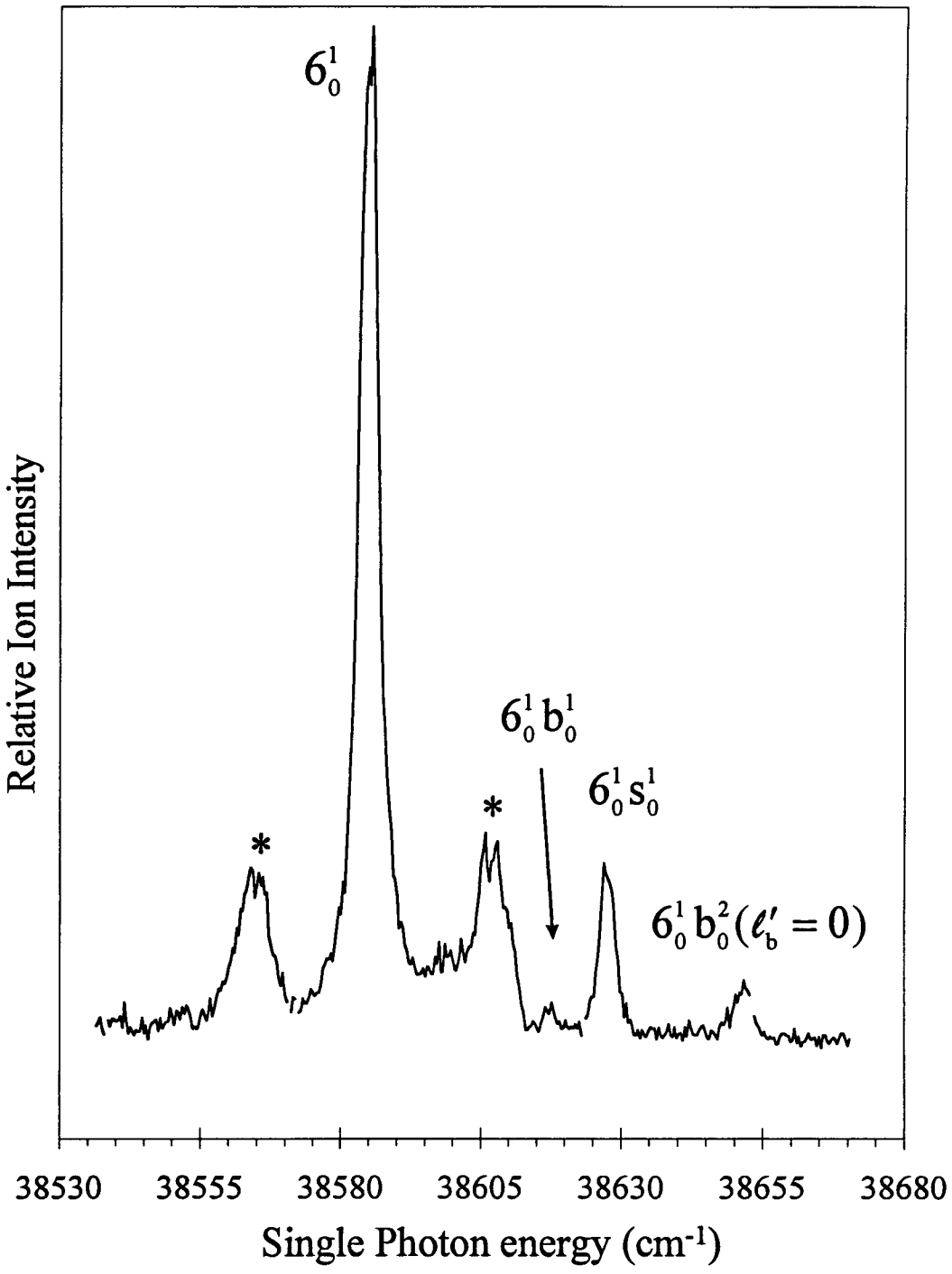

Figure 3-8 One color ionization spectrum of the C_6H_6·Ar cluster in the 6_0^1 region.

This is a nice spectrum since the van der Waals modes are cleanly resolved. The peak labeled 6_0^1 is the analog to the monomer mode with the same label. The benzene-argon cluster has C_{6v} symmetry[52,54] so the argon atom sits in the middle of the ring 3.582 Å above the plane of atoms.[53] All van der Waals modes[54] lie to higher energy and the lowest energy mode is the weak argon bend $6_0^1 b_0^1$. 8 cm^{-1} higher in energy is the argon-benzene stretch $6_0^1 s_0^1$. With two quanta of the bend we have the very interesting possibility of a degenerate mode that has pseudo-angular momentum about the cluster symmetry axis. Unfortunately, it is not possible see this mode due to selection rules so there is only the overtone $6_0^1 b_0^2 \left(\ell_b' = 0\right)$ with no internal angular momentum.

4. HIGH RESOLUTION IONIZATION-DETECTED RAMAN SPECTROSCOPY OF N_2 AND C_6H_6

4.1 Introduction

This chapter is a modified version of a journal article published in the Journal of Chemical Physics, Vol. 105, 4885-4888 (1996). As described in the introduction, Raman-REMPI spectroscopy is a double resonance method which combines the high resolution capability of stimulated Raman spectroscopy with the high detection sensitivity of resonantly-enhanced multiphoton ionization spectroscopy. The feasibility of the technique was first demonstrated in 1983 by Esherick and Owyoung,[3] who showed a 1000-fold increase in detectivity for the Q-branch spectrum of NO compared to previous stimulated Raman methods. In a later classic study,[4,5] they obtained high resolution spectra of C_6H_6 cooled in a jet expansion and were able to perform a complete analysis of the ν_8 and $\nu_1 + \nu_6$ Fermi dyad of this molecule. In both experiments, a simple electrode detector was used to measure the ion/electron burst produced by pulsed lasers. About the same time, Bronner et al.[6] improved the method with the use of a more sensitive single channel ion detector and time-of-flight mass analysis to obtain low resolution spectra of the ν_1 mode in benzene. More recently, Felker and coworkers have used channel-plate detectors and have pioneered in the application of the technique for medium resolution Raman studies of a number of aromatic clusters formed in free jets.[6-8,55] We report here results obtained with a similar apparatus but at much higher resolution (21 MHz) and using a much less efficient 2 + 2 REMPI ionization step for nitrogen molecules.

4.2 Experimental

The experimental apparatus used for this section was described in detail in Chapter 2, so only a brief overview will be given here of the relevant details. The stimulated Raman excitation source consists of a single mode ring dye laser (Coherent 699-29) pumped by an argon ion laser (Coherent I-90-6). The cw output of the ring laser is pulse-amplified in three stages by a seeded, single-mode, frequency-doubled Nd:YAG laser (Continuum). For highest resolution work, this Nd:YAG source is used in a long pulse mode, which yields 45±2 ns pulses (FWHM) of 150-200 mJ at 532 nm. Up to 30 mJ is used as the pump beam for the stimulated Raman experiment and the rest is used in the amplifier chain to give the tunable Stokes pulses of 1-2 mJ energy and 35±2 ns duration. Assuming Gaussian pulses, the Fourier transform limit of the 532 nm beam is 10±1 MHz, to which must be added 6±1 MHz from the dithering of the Nd:YAG cavity length done as part of the seeder locking procedure.[19] The transform limit of the Stokes beam is 13±1 MHz so, from the convolution of the two beams, the theoretical resolution limit of our system would be 21±3 MHz or 0.0007 cm^{-1}. The Nd:YAG laser also can be operated in a higher power, short pulse mode (12 ns) for which an analogous calculation gives a resolution limit of 65±10 MHz. In the present work, the latter mode was used for the N_2 measurements whereas the long pulse mode was used for benzene. In both cases, the observed Raman widths are close to these predicted limits.

For the UV ionization beam, a tunable dye laser (Quanta-Ray PDL-1) is pumped by the harmonics of a Nd:YAG laser and the output is frequency-doubled by an Inrad Autotracker II. This generates a UV-pulse with energy up to 2 mJ, a linewidth of 0.5

cm^{-1}, and a pulse width of 10 ns (FWHM). The collinear Raman excitation beams are focused with a 300 mm lens to a waist diameter of 0.16 mm in the acceleration region of a Wiley-McLaren type time-of-flight mass spectrometer.[25] The counter-propagating UV beam is time-delayed about 50 ns and is sent through a 60 mm focal length lens to produce a tighter focus (0.13 mm waist) centered within the volume that is Raman pumped. This sampling point in the orthogonal molecular beam can be adjusted to be from three to eight cm from the nozzle opening (0.20 mm diameter) by translation of the pulsed valve source (General Valve). The generated ions are accelerated through a grid potential of 3 kV and detected with a dual microchannel plate detector in a home-built mount. The mass-selected photoion signal is recorded with a digital oscilloscope (Tektronix 2440) or a boxcar integrator (Stanford Research SR250) and is analyzed with a computer.

4.3 Results and Discussion

4.3.1 Benzene Spectra

As a test of the performance of this Raman-REMPI apparatus, some spectra were obtained for the same ν_8 region of benzene as had been examined earlier by Esherick and Owyoung.[4,5] This Raman transition gives a relatively weak perpendicular band with a rich, complex structure due to Fermi-resonance mixing of several states. As a representative example, Figure 4-1 shows a scan of one Q branch region (for K = 1). It is noteworthy that the signal to noise is comparable to that of Esherick and Owyoung[4,5] but is obtained at a calculated (isentropic jet)[56] density of $1 \cdot 10^{13}$ molecules per cm^3, about 300 times

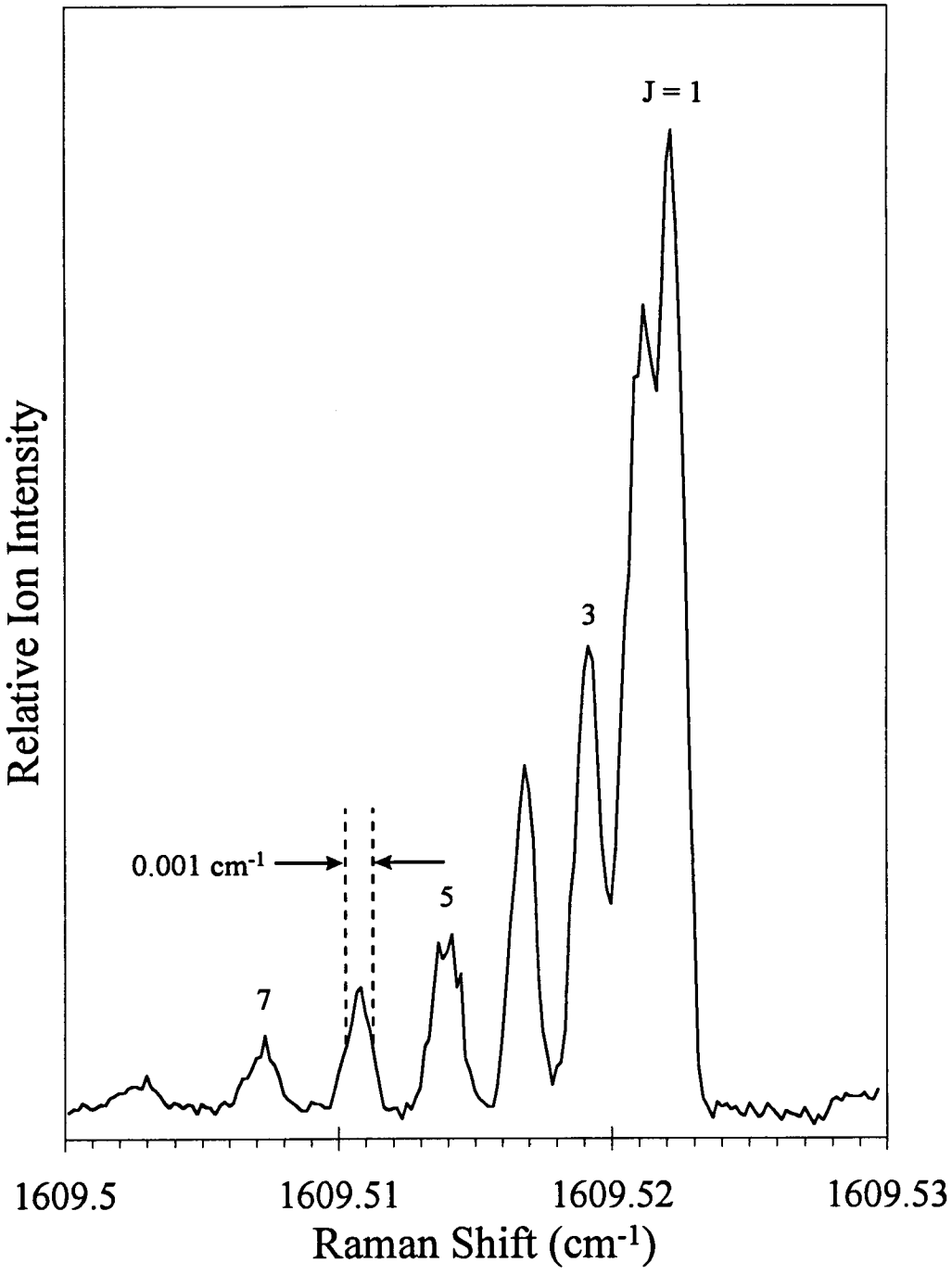

Figure 4-1 Raman-REMPI spectrum of the $^{O}Q_1$ ($\Delta J = 0$, $\Delta K = -2$, $K = 1$) transitions of the ν_8 (e_{2g}) mode of benzene in a molecular beam. The UV source (0.1 mJ) was tuned to 36474 cm^{-1} and the Raman wavenumber calibration in the figure is adjusted to match the J = 6 line reported in References 4 and 5. The expansion was 13% benzene in argon at 0.8 atm. and the sampling was done at X/D = 175 (D = 0.20 mm nozzle diameter) using pump and Stokes laser energies of 2 and 0.5 mJ.

lower than in their measurements, which were made in the high density region of a jet exiting from a Teflon channel extension of their nozzle. This "pseudo jet" produced a relatively warm sample, with a Q-branch maximum at J = 15 and no features resolved for lines below J = 6. In contrast, our spectrum shows far fewer transitions, but with well-resolved lines down to the maximum at J = 1, the lowest possible transition for the K = 1 Q-branch. From the rotational intensity distribution, we estimate the jet temperature to be about 5 K. A partition function calculation indicates that the number density for the J = 1 level is $3 \cdot 10^{11}$ cm^{-3} and, for a S/N of 1 per laser shot, we estimate that the J = 1 Q line could be detected at a state density of $3 \cdot 10^{10}$ cm^{-3}. By signal averaging, we have demonstrated that this can be lowered by a factor of 10 and perhaps another factor of 3 can be obtained by using more laser power, with a milder focus to avoid saturation and ac Stark broadening. Finally, it should be noted that the Raman cross section of this ν_{16} mode is low, more than a factor of ten less than that of the strong ν_1 ring stretching mode for benzene. Thus, in favorable cases, one might expect to achieve a detection limit of about 10^8 cm^{-3} per state with our apparatus.

The resolution of the Raman transitions in Figure 4-1 is also noteworthy. Assuming a translational temperature equivalent to the rotational value of 5 K, the Doppler width would be 9 MHz and, with a 21 MHz instrumental width, an overall linewidth of 24 MHz is predicted (collisional, natural, and transit-time linewidth contributions are assumed to be negligible). As seen in the figure, this value is in reasonable accord with the observed width of 30 MHz. The difference is attributed to AC Stark broadening, which was clearly discernible at higher pump and Stokes beam energies.

To our knowledge, these represent the narrowest lines yet recorded for any Raman transition.

4.3.2 Nitrogen Spectra

In the case of N_2, the photoionization step involves a 2 + 2 REMPI process, which is inherently less efficient than a 1 + 1 process as for benzene. Despite this, the direct 2 + 2 REMPI spectrum of the v = 0 ground state level showed a good signal-to-noise ratio for nitrogen jets, as displayed at the top of Figure 4-2. The simulated spectrum in this figure indicates that the rotational temperature was about 9 K at the X/D sampling point of 175, where the molecular density is calculated to be $2 \cdot 10^{14}$ cm^{-3}. An optical stimulated Raman spectrum would not be feasible at this density although we have previously recorded such spectra for jets at much higher driving pressures and at smaller X/D values. For example, Figure 4-3a shows such a spectrum obtained for a jet driven at 50 atm and at X/D = 5, where the density is $4 \cdot 10^{18}$ cm^{-3} and the rotational temperature is about 27 K.[57]

For these Raman-REMPI measurements it is necessary to carefully align the beams at a common point. In practice, the most convenient procedure was to generate an optical CARS spectrum for a static sample in the beam apparatus to ensure good overlap of the Raman pumping beams and to calibrate the Raman shift. By tuning to match the J = 2 Raman Q-branch line, and overlapping the Raman-pumped volume with the UV focus at X/D = 175, the Raman-REMPI spectrum shown in Figure 4-3b was obtained when the molecular beam was produced and the UV laser was scanned. The result is in good agreement with the simulated spectrum, for which it was assumed that the two-photon

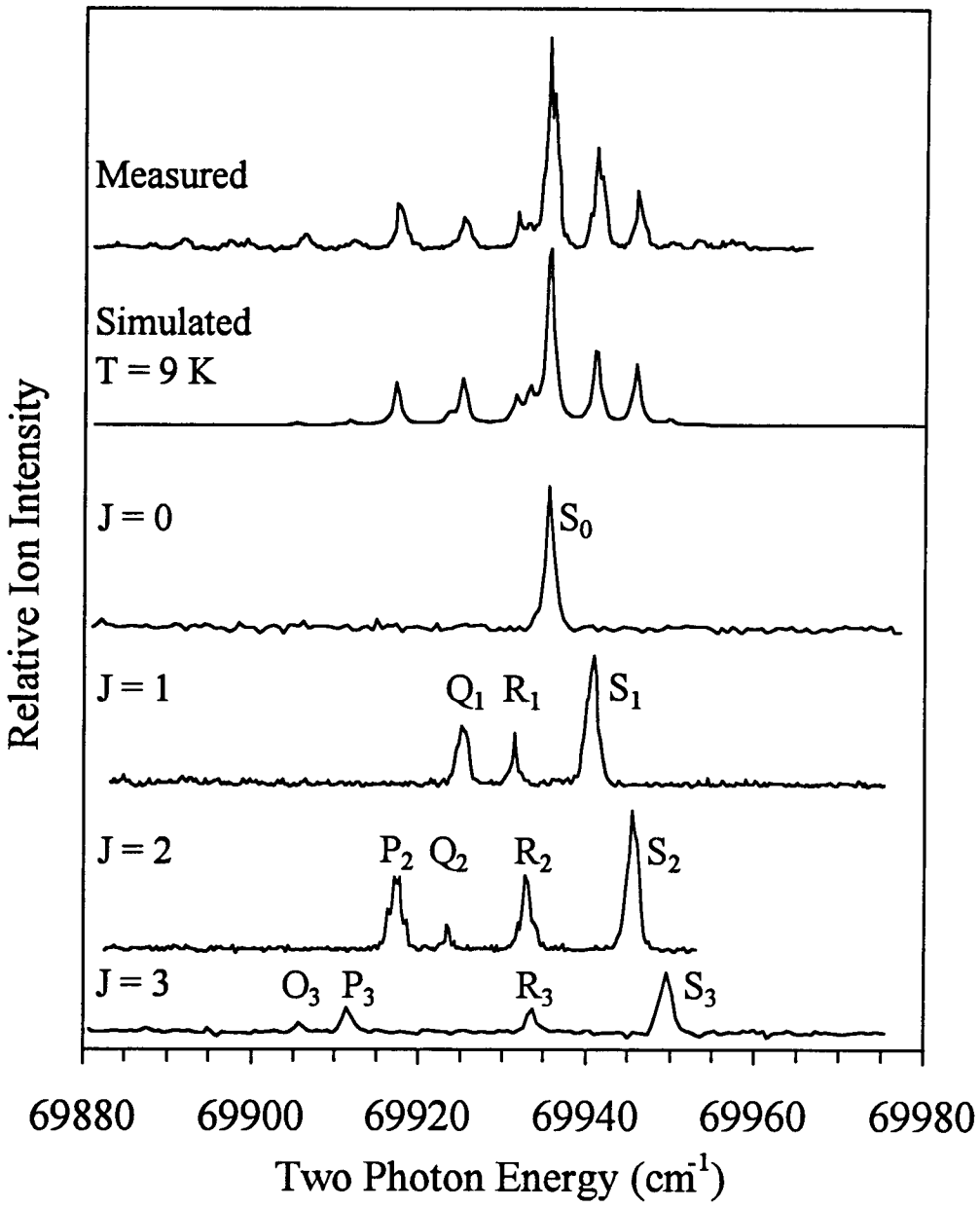

Figure 4-2 REMPI and Raman-REMPI spectra of N_2 in a neat jet at a driving gas pressure of 3.5 atm. The top trace is the 2 + 2 REMPI spectrum of the $a^1\Pi_g$ (v = 1) ← $X^1\Sigma_g$ (v = 0) transition and the simulation indicates that the rotational temperature is about 9 K. The bottom traces show the Raman-REMPI spectra obtained as the $a^1\Pi_g$ (v = 2) ← $X^1\Sigma_g$ (v = 1) UV transition is scanned for different fixed Raman excitations. (Note that the REMPI spectrum at the top has been shifted 691 cm^{-1} to the red to better show the correspondence with the lower double resonance spectra. See the level diagram and discussion of **Figure 4-3**.

resonance is the rate-determining step, so that the intensities can be calculated with the two-photon Hönl-London or transition probability factors.[58] Up to five UV transitions (O, P, Q, R, S) are possible for each initial J level but since there is orbital angular momentum in the upper electronic state of this $a^1\Pi_g \leftarrow X^1\Sigma_g$ transition, the O_2 line is absent. Similar Raman-REMPI spectra are shown in the bottom part of Figure 4-2 for cases where levels J = 0, 1, 2, or 3 were Raman-pumped and the UV laser was scanned. According to the Hönl-London factors, one expects 1, 3, 4 or 5 UV transitions in each of these respective cases. The observed patterns agree with these predictions if one takes into account that the Hönl-London factor for the Q_3 transition is very small. The spectra illustrate nicely the simplification of rotationally-resolved spectra that is possible in all double-resonance experiments.

Of course, our main objective in these measurements is to obtain high resolution Raman spectra and the ionization step is primarily to provide an enhanced detection capability. Figure 4-3c shows such a Raman trace, where the UV frequency was fixed at the S_2 position and the ring dye laser was scanned across the J = 2 Raman transition. As expected, the resultant spectrum consisted of a single sharp Raman Q_2 line whose width was 105 MHz. This width can be compared with a value of 72 MHz which is predicted from the Doppler width (30 MHz) and the 65 MHz instrumental resolution for the 12 ns Nd:YAG mode of operation that was used. Again, the excess of the measured to predicted width is attributed to AC Stark broadening as will be described in detail in chapter 5, with a partial contribution by saturation broadening also likely. An increase in the laser beam focal waist would reduce these effects while allowing full use of the

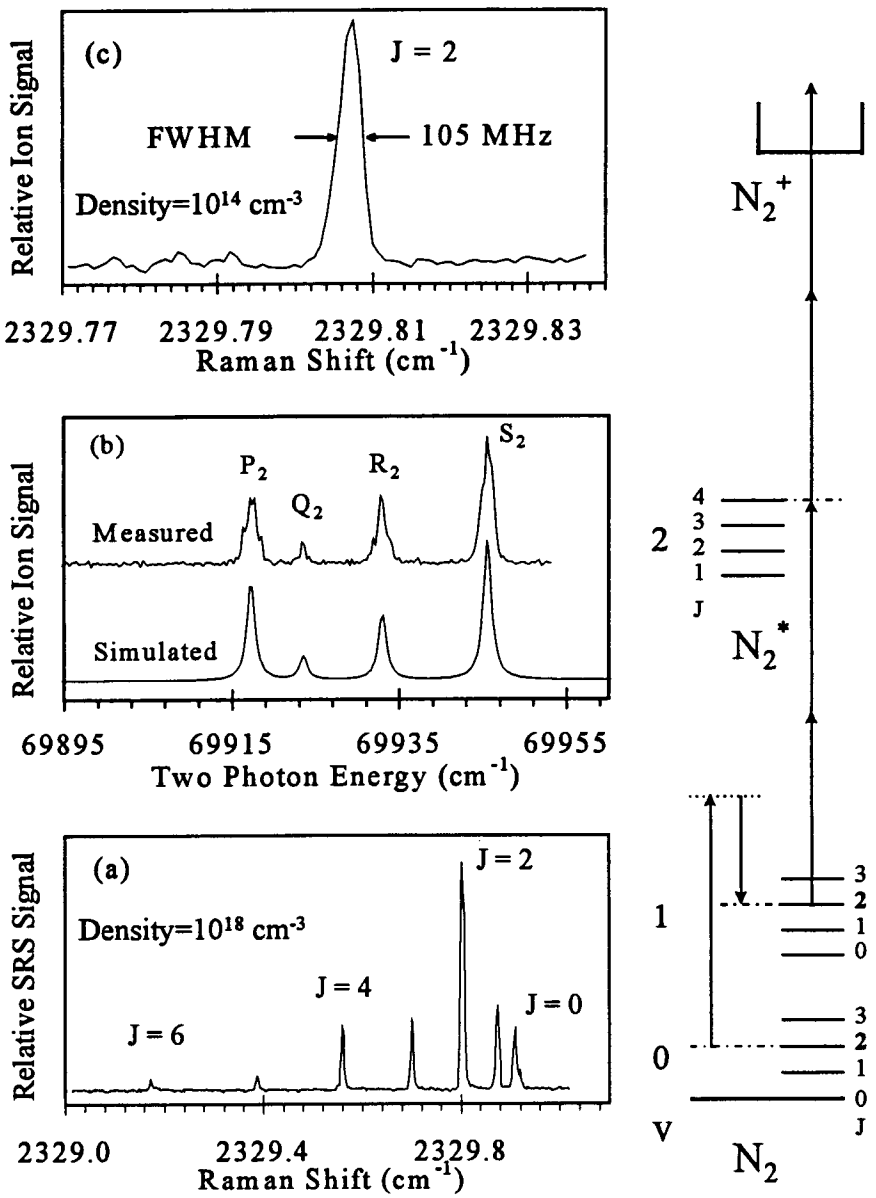

Figure 4-3 Raman-pumped 2 + 2 REMPI spectrum of N_2 taken in a jet and compared with a simulated spectrum. The energy level diagram for the process is shown to the right of the figure. (a) Optical SRS spectrum of the Q branch of N_2 cooled to about 27 K in a high density region (X/D = 5) of a free jet. The driving gas pressure was 50 atm. (b) Spectrum of N_2 in a low density region (X/D = 175) of the jet when the v = 1, J = 2 level was Raman-pumped and the ionization laser was scanned. The driving gas pressure was 3.5 atm. and the Raman pump and Stokes laser energies were 65 and 1.5 mJ. (c) Spectrum obtained when the UV laser was fixed at the S_2 line and the Raman-pumping lasers were scanned across the J = 2 line.

available laser energies, as would use of the long-pulse mode of the Nd:YAG. laser. It should be noted that the Q_2 line displayed in Figure 4-3c was obtained at a sample density 20,000 times lower than that used to obtain the optical stimulated Raman spectrum of Figure 4-3a. At the latter warm, high density position, there remains a substantial collisional broadening of the lines, whose widths are about 300 MHz.

4.4 Conclusion

The possibility of performing double resonance Raman-ionization experiments with a 2 + 2 REMPI process on difficult-to-ionize molecules, like N_2, has been demonstrated. The high resolution and excellent signal-to-noise in this case, and for the Raman 1 + 1 REMPI process in benzene, is encouraging. This suggests that a wide variety of molecules and van der Waals clusters of these can be probed at cold, low density molecular beam conditions and at a resolution adequate for detailed vibrational-rotational analysis.

5. AC STARK EFFECT ON VIBRATIONAL-ROTATIONAL ENERGY LEVELS IN SYMMETRIC TOP MOLECULES

5.1 Introduction

Stark shifts can be both helpful and difficult in interpreting the spectra of atoms and molecules. Historically, the first Stark experiments[59,60] involved the application of uniform static electric fields to induce shifts in the atomic energy levels of atoms through the electric dipole moment. With the development of microwave spectroscopy,[61] the DC Stark effect became a powerful tool for the analysis of molecular spectra; shifts of the normally degenerate M_J levels allow one to determine dipole moments and assign rotational transitions. For one such study,[62] electric fields of up to 70 kV/cm were applied to examine the DC Stark shift due to *induced* dipole moments. These experiments were quite an achievement since the Stark shifts caused by the induced dipole ($\sim\alpha E^2$) are about four orders of magnitude smaller than the permanent dipole moment ($\sim\mu E$) contribution.

It should be noted that AC fields can also produce Stark shifts through the induced dipole moment since the time averaged value of E^2 is non-zero. With the advent of high power, high resolution laser systems and nonlinear spectroscopy, the AC Stark effect has become observable and, in fact, can be the limiting factor in the spectral linewidth if the laser and Doppler contributions are negligible. Recently, several studies have been done on the influence of the Stark effect on diatomic molecules with resonant[63] and nonresonant[64] laser beams. At very high laser intensities (10^{10} W cm^{-2}) the molecules no longer freely rotate but are instead pendular oscillators in the potential of the electric field. The rotational band spectra of such so-called pendular states[65] show very distinct and

broad rotational line shapes, as shown by Felker et al. for the naphthalene trimer.[66] At lower field strengths and higher resolution, we observe more subtle shifts and line broadening, as presented here. To our knowledge there has been no quantitative analysis of such AC-Stark effects for symmetric top molecules, although the effect has been noted by other authors.[5]

In this chapter we present a derivation of the first and second order corrections to the energy levels of a symmetric top due to the nonresonant AC Stark effect. We also derive the corresponding transition intensities and discuss the selection rules for a symmetric top in an external electric field. The effect of temporal and spatial variation of the electric field, and of saturation are considered as well. We then apply our model to interpret our experimental results on the ν_8 (we use Wilson's notation throughout) e_{2g} Raman active CC stretching mode of benzene. Finally, we demonstrate for both benzene and nitrogen that the AC Stark broadening of molecular transitions can be significantly reduced in double resonance experiments with a simple imaging arrangement.

5.2 Theory

5.2.1 Calculation of Field Induced Energy Shifts

When an external electric field is applied to a nonpolar molecule, a dipole moment is induced through the molecular polarizability. If the external field is large enough, the vibrational and rotational levels can no longer be described by the field free energies. A correction term to the energy must be added through perturbation theory that accounts for

the applied external field. In general, when the external electric field is polarized along the Z-axis in the laboratory frame, the time averaged perturbation Hamiltonian due to an AC field is given by:

$$H' = -\frac{1}{4}\alpha_{ZZ}\mathsf{E}_Z^2 \qquad (5.1)$$

where α_{ZZ} is the Cartesian molecular polarizability of the molecule in the laboratory fixed frame, and E_Z is the time independent amplitude (we have already performed the time average in (5.1)). Using (5.1), the first nonzero correction to the energy is given by first order perturbation theory:

$$E_m^{(1)} = \langle m|H'|m\rangle. \qquad (5.2)$$

In order to facilitate the evaluation of the energy correction matrix elements (5.2) and also to discuss the IDSRS transition intensities, it is very convenient to introduce the spherical (irreducible) tensor components, α_p^q, where q is the rank of the tensor and p is the component index. We relate the 9 linearly independent Cartesian tensor components to spherical tensor components with the following expressions:[67]

$$\alpha_0^0 = -\sqrt{\frac{1}{3}}\left(\alpha_{XX} + \alpha_{YY} + \alpha_{ZZ}\right), \qquad (5.3a)$$

$$\alpha_0^2 = +\sqrt{\frac{1}{6}}\left(2\alpha_{ZZ} - \alpha_{XX} - \alpha_{YY}\right), \qquad (5.3b)$$

$$\alpha_{\pm 1}^2 = \mp\left(\alpha_{XZ} \pm i\alpha_{YZ}\right), \qquad (5.3c)$$

$$\alpha_{\pm 2}^2 = \frac{1}{2}\left(\alpha_{XX} - \alpha_{YY}\right) \pm i\alpha_{XY}, \qquad (5.3d)$$

The three remaining antisymmetric first rank tensor components α^1_0, $\alpha^1_{\pm 1}$ are nonzero only for the case of resonant Raman spectroscopy, which is not considered here.

The laboratory fixed spherical tensor components, α^J_M, can be expressed in terms of the components for the molecule fixed coordinate system, $\bar{\alpha}^J_K$, with the use of the Wigner rotation matrices,[68]

$$\alpha^J_M = \sum_{K=-J}^{J} D^J_{MK}(\varphi,\vartheta,\chi)^* \; \bar{\alpha}^J_K \qquad (5.4)$$

Using equations (5.3a), (5.3b), and (5.4) we note that only the $K = 0$ terms in the molecular polarizability are invariant to rotations and give a non-zero result in (5.2) (in the molecule-fixed coordinate system, the equilibrium polarizability elements $\alpha^2_{\pm 1}$ and $\alpha^2_{\pm 2}$ are zero by symmetry since $\alpha_{xx} = \alpha_{yy}$ and $\alpha_{ij} = 0$ if $i \neq j$). The Stark shift Hamiltonian can thus be expressed as:

$$H' = \frac{1}{4}\sqrt{\frac{1}{3}}\, D^{0\,*}_{00}\, \bar{\alpha}^0_0\, \mathsf{E}^2_Z - \frac{1}{2}\sqrt{\frac{1}{6}}\, D^{2\,*}_{00}\, \bar{\alpha}^2_0\, \mathsf{E}^2_Z . \qquad (5.5)$$

where we have dropped the explicit display of the angular coordinates in the Wigner rotation matrix. For the specific case of a symmetric top we use the relations,

$$-\sqrt{\frac{1}{3}}\bar{\alpha}^0_0 = \alpha$$

and

$$\bar{\alpha}^2_0 = 2\sqrt{\frac{1}{6}}\left(\alpha_{zz} - \alpha_{xx}\right) = 2\sqrt{\frac{1}{6}}\,\gamma$$

where α is the isotropic part the molecular polarizability tensor and γ is the anisotropy. With the above definitions and considering that $D^{0\,*}_{00} = 1$, (5.5) simplifies to

$$H' = -\frac{1}{4}\alpha \mathsf{E}_z^2 - \frac{1}{6} D^{2\,*}_{00}\, \gamma \mathsf{E}_z^2 . \qquad (5.6)$$

Substitution of (5.6) into (5.2) gives for the energy

$$\begin{aligned} E^{(1)}_{JKM} &= -\frac{1}{4}\alpha \mathsf{E}_z^2 - \frac{1}{6}\gamma \mathsf{E}_z^2 \left\langle JKM \middle| D^{2\,*}_{00} \middle| JKM \right\rangle \\ &= -\frac{1}{4}\alpha \mathsf{E}_z^2 - \frac{1}{6}\gamma \mathsf{E}_z^2 (-1)^{(M+M)-(K+K)} \frac{\sqrt{(2J+1)(2J+1)}}{8\pi^2} \\ &\qquad * \int D^{J}_{-M-K}(\Omega) D^{2\,*}_{00}(\Omega) D^{J\,*}_{-M-K}(\Omega)\, d\Omega \end{aligned} \qquad (5.7)$$

where we have used

$$|JKM\rangle = \sqrt{\frac{2J+1}{8\pi^2}} D^{J}_{M,K} = (-1)^{M-K} \sqrt{\frac{2J+1}{8\pi^2}} D^{J}_{-M,-K} . \qquad (5.8)$$

as the definition of the symmetric top states $|JKM\rangle$.[68] To evaluate the integral in (5.7) we make use of the general expression for the triple product integral,

$$\int D^{J''}_{M''K''}(\Omega) D^{J'}_{M'K'}(\Omega) D^{J}_{MK}(\Omega)\, d\Omega = 8\pi^2 \begin{pmatrix} J & J' & J'' \\ M & M' & M'' \end{pmatrix} \begin{pmatrix} J & J' & J'' \\ K & K' & K'' \end{pmatrix} . \qquad (5.9)$$

Substituting (5.9) into (5.7) using $J = J''$, $M = M''$, $K = K''$, $J' = 2$, and $M' = K' = 0$, we find the first order Stark energy shifts are given by

$$E^{(1)}_{J,K,M} = -\frac{1}{4}\mathsf{E}_z^2 \alpha - \frac{1}{6}\gamma \mathsf{E}_z^2 \frac{\left[J(J+1) - 3M^2\right]\left[J(J+1) - 3K^2\right]}{J(J+1)(2J-1)(2J+3)} . \qquad (5.10)$$

The first term shifts all the energy levels by the same amount and can be ignored when calculating transition energies, but the second term has a complicated JKM dependence

that splits out the $|M|$ degeneracy. As an example of the M sub-level splittings, Figure 5-1 shows the relative M-splitting patterns for the ^{S}S branch up to $J = K = 12$, setting $1/6\gamma E_Z^2 = 1$. Note that the degeneracy is not completely removed since $\pm M$, $\pm K$ states still have the same energy due to the squared terms in equation (5.10). In general, the splitting decreases as J increases because of the denominator in (5.10) and, for $K = 0$, the $M = 0$ level is the lowest in energy. It is noteworthy that in the sequence of transitions shown by circles in Figure 5-1 the M sub-levels split out toward lower energy until the width of the lines become a minimum. Beyond this point, the order reverses and the $M = J$ value becomes the lowest in energy. This is seen in the peak asymmetries of the 5 mJ experimental spectrum of Figure 5-2, which corresponds to the circled transitions of Figure 5-1. In general, these Stark splitting patterns are unique and could be a useful aid in the analysis and assignment of spectra based on the shapes of the lines observed.

By combining equations (5.7), (5.8) and (5.9) it is possible to derive the very useful relation

$$\left\langle J''K''M'' \left| D^{J'}_{M'K'}{}^{*} \right| JKM \right\rangle = (-1)^{M''-K''} \sqrt{(2J''+1)(2J+1)} \begin{pmatrix} J'' & J' & J \\ -M'' & M' & M \end{pmatrix} \begin{pmatrix} J'' & J' & J \\ -K'' & K' & K \end{pmatrix}. \quad (5.11)$$

The advantage of using the spherical tensor form for the molecular polarizability, α, is revealed by (5.11) in two ways. First, the algebraic complexity of the matrix element is buried in the 3-j symbols, which are easily obtained in functional or numerical form using the expressions found in Zare[68] or by using symbolic algebra programs such as Mathematica and Maple. Second, the vector addition rules for the 3-j symbols place constraints on the possible combinations of the quantum numbers, viz.

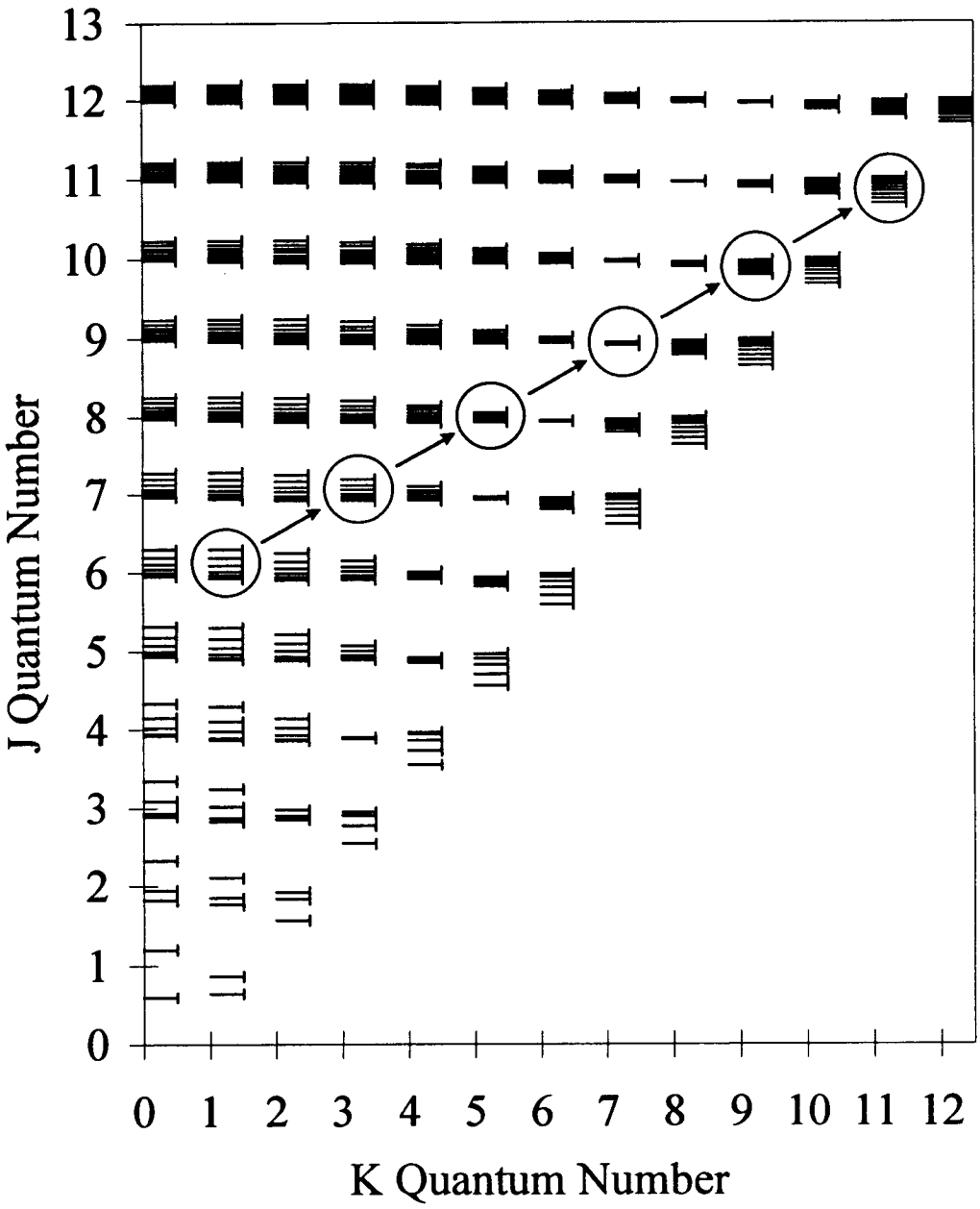

Figure 5-1 *M* Sub-level splittings for the ^{S}S-branch. The circles and arrows show the group of transitions in **Figure 5-2**.

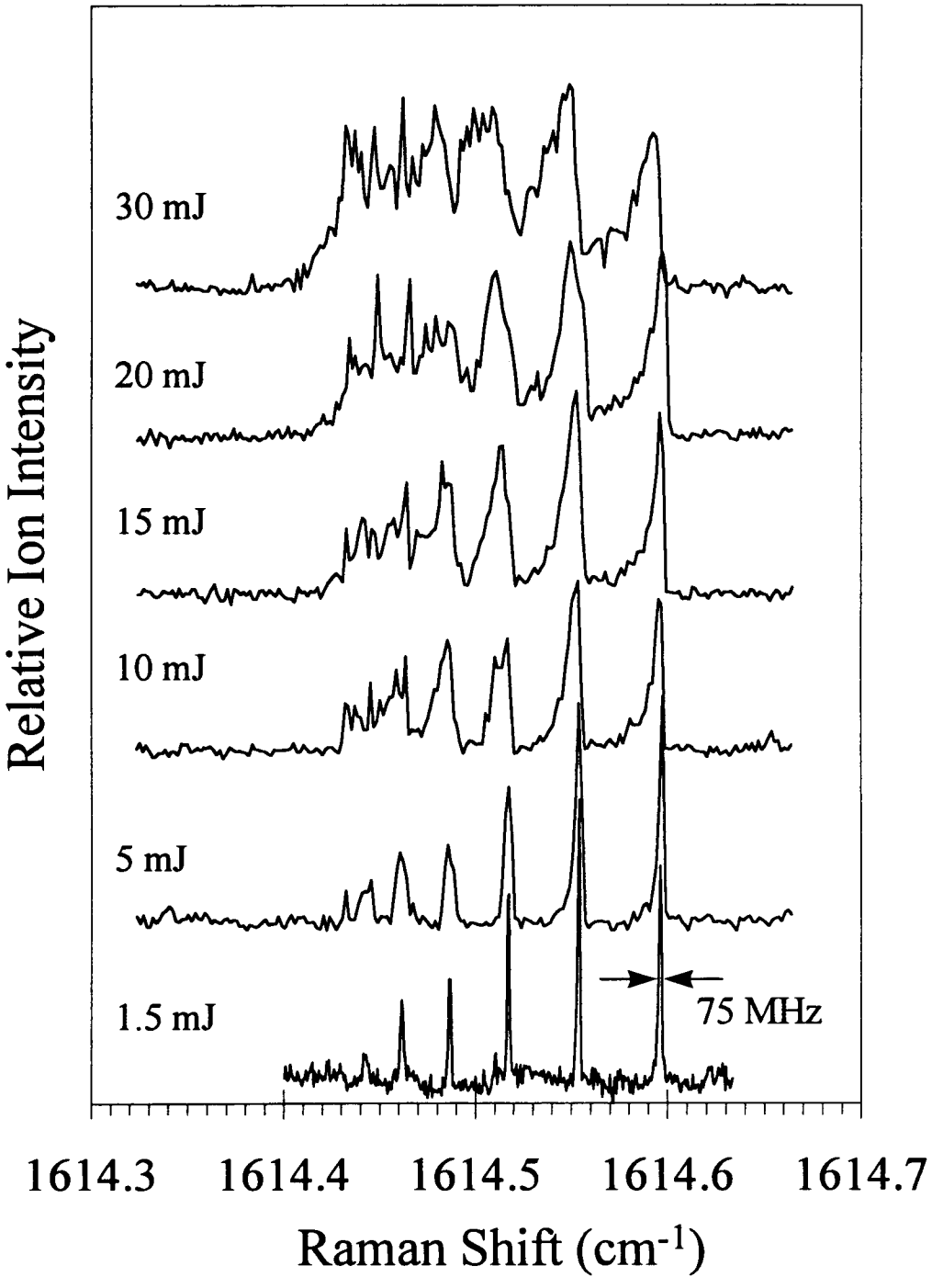

Figure 5-2 Power dependence of the ν_8 ^{S}S-branch in benzene. Two different processes contribute to the power dependent linewidth: first is the Stark splitting of the *M* sub-levels and second is saturation of the stronger transitions.

$$\left|J' - J''\right| \le J \le \left|J' + J''\right| \quad \text{(vector addition)}$$

$$-M'' + M' + M = 0, \quad -K'' + K' + K = 0 \quad \text{(algebraic component addition).}$$

This leads naturally to the selection rule constraints for transitions between vibrational/rotational levels.

The second order shifts are calculated in a similar manner as above using second order perturbation theory,

$$E^{(2)}_{JKM} = -\frac{1}{6}\gamma \mathsf{E}_Z^2 \sum_{\substack{J'=J-2,\\ J'\neq J}}^{J+2} \frac{\left|\left\langle J'KM\left|D^{2\,*}_{00}\right|JKM\right\rangle\right|^2}{E^{(0)}_{JKM} - E^{(0)}_{J'KM}}. \qquad (5.12)$$

Although it is straight forward to calculate the explicit *JKM* dependence, due to the summation over the different *J*'s, this expression is not as simple as the first order correction and the result is given in Appendix B. Note that there is no *K*, *M* mixing since the $D^{2\,*}_{00}$ operator doesn't connect states with differing *K*, *M*'s. For intensities used in our experiment the second order term is negligible in comparison to the first order correction and it was not included in the modeling of our experimental data.

5.2.2 Calculation of IDSRS Transition Intensities

The calculation of the overall IDSRS intensity can be simplified by breaking the double resonance process into parts. The first two parts correspond to the Raman pumping step and the resonant UV transition to the upper electronic state. We assume that the probability for ionization from the upper electronic state is uniform for all

rotational states. To begin, we first consider the Raman intensity contribution and then find the UV intensity factor. The overall intensity is simply the product of expressions.

The Raman transition intensity for an AC light field polarized along the Z-axis is proportional to

$$\left|\left\langle \mathrm{v}'J'K'M' \left| \alpha_{ZZ} \right| \mathrm{v}JKM \right\rangle\right|^2 . \qquad (5.13)$$

With the use of (5.3a,b) we can express α_{ZZ} in terms of the space fixed spherical tensor elements

$$\alpha_{ZZ} = -\sqrt{\frac{1}{3}}\alpha_0^0 + \sqrt{\frac{2}{3}}\alpha_0^2 \qquad (5.14)$$

and then transform the right side of this equation to the molecule fixed coordinate system with the use of expansion (5.4)

$$\alpha_{ZZ} = -\sqrt{\frac{1}{3}} D_{00}^{0\,*} \bar{\alpha}_0^0 + \sqrt{\frac{2}{3}}\left[D_{00}^{2\,*} \bar{\alpha}_0^2 + D_{01}^{2\,*} \bar{\alpha}_{\pm 1}^2 + D_{02}^{2\,*} \bar{\alpha}_{\pm 2}^2 \right]. \qquad (5.15)$$

From the D_{6h} character table, it can be seen that the symmetries of the polarizabilities are $a_{1g}(\bar{\alpha}_0^0, \bar{\alpha}_0^2)$, $e_{1g}(\bar{\alpha}_{\pm 1}^2)$, and $e_{2g}(\bar{\alpha}_{\pm 2}^2)$ (note that the $\bar{\alpha}_K^J$ elements form linear combinations of the Cartesian elements α_{xx} etc. which is what is usually displayed in such character tables). For an e_{2g} vibrational transition then, only the last term of (5.15) contributes to the Raman intensity. Assuming that the vibrational and rotational wavefunctions are separable gives for the intensity of such an e_{2g} transition

$$\left|\left\langle J'K'M' \left| D_{02}^{2\,*} \right| JKM \right\rangle \left\langle \mathrm{v}' \left| \bar{\alpha}_{\pm 2}^2 \right| \mathrm{v} \right\rangle\right|^2 . \qquad (5.16)$$

The vibrational part can be evaluated by expanding $\bar{\alpha}_{\pm 2}^2$ in terms of the normal coordinates of the molecule

$$\bar{\alpha}_{\pm 2}^2 = \left(\bar{\alpha}_{\pm 2}^2\right)_0 + \sum_i \left(\frac{d\bar{\alpha}_{\pm 2}^2}{dq_i}\right)_0 q_i + \dots \,, \qquad (5.17)$$

which determines the Raman vibrational selection rules. Note that $\left(\bar{\alpha}_{\pm 2}^2\right)_0 = 0$ and that only the normal coordinate with e_{2g} symmetry in the expansion contributes to the transition of interest.

The Wigner rotation operator that is determined by the e_{2g} vibration is thus the $D_{02}^{2\,*}$ element. It is this operator that governs the selection rules and corresponding intensities for the rotational transitions between the two vibrational states. Assuming that the vibrational contribution to the intensity is constant for all the rotational transitions, the relative rotational Raman intensities are given by

$$I_{Raman} = g_{JKM}\, e^{-\frac{E_{JKM}}{kT}} \left| \left\langle J'K'M' \left| D_{02}^{2\,*} \right| JKM \right\rangle \right|^2 , \qquad (5.18)$$

where g_{JKM} accounts for the nuclear spin, K^2, and M^2 degeneracy, $\exp(-E_{JKM}/kT)$ is the Boltzmann population and the last factor is the Raman transition probability. Since the M sub-levels are split by the electric field, we do not sum over the M's.

If the external electric field is strong enough, the states in (5.18) may mix appreciably and therefore should be corrected with first order perturbation theory, or, at very high field strengths, found by explicit diagonalization of the Hamiltonian. At the field

strengths used in our experiment the corrections are small, as can be seen in Figure 5-3. This diagram shows the coefficients for the first order corrected wavefunctions

$$|iKM\rangle = |JKM\rangle + a_{J-2,K,M}|J-2KM\rangle + b_{J-1,K,M}|J-1KM\rangle + c_{J+1,K,M}|J+1KM\rangle + d_{J+2,K,M}|J+2KM\rangle \quad (5.19)$$

where each coefficient is given by the expression

$$a_{J'KM} = \frac{\gamma E^2}{6} \frac{\left\langle J'KM \left| D_{00}^{2\,*} \right| JKM \right\rangle}{E_{JKM}^{(0)} - E_{J'KM}^{(0)}}. \quad (5.20)$$

It is clear that the contributions by the other states are only on the order of a few percent at the laser powers used and can be neglected in our analysis. This simplifies the calculation of the Raman intensities enormously since if (5.19) is used in (5.18), there are 15 non-zero elements that must be calculated, each of which has a very complicated *JKM* dependence.

The UV transition is also of e_{2g} symmetry and using the same arguments as above to separate the electronic/vibrational and rotational parts of the dipole moment operator, we find that the rotational transition intensities are determined by the Wigner operator $D_{01}^{1\,*}$. The relative UV rotational transition intensities are then given by

$$I_{UV} = \left| \left\langle J''K''M'' \left| D_{01}^{1\,*} \right| J'K'M' \right\rangle \right|^2. \quad (5.21)$$

Note that there is no sum over the *M* sub-levels for this term either, even though the Stark field has been turned off when the UV laser fires and all the *M* levels have again become degenerate. The reason for this is that during the Raman pumping step we populate a specific *JKM* state–not every $M = -J \ldots +J$. The result is that after the Raman lasers have

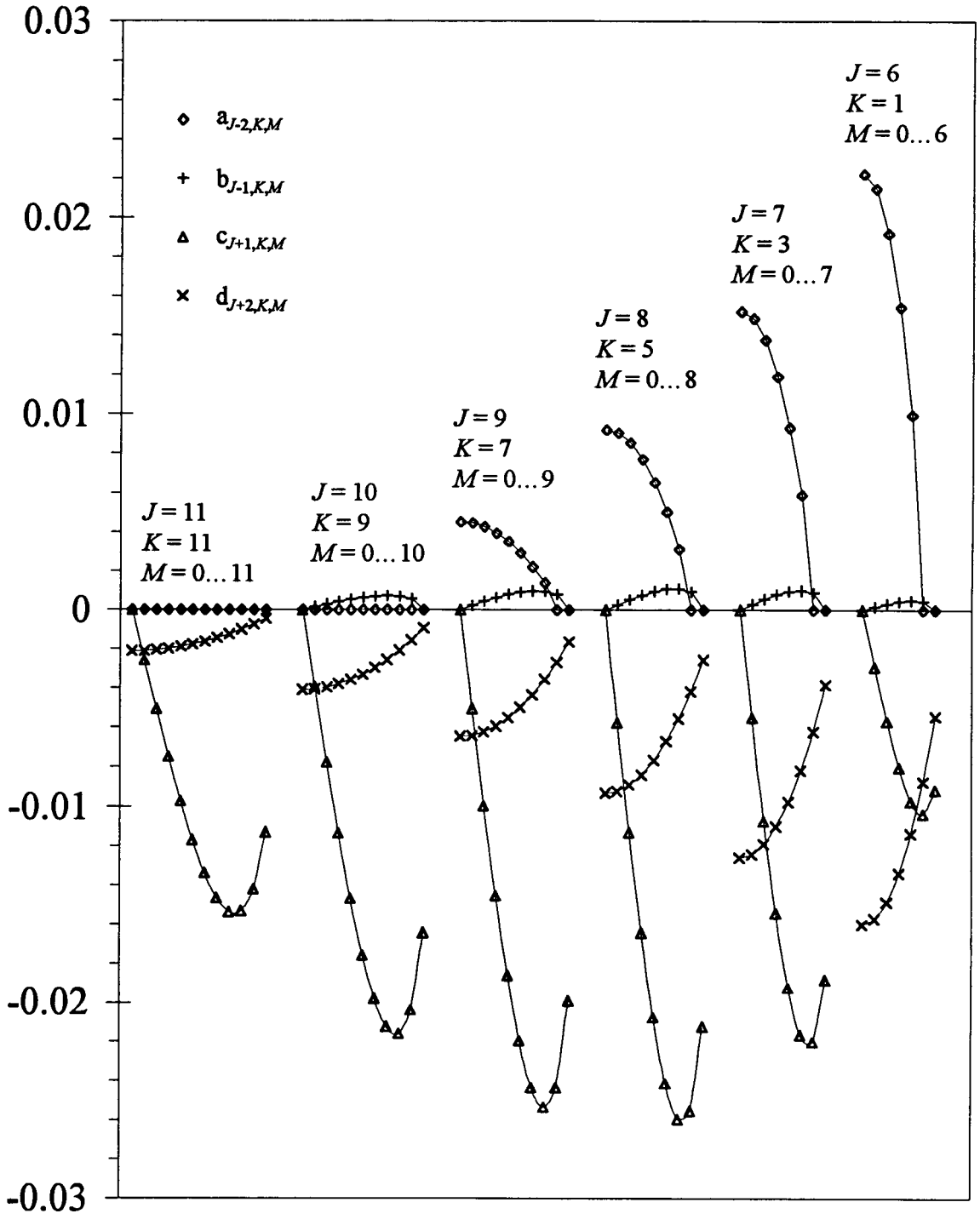

Figure 5-3 Normalized coefficients for the first order corrected wavefunctions in a AC Stark field.

turned off, only those states that are populated by Raman pumping can be ionized so the UV intensity only depends on the probability to ionize from those levels.

The overall IDSRS intensity is just the product of (5.18) and (5.21)

$$
\begin{aligned}
I_{IDSRS} &= I_{UV} I_{Raman} \\
&= g_{JKM} e^{-\frac{E_{JKM}}{kT}} \left| \left\langle J''K''M'' \left| D_{01}^{1\,*} \right| J'K'M' \right\rangle \right|^2 \left| \left\langle J'K'M' \left| D_{02}^{2\,*} \right| JKM \right\rangle \right|^2 \\
&= g_{JKM} e^{-\frac{E_{JKM}}{kT}} (2J''+1)(2J'+1)^2(2J+1) \begin{pmatrix} J'' & 1 & J' \\ -M'' & 0 & M' \end{pmatrix}^2 \\
&* \begin{pmatrix} J'' & 1 & J' \\ -K'' & 1 & K' \end{pmatrix}^2 \begin{pmatrix} J' & 2 & J \\ -M' & 0 & M \end{pmatrix}^2 \begin{pmatrix} J' & 2 & J \\ -K' & 2 & K \end{pmatrix}^2
\end{aligned}
\qquad (5.22)
$$

No single explicit expression can be written for (5.22) for all of the rotational branches that are allowed. Instead, a separate expression for each rotational branch must be determined using the explicit expressions for the 3-j symbols of each specific transition of interest.

5.3 Experimental

Ionization-detected stimulated Raman spectroscopy[3] (IDSRS) was used to record all the high resolution Raman spectra. IDSRS is unusual because it allows us to perform Raman spectroscopy in the low density region of a molecular jet. Previous measurements have indicated that we can probe state densities as low as 10^{11} cm^{-3}, even for the weak ν_8 mode in benzene.[69] Probing in this low density region has the advantage that the translational and rotational temperatures are on the order of 5 K, so Doppler contributions to the Raman line width are only about 9 MHz FWHM. Combining the Doppler contribution with our 21 MHz instrumental width gives an overall expected linewidth of

24 MHz. This high resolution is crucial for resolving the very small Stark shifts in the Raman spectra. For example, with 1 mJ laser pulses we expect relative Stark shifts on the order of 2 MHz.

A diagram of the experimental setup was shown previously in Figure 2-1. As noted earlier, the use of counter-propagating beams for the Raman and UV made the alignment procedure much easier. The focal lengths of the green and UV differ by approximately 2 cm for collimated beams focused through a 26 cm lens, making it difficult to overlap the focal volumes with just one lens. By using two lenses we not only eliminate this problem, but we can then use a much shorter focal length lens for the UV so molecules with large ionization potentials such as N_2 can be photoionized. A side benefit of the tighter UV focus will be discussed later for the IDSRS spectra of N_2.

5.4 Comparison of Experiment with Theory

5.4.1 Benzene

There are two processes that contribute to the power dependent broadening of the spectra shown in Figure 5-2. First is the Stark splitting that produces an asymmetric line shape and which can be modeled with the energy correction (5.10) and intensities calculated with (5.22). The second process is caused by saturation of the stronger transitions. Saturation of the lines causes them to broaden out and reduces the peak intensities as well. This is because when the intensity of the laser is very high an appreciable number of molecules can be pumped into the upper Raman state. Since the

Raman transition intensity depends on the population difference between the upper and lower state (note that in (5.22) we have assumed that the population in the final state is zero), this increase in population of the upper state decreases the intensity of the transition being pumped. Strong transitions tend to saturate more easily than weak ones, so the overall effect is to decrease the peak intensity of the strong transitions relative to the intensity of the weak transitions. In order to understand some of the details of these broadening effects we made an effort to reproduce the line shapes of Figure 5-2.

5.4.2 Simulation of the Benzene IDSRS ^{S}S-Branch Spectra

Accurate replication of the line shapes in the experimental spectra of Figure 5-2 with computer simulation turns out to be a fairly involved process. This is because the line shapes are a complicated convolution of the intensity dependent Stark shifts with saturation that is a function of the laser temporal and spatial intensity profile. There is no simple closed form expression for the Raman signal, which is given by the integral over time of the pulse and over the spatial extent of the laser beam at the focus. However a numerical integration is done in the following computer simulation of the experimental spectra.

The starting point for the simulation is a stick spectrum calculated using (5.8) and (5.15). To each of these lines a Voigt profile is added that takes into account the combined Gaussian laser and Doppler linewidths, $\Gamma_{eff}^{\ 2} = \Gamma_{laser}^{\ 2} + \Gamma_{Doppler}^{\ 2} = 0.001\ cm^{-1}$, as well as the intrinsic Lorentzian linewidth of the transitions, Γ_0, which was taken in our calculations to be $0.0001\ cm^{-1}$. These contributions to the linewidth are small and if they

were the only cause of broadening, and the electric field were really a constant in time, almost all of the Stark split transitions would be resolved as shown in Figure 5-4 part a) where a constant laser energy of 30 mJ was assumed with a 120 micron diameter spot size for the focused beam. In fact, saturation and the temporal/spatial field variations clearly must be included to model the spectra at the higher laser intensities in Figure 5-2.

Saturation of a transition occurs when the rate of Raman pumping from the lower to an upper level is large enough to cause an appreciable population change, producing in the upper limit equal number densities for both states so that $\Delta = N_{lower} - N_{upper} = 0$, and no net signal results. The pumping rate is proportional to the line strength of the transition, S_{JKM}, and the laser intensity product, $I_1 I_2$. In the cw limit, saturation can be accounted for by modifying the intrinsic linewidth with a term that accounts for the Raman transition effect on the upper state lifetime,[70]

$$\Gamma^2 = \Gamma_0^{\,2} + \left(a S_{JKM} I_1 I_2\right)^2 . \qquad (5.23)$$

Here the a is a fitting parameter that scales the magnitude of the saturation. It should be noted that a, the minimum beam waist (used in calculating the electric field), and a single Boltzmann temperature (deduced from a fit of the low power spectra) are the only three fitting parameters that are used in modeling all of the spectra shown in this chapter. The result of including (5.23) in the Voigt profile at a constant laser energy (30 mJ) is shown in part b) of Figure 5-4. Examination of the simulated spectrum shows that, while this model for saturation broadens out the individual lines, the overall experimental contours are not reproduced very well. The high JK peaks to the right of the figure are saturated too much, while for the lower JK transitions, the baseline is too low and the peak

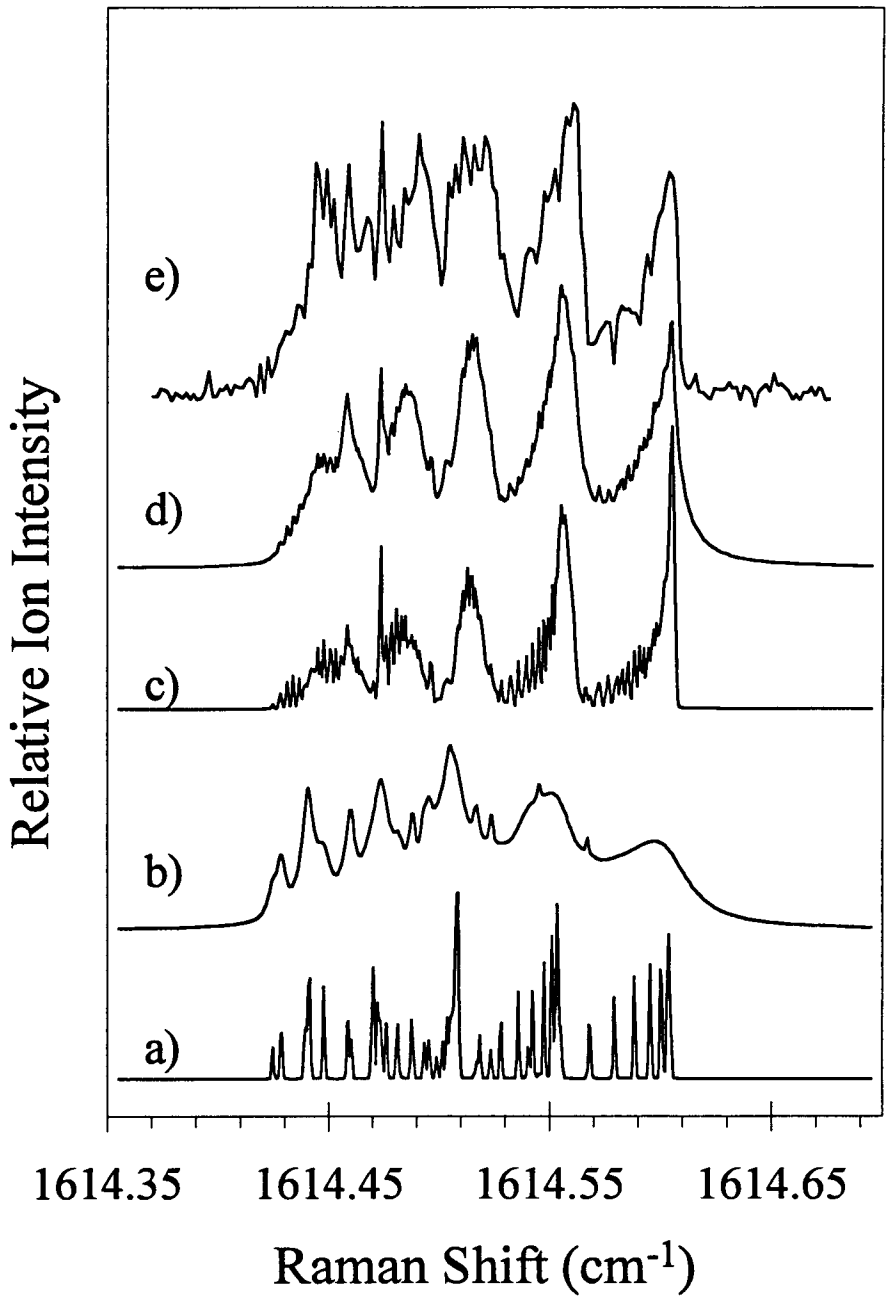

Figure 5-4 Comparison of the different levels of simulation with the 30 mJ experimental spectrum in e). a) shows the Stark shift stick spectrum with a constant average power of 30 mJ. b) adds saturation to part a). c) accounts for the temporal variation of the power by summing each time slice with the corresponding Raman pumping efficiency. d) adds to c) the spatial variation of the power at the focus, which is assumed to be of a Gaussian profile.

positions are shifted in comparison to the experimental data. It is interesting to note that the spikes at 1614.545 and 1614.568 cm^{-1} on top of the broad peaks are not artifacts but rather are a result of weak transitions growing in intensity relative to the strong transitions due to saturation. These weak transitions are much narrower in linewidth but have a comparable intensity to the strong transitions as demonstrated in Figure 5-5 for the case of the weakest and strongest transitions in the simulated spectrum. It is possible that a more explicit temporal integration (instead of using the cw model) of the saturation effect would improve this result, however it is our belief that other spatial and temporal effects are more important.

If there were no saturation and the only source of broadening was Stark splitting, we would see much different lineshapes. The lineshapes will be smeared out because the Stark shifts are not the same for every molecule at any given time so that in general each line will have an asymmetric shape. Not all the molecules in the focus of the laser beam experience the same Stark shifts for two reasons. First, our laser pulse has a Gaussian temporal shape

$$I(t) = I_0 e^{-\frac{t^2}{\tau^2}}. \qquad (5.24)$$

The consequence of this is that initially, as the laser is turned on the Stark shifts for molecules at a particular point in the laser beam are negligible, but as the laser pulse develops the M sub-levels start to split out to their maximum. Then, as the pulse dies out, the Stark shifts become negligible again. The second reason is that the intensity profile of the beam is given by

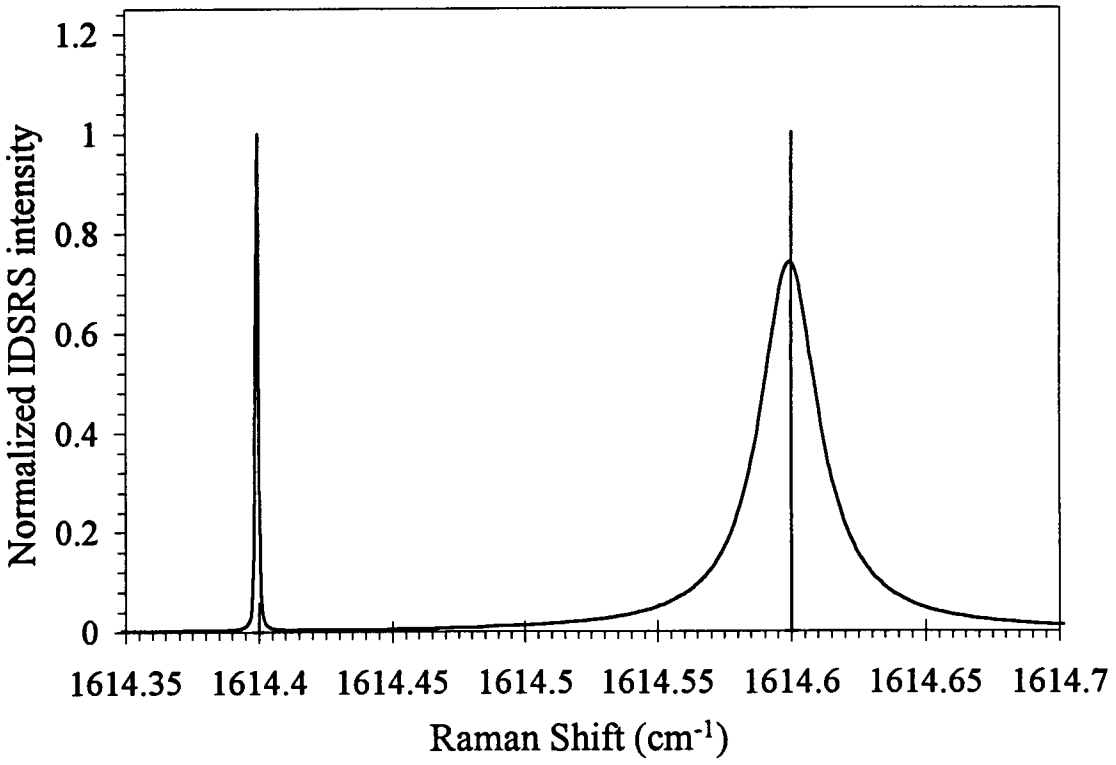

Figure 5-5 Comparison of the strongest IDSRS transition with the weakest for the two cases of the stick intensities and then with the inclusion of saturation. Notice that the weaker transition has a larger amplitude with a linewidth of about 25 times smaller than the stronger transition. The frequencies are not where the actual transitions occur–they have be separated so they don't overlap.

$$I(r,z) = I_0\left(\frac{w_0}{w(z)}\right)^2 e^{-\frac{2r^2}{w(z)^2}} \qquad (5.25)$$

so for any particular time, molecules that are in different parts of the beam experience a different Stark shift. Figure 5-6 is a contour plot that shows where the molecules will experience a constant Stark shift for a given point in time. The result of these two effects

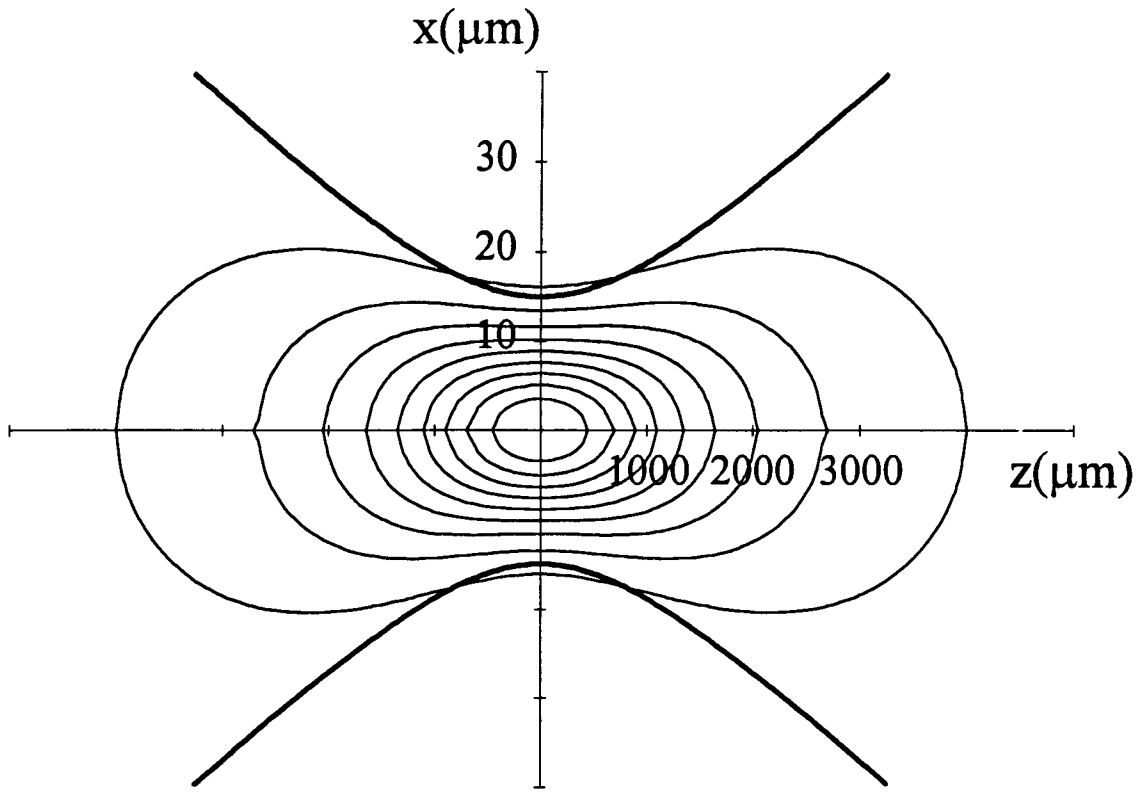

Figure 5-6 Contour plot of the intensity of the laser at the focus. Each contour corresponds to a ten percent change in the normalized peak intensity I / I_0. The two heavy lines plot the beam waist at the I / e^2 point in the radial direction as a function of z.

is that first order energy correction, (5.10), is modified to account for the spatial and temporal variations of the electric field

$$E^{(1)}_{J,K,M} = -\left\{\frac{1}{4}\alpha + \frac{1}{6}\gamma \frac{\left[J(J+1) - 3M^2\right]\left[J(J+1) - 3K^2\right]}{J(J+1)(2J-1)(2J+3)}\right\} * E_0^2\left(\frac{w_0}{w(z)}\right)^2 e^{-\frac{2r^2}{w(z)^2}} e^{-\frac{t^2}{\tau^2}} . \quad (5.26)$$

The signal measured in our experiment is the convolution of the instrumental and intrinsic linewidths with the stick spectrum integrated over time and space, which has no analytical solution. In order to approximate our measured spectra, we therefore break the time and space parts into nine pieces each and then calculate the convolved spectra that correspond to the 81 space-time slices. For the temporal integration each transition is given a Voigt profile and the resulting spectrum is weighted by the Raman pumping efficiency, which is proportional to $I_1 I_2$. The weighting factors for the spatial integration are different because the Stark shifts depend on the intensity of the laser in the particular volume element they are in. To calculate the weighting factor, we find the contours (Figure 5-6) that correspond to a constant field and then numerically compute the differential volumes at an increment of ten percent the maximum normalized intensity. We then multiply each spectrum by the product of the intensities of both the Raman lasers and the UV laser. The intensity of the UV is added because the IDSRS signal from a particular volume element is proportional not only to the Raman pumping efficiency but the efficiency of ionization as well. Summing all the spectra with the appropriate weighting factors results in the spectrum shown in part c) of Figure 5-4. The contours are not smooth due to the finite increments in the summation and would smooth out with a finer increment. The two sharp spikes at the left of the spectrum are a result of the fact that the lower energy, less saturated contribution is weighted more than the higher energy more saturated part of the spectrum as demonstrated by Figure 5-7, which shows the relative weights given to each of the spectra in the summation as a function of the normalized intensity. This spectrum in part c) has the correct trends of the experimental

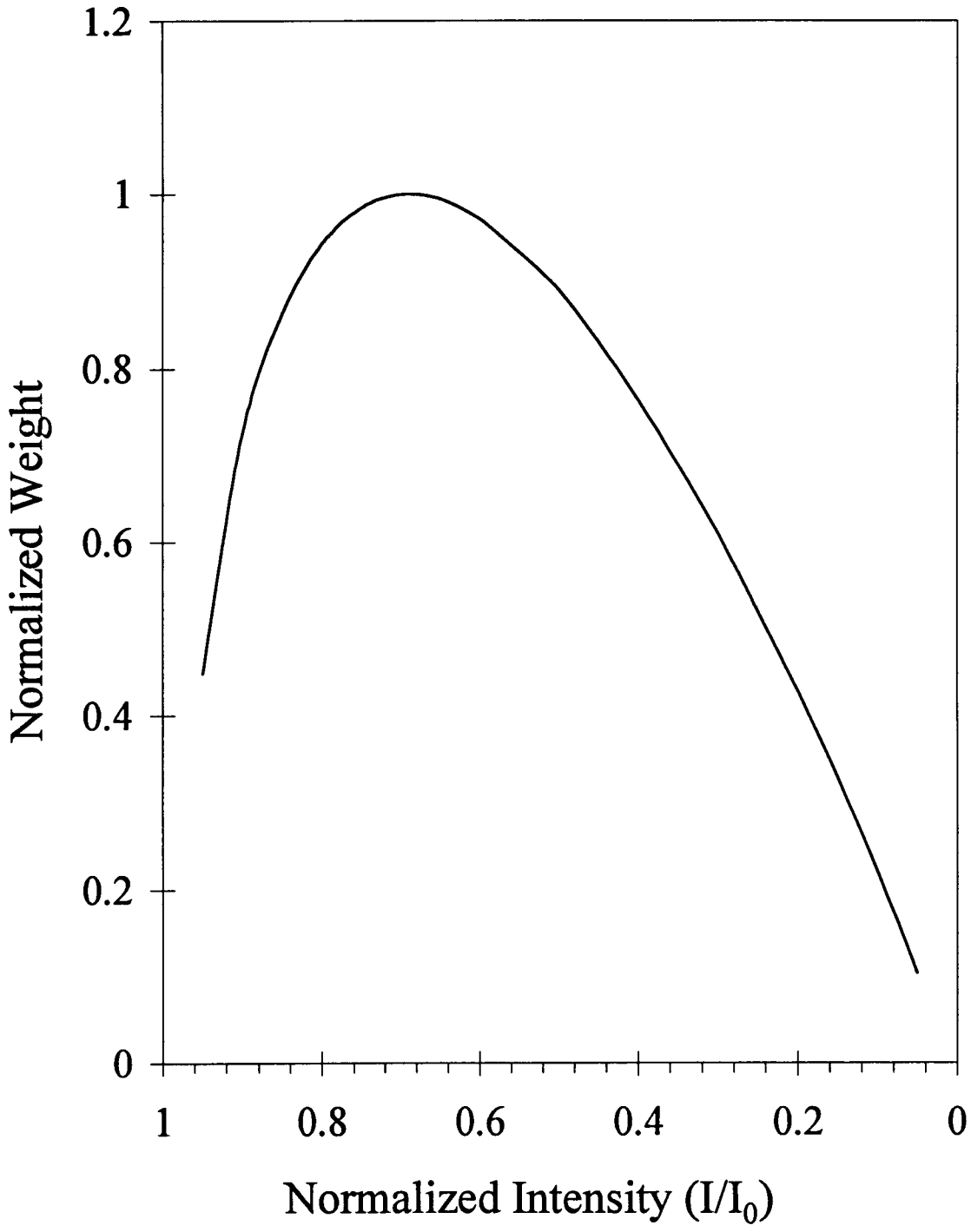

Figure 5-7 A plot of the weighting factor as a function of the normalized spatial intensity. Notice that the effect of including the weighting factor in the spatial integration is to increase the influence of the lower intensity part of the laser beam.

spectrum but the lines are still too narrow which indicates that we must include saturation with the temporal/spatial broadening.

The result of including both sources of broadening is shown in Part d) of Figure 5-4. We see that this comes very close to the experiment, although the lower J,K lines at the left of the spectrum have slightly different linewidths. Using the same saturation factor and varying only the laser energy from 30 mJ to 15 and 1.5 mJ we see that the basic features of the experimental spectra are reproduced very well in Figure 5-8.

5.4.3 Q-Branch Spectra

For the case of Q-branch spectra where $\Delta J = \Delta K = 0$, there is a greatly reduced Stark effect because the shift is nearly the same in the upper and lower vibrational energy levels. The main source of broadening (other than saturation) is due to the difference in the isotropic ($\Delta\alpha$) and anisotropic ($\Delta\gamma$) polarizabilities for the upper and lower states, with the former terms likely to be larger since α is usually greater than γ. Thus, the Stark effect is small for the linear molecule case (described with (5.10) by setting $K = 0$). This is also true for symmetric top ^{Q}Q-branch transitions where $\Delta J = \Delta K = 0$. However, because of the additional K dependence in the energy, there will be Stark broadening for Q-branch lines when $\Delta K \neq 0$, e.g. for ^{O}Q, ^{P}Q, ^{R}Q, and ^{S}Q bands. One exception to this is for the $K = 1$ ^{O}Q-branch shown in Figure 5-9. This branch is unusual in that $\Delta J = 0$ and $\Delta K = -2$, and because the energy depends only on K^2, we see no appreciable Stark broadening for this branch (K goes from $K = 1$ in the lower state to $K = -1$ in the upper state, so the K^2 term effectively drops out). Therefore the primary source of broadening for the spectra in

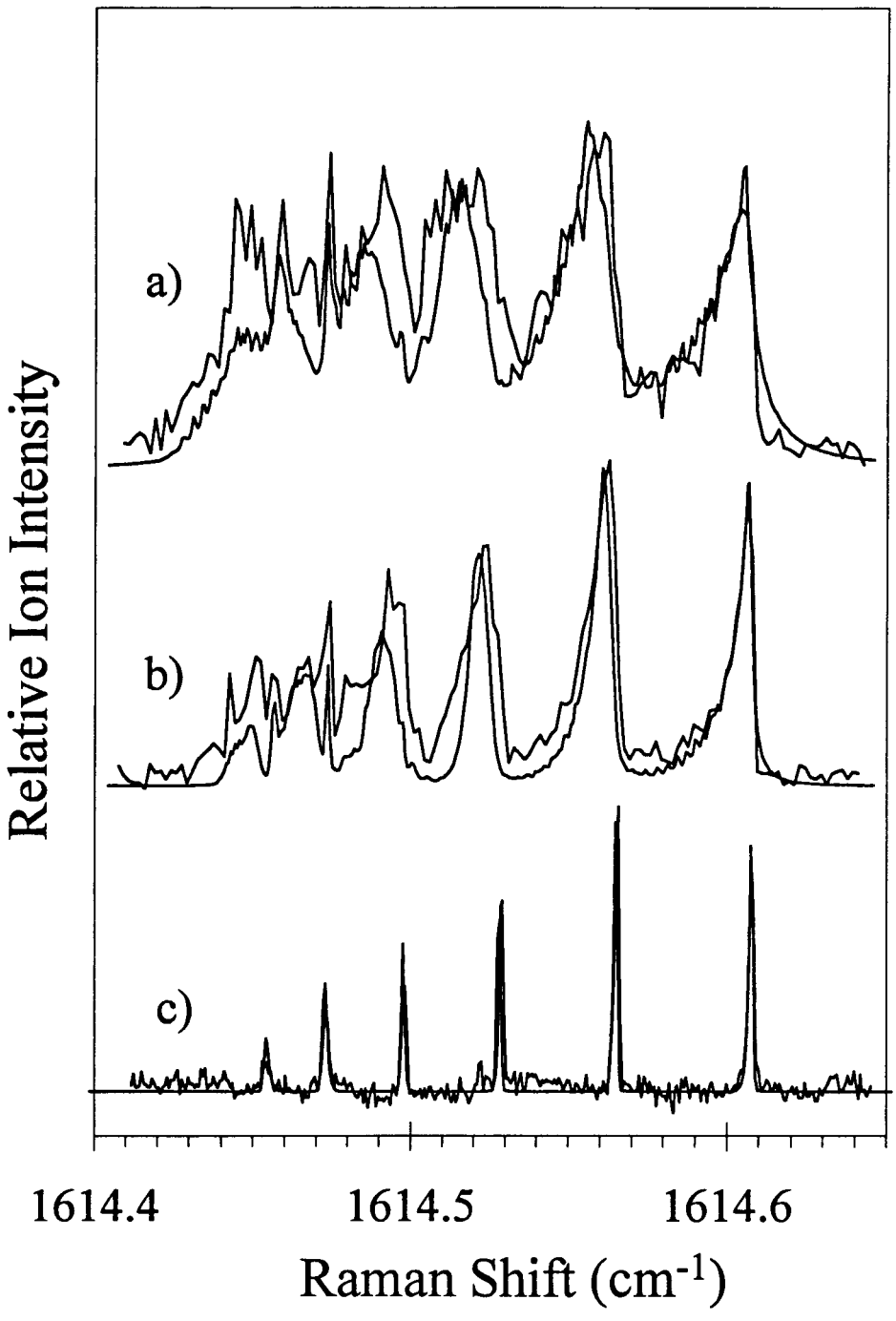

Figure 5-8 Power dependence of the ν_8, ^sS-branch spectrum of benzene with simulated data overlaid. The experimental energies used were: a) 30 mJ, b) 15 mJ, c) 1.5 mJ.

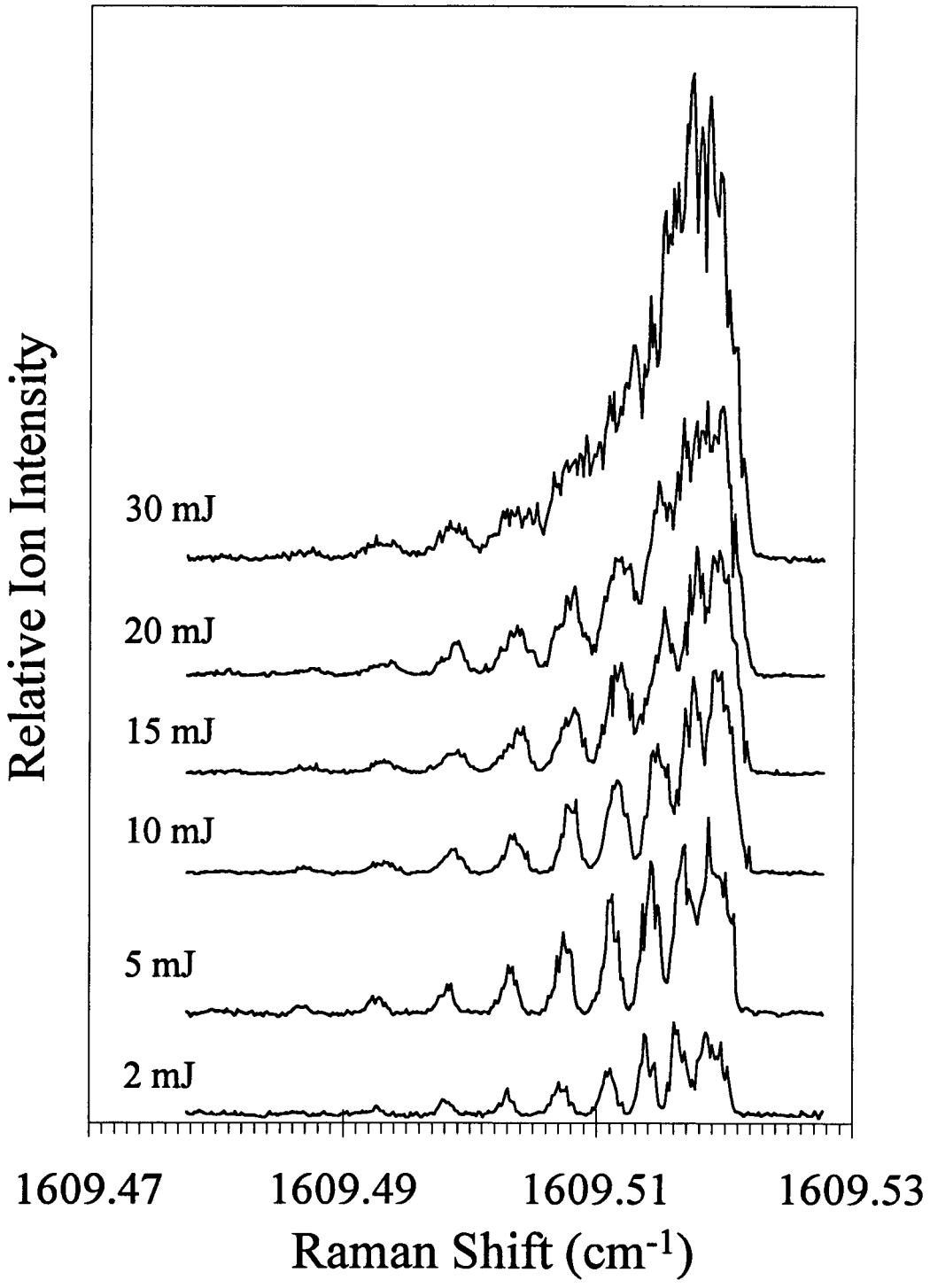

Figure 5-9 Power dependent IDSRS spectra of the ν_8 $K = 1$ ^{O}Q-branch of benzene. Notice how narrow the lines remain at high laser energies compared to the ^{S}S-branch spectra in **Figure 5-2**.

Figure 5-9 should be saturation at higher laser energies. It is remarkable that linewidths remain very narrow over the range of laser energies shown in the figure. The 2 mJ spectrum is about 3 times narrower than the 30 mJ spectrum, going from 0.001 cm^{-1} to 0.003 cm^{-1}, respectively. This should be contrasted with the ^{S}S-branch in Figure 5-2 where the linewidths go from about 0.0025 cm^{-1} for the 1.5 mJ spectrum to ~0.025 cm^{-1} (depending on the transition chosen) for the 30 mJ case. In principle the ^{O}Q-branch would be ideal for ascertaining the saturation effects in our experiment independent of AC Stark broadening. However, no quantitative analysis of these spectra was done for this particular band because it is very sensitive to the center frequency and spectral intensity profile of the UV laser, so modeling of the experimental data is difficult. Nevertheless, comparing the power dependent lineshapes in Figure 5-2 and Figure 5-9 demonstrates that Stark broadening can be useful as a spectroscopic tool since one can make rotational branch assignments based on the lineshapes observed. Actually, it is possible to make even more specific rotational line assignments based on the shapes of the lines within a particular branch. An example of this is shown in Figure 5-2 where the middle peak has a symmetric Stark broadening while the lines on either side fan out toward the middle peak.

The Stark effect in nitrogen should be much smaller than that for benzene since the isotropic polarizability, α, of N_2 is about 1.76 $Å^3$ compared to 10.3 $Å^3$ for benzene.[71] But, as can be seen from the optical stimulated Raman spectrum[72] in part b) of Figure 5-10, there is an appreciable Stark shift and broadening of the Q-branch lines even at modest laser energies of 14 mJ with a 15 ns pulse. In contrast to the optical spectrum is the IDSRS spectrum in part a) of Figure 5-10. This spectrum was taken at a laser energy of

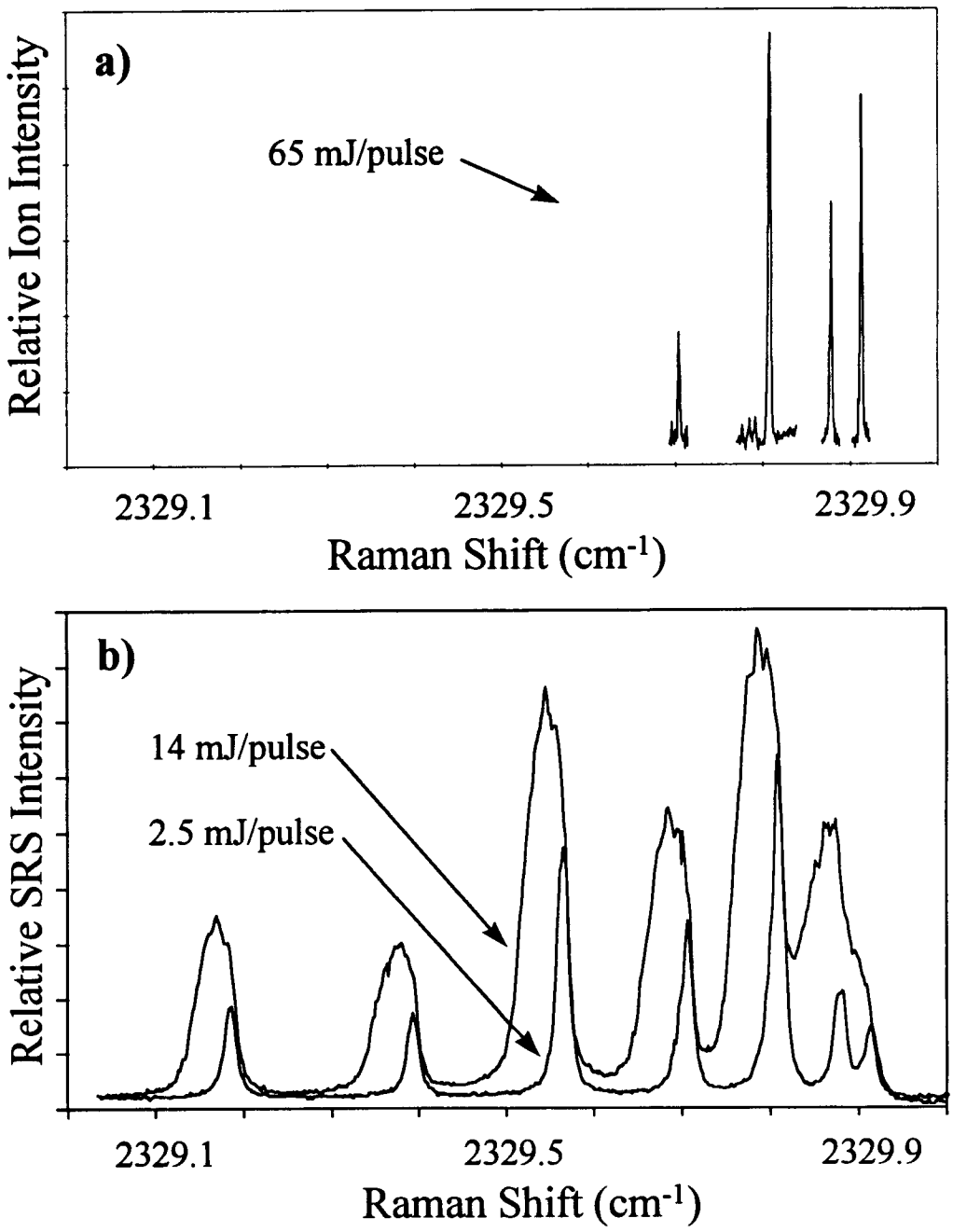

Figure 5-10 a) IDSRS Q-branch spectra of N_2 taken with our apparatus at 65 mJ/pulse. b) Optical SRS spectra taken at 14 and 2.5 mJ.[72] Note that Stark shifts and saturation broadening are readily seen in the optical spectra, while the IDSRS spectra, with much higher energies and comparable temporal pulse widths, have linewidths remarkably close to the instrumental width.

65 mJ (20 ns pulse) but, remarkably, shows only a small amount of broadening in the peaks. The difference in linewidths may be a consequence of using two separate lenses for this IDSRS experiment. Due to the 2 + 2 ionization of nitrogen, a short focal length lens must be used in the ionization step for the IDSRS measurement. The narrowing of the Stark broadened lines in the nitrogen IDSRS spectra may in part be attributed to the fact that the focus of the UV laser is approximately 5 times tighter than the focus of the Raman beams so we probe only molecules that feel a mostly uniform field. In fact, calculation shows that the intensity of the Raman beams only varies by approximately 6% in the region that the UV probes our sample. This illustrated in Figure 5-11 which shows the measured beam waist and intensity profile of both lasers at the focal point. The difficulty with this explanation of the IDSRS linewidths is that saturation and temporal broadening still remain and should broaden the lines even with the narrow spatial selection.

Another, perhaps more probable, explanation for the difference in linewidths is that the focal volumes are not exactly overlapped at the most intense part of the focus. This would mean that the UV laser samples a region in the Raman pumping beams that has a larger focus and therefore shows a smaller Stark effect and saturation. This is a potentially a very useful result. If true, then by simply increasing the focal volume one could increase the number of molecules sampled (increasing the signal) while simultaneously decreasing the saturation and Stark broadening. Further studies to test this possibility are recommended.

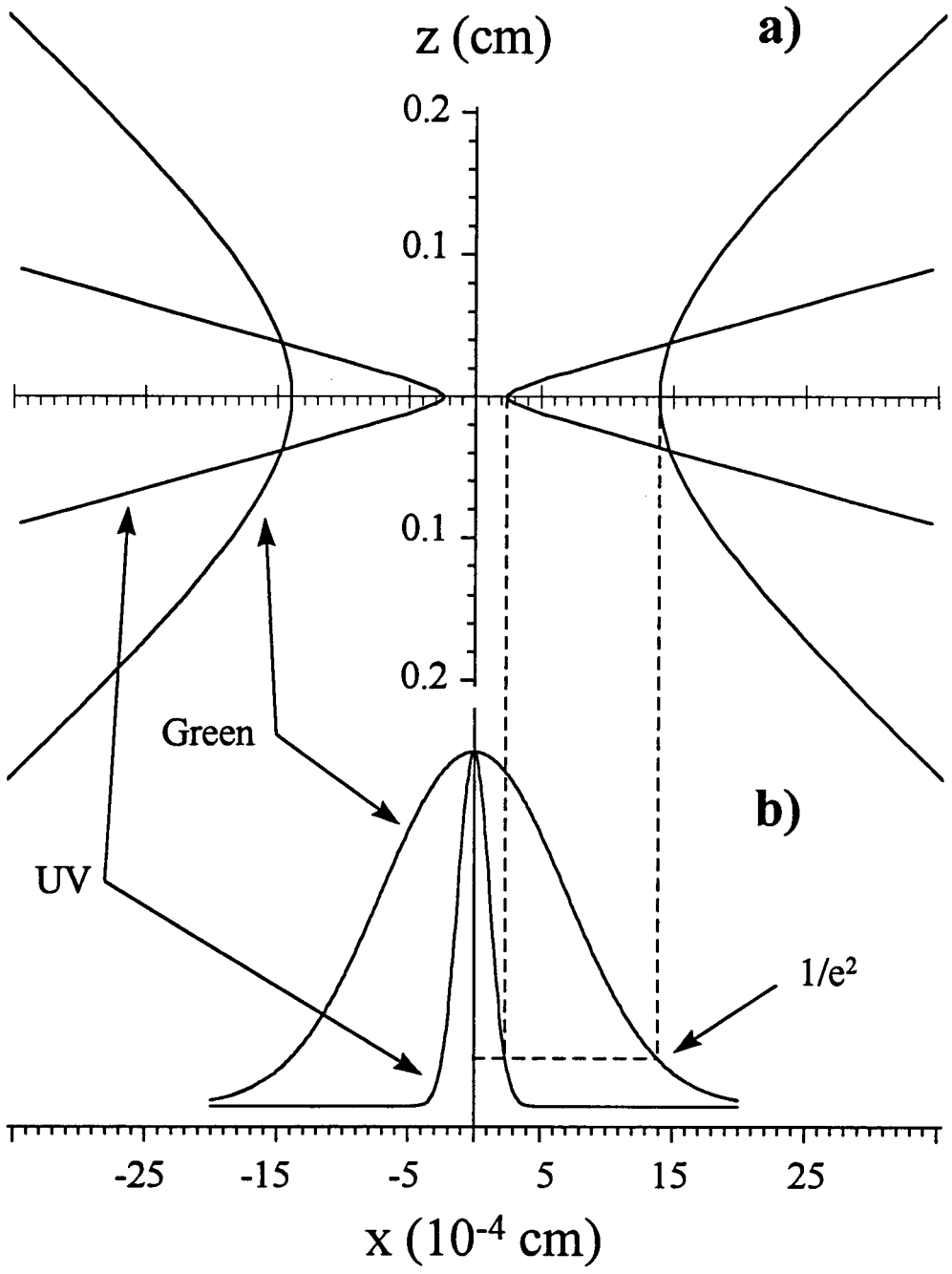

Figure 5-11 The upper part of the figure compares the experimentally measured beam waists (with measurements made in the far field) for the green (532 nm) and the UV laser (~270 nm). We can see that the UV focus is approximately 7 times tighter than the green. In part b) the transverse Gaussian intensity profile is shown for both beams and the dashed lines indicate the $1/e^2$ point.

5.5 Conclusion

We have shown that simple expressions for the Stark split energies and transition intensities can be found using first and second order perturbation theory. With the inclusion of temporal and spatial integration as well as saturation effects, we have also been able to qualitatively reproduce our experimental spectra. By choosing an experimental design that uses counter propagating laser beams for the Raman and UV, we have demonstrated that the peak linewidths can be effectively reduced. Further work to exploit this feature would seem worthwhile.

It may also be desirable to consider a more correct model for saturation in an effort to improve the spectral simulation. The model used here is in the cw limit, which assumes that the lasers have been on a long time and equilibrium has been established. Also, this model assumes that there is some kind of collisional relaxation process that depopulates the upper vibrational/rotational state, a condition that does not apply in the low density jet. Since our lasers are only on for a few nanoseconds we expect that the cw limit assumption is not adequate. Instead, the temporal pumping efficiency should be included in the coupled differential equations that describe the time development of the population in the upper and lower states. This calculation is formidable however, and it is satisfying that even with the flaws of the cw model, the qualitative fit of the simulation to the experimental data is quite good.

6. CONCLUSIONS

A new experimental apparatus was built to perform high resolution stimulated Raman spectroscopy in a pulsed molecular jet at state densities of the order of 10^{11} cm^{-3}. A stimulated Raman step first populates a vibrational/rotational level and then a resonantly enhanced multiphoton ionization (REMPI) step probes the Raman pumped upper state. By accelerating the resulting ions down a time of flight mass spectrometer (with mass resolution of 182 amu) and detecting the ions with a home built microchannel plate detector, mass selective Raman spectroscopy is made possible. The demonstrated instrumental linewidth of 0.001 cm^{-1} in the benzene experiment is remarkable for Raman spectroscopy and will provide an unusual capability for probing the structure and dynamics of many other molecular systems. The cold molecular beam is advantageous not only because the collisional and Doppler contributions to linewidths are reduced to less than the instrumental resolution, but also because the rotationally resolved spectra are simplified to a great extent due to the reduced temperature.

The IDSRS results on nitrogen are significant because nitrogen was ionized using a difficult 2 + 2 REMPI step for detection of the Raman pumped vibrational/rotational state. Even so, the detection limit was improved by a factor of 10^4 over optical stimulated Raman spectroscopy. These results demonstrate that IDSRS can effectively be used for small molecules that have large ionization potentials.

The high resolution of this experiment, coupled with the high electric fields needed for the nonlinear Raman pumping, has enabled a qualitative study of the AC Stark

splittings that come about through the *induced* dipole moment of the molecule. By including saturation and temporal/spatial broadening along with the Stark splittings, a good qualitative fit to the experimental spectra was obtained. Due to the unique power dependent lineshapes of the Stark split rotational transitions, the Stark effect can be a useful spectroscopic tool for Raman rotational assignments within a particular vibrational band.

With the use of counter propagating beams for the Raman and UV lasers, the experimental linewidths can be effectively reduced. The most probable reason for this is that the focal volumes are not exactly overlapped at the most intense part of the focus. This allows the UV laser to sample a region in the Raman pumping beams that has a larger focus and therefore has a smaller Stark effect and saturation. If this is the case, then by simply increasing the focal volume (e.g., by using a longer focal length lens) one could increase the number of molecules sampled (increasing the signal) while simultaneously decreasing the saturation and Stark broadening. Further experiments that explore this possibility are recommended.

BIBLIOGRAPHY

1. D. E. Cooper, C. M. Klimcak, and J. E. Wessel, Phys. Rev. Lett. **46**, 324 (1981)

2. D. E. Cooper and J. E. Wessel, J. Chem. Phys. 76, 2155-2160, (1982)

3. P. Esherick and A. Owyoung, Chem. Phys. Lett. **103**, 235, (1983)

4. P. Esherick and A. Owyoung, J. Plíva, J. Chem. Phys. **83**, 3311-3317, (1985)

5. J. Plíva and P. Esherick and A. Owyoung, J. Mol. Spectrosc. **125**, 393-412, (1987)

6. W. Bronner, P. Oesterlin, and M. Schellhorn, Appl. Phys. B **34**, 11-15 (1984)

7. G. V. Hartland, B. F. Henson, V. A. Venturo, R. A. Hertz, and P. M. Felker, J. Opt. Soc. Am. B 7, 1950-1959, (1990)

8. B. F. Henson, G. V. Hartland, V. A. Venturo, and P. M. Felker, J. Chem. Phys. **91**, 2751-2753, (1989)

9. V. A. Venturo, P. M. Maxton, and P. M. Felker, J. Phys. Chem. **96**, 5234-5237, (1992)

10. P. M. Felker, P. M. Maxton, M. W. Schaeffer, Chem. Rev. **94**, 1787-1805, (1994)

11. V. A. Venturo, and P. M. Felker, J. Chem. Phys. **99**, 748-751, (1993)

12. V. A. Venturo, and P. M. Felker, J. Phys. Chem. **97**, 4882-4886, (1993)

13. P. M. Maxton, M. W. Schaeffer, S. M. Ohline, W. Kim, V. A. Venturo, and P. M. Felker, J. Chem. Phys. **101**, 8391-8408, (1994)

14. P. M. Maxton, M. W. Schaeffer, and P. M. Felker, Chem. Phys. Lett. **241**, 603-610, (1995)

15. W. Kim, and P. M. Felker, J. Chem. Phys. **104**, 15, (1996)

16. S. Dhawan, IEEE Trans. Nuc. Sci., **28**, 672-676, (1981)

17. Mansour Zehedi, Ph.D. thesis, Oregon State University, 1993

18. Diode-Pumped Solid-State Non-Planar Ring Laser Users Manual
Lightwave Electronics
Mountain View, CA
415-962-0755

19. J. A. Harrison, M. Zahedi, and J. W. Nibler, Opt. Lett. **18**, 149, (1993)

20. Stanford Research Systems, Users Manual
1290 D Reamwood Avenue
Sunnyvale, CA 94089
408-744-9040

21. Dennis Barnaal, *Analog Electronics for Scientific Application*

22. Spectra Physics GCR-200 logbook, p. 003 yellow

23. *Optics and Filters*
ORIEL CORPORATION
250 Long Beach BLVD
P.O. box 872 Stratford, CT 06497
Tel: 203-377-8282

24. R. Guenther, *Modern Optics*

25. W. C. Wiley and I. H. Mclaren, Rev. Sci. Instrum. **26**, 1150, (1955)

26. J. D. Jackson, *Classical Electrodynamics*, Second Edition

27. R. A. Serway, *Physics for Scientists and Engineers*, Second Edition

28. S. Dhawan, IEEE Transactions on Nuclear Science, **28**, 672, (1981)

29. Intevac, Incorporated
EO Sensors Division
601 California Avenue
Palo Alto, CA 94304-0883
Tel: 415-493-1800
Fax: 415-4933658

30. Product Bulletin
Varian, LSE Division
611 Hansen Way
Palo Alto CA 94306
415-493-4000

31. Instruction Manual
Edwards High Vacuum International
Manor Royal, Crawley,
West Sussex, RH10 2LW, UK
Tel: (0293) 528844

32. Instruction Manual
Alcatel Vacuum Products
1050 East Duane Ave., Suite E
Sunnyvale, CA 94086
Tel: 408-746-2947

33. E. Riedle, Th. Knittel, Th. Weber, and J. J. Neusser, J. Chem. Phys. **91**, 4555-4563, (1989)

34. U. Boesl, H. J. Neusser, R. Weinkauf, and E. W. Schlag, J. Phys. Chem. **86**, 4857-4863, (1982)

35. D. Easter, X. Li, and R. Whetten, J. Chem. Phys. **95**, 6362, (1991)

36. D. Easter, M. El-Shall, M. Hahn, and R. Whetten, Chem. Phys. Lett. **157**, 277, (1989)

37. P. Johnson, J. Chem. Phys. **64**, 4143, (1976)

38. S. Long, J. Meek, and J. Reilly, J. Chem. Phys. **79**, 3206, (1983)

39. J. Hopkins, D. Powers, and R. Smalley, J. Phys. Chem. **85**, 3739, (1981)

40. U. Boesl, H. J. Neusser, and E. W. Schlag, J. Chem. Phys. **72**, 4327-4333 (1980)

41. H. Kühlewind, H. J. Neusser, and E. W. Schlag, J. Phys. Chem. **88**, 6104-6106 (1984)

42. H. Kühlewind, H. J. Neusser, and E. W. Schlag, Int. J. Mass Spectrom. Ion Phys. **51**, 255-265 (1983)

43. H. Kühlewind, A. Kiermeier, and H. J. Neusser, J. Chem. Phys. **85**, 4427-4435 (1986)

44. David R. Lide, CRC *Handbook of Chemistry and Physics*, 71st edition, (1990-1991)

45. A. B. Hollinger and H. L. Welsh, Can. J. Phys. **56**, 1513-1525, (1978)

46. J. M. Fernández-Sánchez and S. Montero, J. Chem. Phys. **90**, 2909-2914, (1989)

47. C. S. Parmenter, Adv. Chem. Phys., **22**, 365, (1972)

48. E. Arunan and H.S. Gutowsky, J. Chem. Phys. **98**, 4294, (1993)

49. B.F. Henson, G.V. Hartland, V. A. Venturo, and P.M. Felker, J. Chem. Phys. **97**, 2189-2208, (1992)

50. J. B. Hopkins, D. E. Powers, and R. E. Smalley, J. Phys. Chem. **85**, 3739-3742 (1981)

51. O. Krätzschmar, H. L. Selzle, and E. W. Schlag, J. Phys. Chem. **98**, 3501-3505 (1994)

52. J. A. Menapace, E. R. Bernstein, J. Phys. Chem. **91**, 2533-2544 (1987)

53. Th. Weber, A. von Bargen, E. Riedle, and H. J. Neusser, J. Chem. Phys. **92**, 90-96 (1990)

54. R. Sussmann, R. Neuhauser, and H. J. Neusser, J. Chem. Phys. **103**, 3315-3324 (1995)

55. B. F. Henson, V. A. Venturo, G. V. Hartland, and P. M. Felker, J. Chem. Phys. **98**, 8361 (1993)

56. D. R. Miller, in *Atomic and Molecular Beam Methods*, edited by G. Scoles (Oxford University Press, Oxford, 1988), Vol. I, Chap. 2.

57. R. D. Beck, M. F. Hineman, and J. W. Nibler, J. Chem. Phys. **92**, 7068 (1990)

58. R. G. Bray and R. M. Hocstrasser, Mol. Phys. **31**, 1199 (1976)

59. J. Stark, Berl. Ber., **47**, 932 (1913)

60. J. Stark , Ann. d. Phys., **43**, 965 (1914)

61. T. W. Dakin, W. E. Good, and D. K. Coles, Phys. Rev. **70**, 560, 1946

62. L. H. Scharpen, J. S. Muenter, and V. W. Laurie, J. Chem. Phys., **53**, 2513 1970

63. B. Girard, G. Sitz, and R. Zare, J. Chem. Phys. **97**, 26-41, (1992)

64. R. L. Farrow and L. A. Rahn, Phys. Rev. Lett. **48**, 395-398, (1982)

65. B. Friedrich and D. Herschbach, Phys. Rev. Lett., **74**, 4623 (1994)

66. W. Kim and P. Felker, J. Chem. Phys., **104**, 1147 (1996)

67. D. Papousek and M. R. Aliev, *Molecular Vibrational-Rotational Spectra*, Elsevier Scientific Publishing Company, (1982)

68. R. N. Zare, *Angular Momentum*, (1987)

69. M. Leuchs, M. Crew, J. Harrison, M. Hineman, and J. Nibler, J. Chem. Phys. **105**, 4485-4888, (1996)

70. K. Shimoda, *Introduction to Laser Physics*, Springer Series in Optical Sciences **44**

71. Hirschfelder, Curtiss, and Bird, *Molecular Theory of Gasses and Liquids*, p. 950, (1954)

72. Rainer Beck, Ph.D. thesis, Oregon State University (1990)

APPENDICES

Appendix A . UNCERTAINTY RELATION FOR GAUSSIAN PULSES

Assume the electric field is modulated in time by a Gaussian line shape so that the magnitude of the field as a function of time is given by the relation

$$E(t) = E_0 e^{-at^2} e^{i\omega_o t}. \tag{A.1}$$

It is the intensity, not the electric field, that is the quantity we measure in the lab. Thus, we relate the intensity to the electric field through the equation

$$I(t) = \frac{1}{8\pi} \left|E(t)\right|^2. \tag{A.2}$$

Using (A.1) in this expression gives for the intensity

$$I(t) = \frac{E_0^{\,2}}{8\pi} e^{-2at^2}. \tag{A.3}$$

Typically, the standard measurement of the pulse width is the full width at half the maximum (FWHM), which for our case is;

$$\Delta t_{FWHM} = \sqrt{\frac{2 \ln 2}{a}} \tag{A.4}$$

To find the FWHM of the intensity in frequency space we must first Fourier transform the electric field,

$$E(\omega) = \frac{1}{\sqrt{2\pi}} \int_{-\infty}^{\infty} E_o e^{i\omega_o t - at^2} e^{-i\omega t} dt \tag{A.5}$$

and then square that to get the intensity as a function of frequency,

$$I(\omega) \propto |E(\omega)|^2. \tag{A.6}$$

Note that it is not the Fourier transform of the intensity but rather the electric field that is important for uncertainty relation. This is because the electric field carries all the information about the laser pulse and when the fields are squared all phase information is lost. Simplifying the integral in (A.5) gives,

$$E(\omega) = \frac{E_o}{\sqrt{2\pi}} e^{-\frac{(\omega_o-\omega)^2}{4a}} \int_{-\infty}^{\infty} e^{-a\left[t+\frac{i(\omega-\omega_o)}{2a}\right]^2} dt \tag{A.7}$$

which evaluates to

$$E(\omega) = \frac{E_o}{\sqrt{2a}} e^{-\frac{(\omega_o-\omega)^2}{4a}}. \tag{A.8}$$

Using this in (A.2) gives for the intensity as a function of frequency,

$$I(\omega) \propto e^{-\frac{(\omega_o-\omega)^2}{2a}}. \tag{A.9}$$

Solving (A.9) for the FWHM in terms of linear frequency gives,

$$\Delta\upsilon = \frac{\sqrt{2 \ln 2}}{\pi} \tag{A.10}$$

so that the uncertainty relation for a Gaussian laser pulse is

$$\Delta\upsilon \Delta t = \frac{2 \ln 2}{\pi} \approx 0.44 \tag{A.11}$$

Appendix B . SECOND ORDER ENERGY CORRECTIONS TO THE STARK ENERGIES

Starting with (5.12),

$$E^{(2)}_{JKM} = -\frac{1}{6}\gamma E_Z^2 \sum_{\substack{J'=J-2,\\ J'\neq J}}^{J+2} \frac{\left|\left\langle J'KM\left|D^{2\,*}_{00}\right|JKM\right\rangle\right|^2}{E^{(0)}_{JKM} - E^{(0)}_{J'KM}} \tag{B.1}$$

we expand out just the summation, including the explicit form for the zero order energies of a symmetric top in the denominator

$$\begin{aligned}\sum = &\frac{\left|\left\langle J-2KM\left|D^{2\,*}_{00}\right|JKM\right\rangle\right|^2}{2B(2J-1)} + \frac{\left|\left\langle J-1KM\left|D^{2\,*}_{00}\right|JKM\right\rangle\right|^2}{2BJ} \\ &- \frac{\left|\left\langle J+1KM\left|D^{2\,*}_{00}\right|JKM\right\rangle\right|^2}{2B(2J+1)} - \frac{\left|\left\langle J+2KM\left|D^{2\,*}_{00}\right|JKM\right\rangle\right|^2}{2B(2J+3)}.\end{aligned} \tag{B.2}$$

To evaluate the matrix elements in the numerator we make use of (5.11) for each term

$$\begin{aligned}\sum = &\frac{(2J-3)(2J+1)\begin{pmatrix} J-2 & 2 & J \\ -M & 0 & M\end{pmatrix}^2\begin{pmatrix} J-2 & 2 & J \\ -K & 0 & K\end{pmatrix}^2}{2B(2J-1)} \\ &+ \frac{(2J-1)(2J+1)\begin{pmatrix} J-1 & 2 & J \\ -M & 0 & M\end{pmatrix}^2\begin{pmatrix} J-1 & 2 & J \\ -K & 0 & K\end{pmatrix}^2}{2BJ} \\ &- \frac{(2J+3)(2J+1)\begin{pmatrix} J+1 & 2 & J \\ -M & 0 & M\end{pmatrix}^2\begin{pmatrix} J+1 & 2 & J \\ -K & 0 & K\end{pmatrix}^2}{2B(2J+1)} \\ &- \frac{(2J+4)(2J+1)\begin{pmatrix} J+2 & 2 & J \\ -M & 0 & M\end{pmatrix}^2\begin{pmatrix} J+2 & 2 & J \\ -K & 0 & K\end{pmatrix}^2}{2B(2J+3)}.\end{aligned} \tag{B.3}$$

With the use of Mathematica, we evaluate each of the 3j symbols and then obtain the final result for the second order energy correction as

$$E_{JKM}^{(2)} = -\frac{1}{6}\gamma E_z^2\left\{\frac{(2J-3)(2J+1)}{2B(2J-1)}\left[\frac{3(J-M-1)(J-M)(J+M-1)(J+M)}{2J(J-1)(2J-1)(2J-3)(2J+1)}\right]\right.$$
$$*\left[\frac{3(J-K-1)(J-K)(J+K-1)(J+K)}{2J(J-1)(2J-1)(2J-3)(2J+1)}\right]$$
$$+\frac{(2J-1)(2J+1)}{2BJ}\left[\frac{6(J-M)M^2(J+M)}{2J(J-1)(J+1)(2J-1)(2J+1)}\right]$$
$$*\left[\frac{6(J-K)K^2(J+K)}{2J(J-1)(J+1)(2J-1)(2J+1)}\right]$$
$$-\frac{(2J+3)(2J+1)}{2B(2J+1)}\left[\frac{3(J-M+1)M^2(J+M+1)}{J(J+1)(J+2)(2J+1)(2J+3)}\right]$$
$$*\left[\frac{3(J-K+1)K^2(J+K+1)}{J(J+1)(J+2)(2J+1)(2J+3)}\right]$$
$$-\frac{(2J+4)(2J+1)}{2B(2J+3)}\left[\frac{3(J-M+1)(J-M+2)(J+M+1)(J+M+2)}{2(J+1)(J+2)(2J+1)(2J+3)(2J+5)}\right]$$
$$\left.*\left[\frac{3(J-K+1)(J-K+2)(J+K+1)(J+K+2)}{2(J+1)(J+2)(2J+1)(2J+3)(2J+5)}\right]\right\}$$